

SN 1994W: a Type IIn Supernova without Core Collapse?

Luc Dessart^{1,2*}, D. John Hillier³, Suvi Gezari⁴, Stéphane Basa⁵, and Tom Matheson⁶

¹ Department of Astronomy and Steward Observatory, The University of Arizona, Tucson, AZ 85721

² Department of Astrophysical Sciences, Princeton University, Princeton, NJ 08544

³ Department of Physics and Astronomy, University of Pittsburgh

⁴ California Institute of Technology, Pasadena, CA 91125

⁵ Laboratoire d’Astrophysique de Marseille, France

⁶ NOAO Gemini Science Center, 950 North Cherry Avenue, Tucson, AZ 85719

Accepted . Received

ABSTRACT

We present a multi-epoch quantitative spectroscopic analysis of the Type IIn SN 1994W, an event interpreted by Chugai et al. as stemming from the interaction between the ejecta of a SN and a $0.4 M_{\odot}$ circumstellar shell ejected 1.5 yr before core collapse. During the brightening phase, our models suggest that the source of optical radiation is not unique, perhaps associated with an inner optically-thick Cold Dense Shell (CDS) and outer optically-thin shocked material. During the fading phase, our models support a *single* source of radiation, an hydrogen-rich optically-thick layer with a near-constant temperature of ~ 7000 K that recedes from a radius of 4.3×10^{15} cm at peak to 2.3×10^{15} cm 40 days later. We reproduce the hybrid narrow-core broad-wing line profile shapes of SN 1994W at all times, invoking an optically-thick photosphere exclusively (i.e., without any external optically-thick shell). In SN 1994W, slow expansion makes scattering with thermal electrons a key escape mechanism for photons trapped in optically-thick line cores, and allows the resulting broad incoherent electron-scattering wings to be seen around narrow line cores. In SNe with larger expansion velocities, the thermal broadening due to incoherent scattering is masked by the broad profile and the dominant frequency redshift occasioned by bulk motions. We speculate that, given the absence of broad lines at all times and the very low ^{56}Ni yields, SN 1994W may be the result of an interaction between two ejected shells with no core collapse.

Key words: radiative transfer – stars: atmospheres – stars: supernovae: individual: 1994W

1 INTRODUCTION

Understanding the diversity of supernova (SN) spectra and light curves is a considerable challenge. Although some SN classes suffer less and less ambiguity, as in the thermonuclear incineration of a Chandrasekhar-mass white dwarf leading to a Type Ia SN, or as in the collapse of the degenerate core of a massive star leading to Type II or Type Ib/c SNe, a unified picture of stellar explosions is compromised by the growing number of atypical SNe that emerge from deeper and more frequent searches for transient phenomena in the local and distant Universe. One such type of peculiar SNe are “n”-suffixed (i.e. IIn, IbN, IAn), in reference to their atypical narrow line profiles. This suggests that despite the bright, supernova-like, visual display, the expansion rate of the radiating layer is small, i.e. of a few 100 km s^{-1} , in contrast with the large ejecta velocities, of a few 1000 km s^{-1} , associated with SN explosions. Paradoxically, these events can boast a huge bolometric luminosity — a few $10^9 L_{\odot}$ sustained for weeks (as in SN 1994W) but associ-

ated with a spectral energy distribution (SED) typical of a 10,000 K blackbody, hence implying “photospheric” radii of a few 10^{15} cm ($L \sim 2 \times 10^9 (R_{15})^2 (T_4)^4 L_{\odot}$, where R_{15} is the radius in units of 10^{15} cm and T_4 the temperature in units of 10^4 K).

All SN ejecta yield photospheric radii of 10^{15} cm a few weeks after explosion, but the remarkable property of Type IIn SNe is that they achieve this with an apparent slow expansion. The common interpretation is that Type IIn SNe interact with material present in the direct environment of the exploding star, forming the “photosphere” where that external material resides, at a few 10^{15} cm. If its mass is on the order of the ejecta mass, this outer material can cause a significant deceleration of the ejecta, with an efficient conversion of kinetic energy into internal and radiative energy.

The narrow line cores are accompanied, in a subset of IIn SNe, by broad (and symmetric) line wings which are generally interpreted as arising from multiple electron-scattering of line photons in the circumstellar (CS) shell with which the ejecta collide (Chugai 2001). These optical “peculiarities” are also often associated with the detection of X-ray and/or radio emission, as well as significant spectral variations. Although interaction is evident in many SNe

* E-mail: luc@as.arizona.edu

(see, e.g., Chevalier & Fransson 1994, 2001; Fransson et al. 1996), Type IIn SNe are objects in which the interaction is central, and perhaps “makes” the SN (i.e., the interaction can increase the luminosity so that it is easier to detect).

Given the rich mass loss history and the many alternate channels of evolution, massive stars are the prime candidates for such interactions, in particular the hydrogen-rich, Type II, SNe. A few well-documented examples that reveal the wealth and the diversity of phenomena hosted by such IIn events are SN 1988Z (Stathakis & Sadler 1991; van Dyk et al. 1993; Turatto et al. 1993; Chugai & Danziger 1994; Fabian & Terlevich 1996; Aretzaga et al. 1999; Williams et al. 2002; Schlegel & Petre 2006), SN 1994W (Sollerman et al. 1998, hereafter SCL; Tsvetkov 1995; Schlegel 1999; Chugai et al. 2004a, hereafter C04), SN 1995G (Pastorello et al. 2002; Chugai & Danziger 2003), SN 1995N (Fox et al. 2000; Fransson et al. 2002; Mucciarelli et al. 2006; Chandra et al. 2005; Zampieri et al. 2005), SN 1997eg (Salamanca et al. 2002; Hoffman et al. 2007), SN 1998S (Bowen et al. 2000; Gerardy et al. 2000; Leonard et al. 2000; Liu et al. 2000; Anupama et al. 2001; Chugai 2001; Lentz et al. 2001; Fassia et al. 2000, 2001; Chugai et al. 2002; Pooley et al. 2002; Fransson et al. 2005; Pozzo et al. 2004, 2005). Despite the common IIn SN type, the above sample of SNe do not boast a uniform set of properties, some being bright for weeks, some for months or even years; some showing a clear brightness plateau after peak, others fading by a few magnitudes in just a few weeks, etc. Objects classified as “n-”type SNe are in fact shaking the common understanding of what makes a SN.

The Type IIn SN 2006gy, the most luminous SN ever seen, may have originated from a pair-instability explosion (Smith et al. 2007; Ofek et al. 2007; Smith & McCray 2007), or consecutive pair-instability pulsations (Woosley et al. 2007) in a supermassive star. Also recently, SN 2006jc joined SN 1999cq and SN 2002ao to consolidate the rare SN Ibn type, characterized by narrow lines of helium instead of hydrogen, an interpretation that conflicts with the notion that pre-SN mass ejections are generally associated with hydrogen-rich stars (e.g., Luminous Blue Variables, LBVs, see Davidson & Humphreys 1997; Matheson et al. 2000; Foley et al. 2007; Pastorello et al. 2007). Interaction with CS material has also been invoked in the Type Ia SN 2002ic following the observations of narrow hydrogen-line emission in the optical spectrum (Hamuy et al. 2003; Chugai & Yungelson 2004; Chugai et al. 2004b; Deng et al. 2004; Kotak et al. 2004; Wang et al. 2004; Wood-Vasey et al. 2004; Benetti et al. 2006; Han & Podsiadlowski 2006; Wood-Vasey & Sokoloski 2006; Chugai & Chevalier 2007).

Modeling such an interaction is a complicated radiation hydrodynamics problem, in which the uncertainties in the properties of both shells prior to interaction add to those of the interaction itself. The diversity of observations, suggests that a similar diversity is to be found in the circumstances of the interaction. Focusing from now on on the massive star progeny, the outer, CS, material may arise from the pre-SN steady-state wind mass loss, an LBV outburst, perhaps a violent pair-instability pulsation, or some yet unidentified ejection mechanism occurring recurrently (and without core collapse) or immediately prior to core-collapse. The inner shell that rams into this CS shell may arise from a core collapse SN explosion (which may be neutrino-, acoustic-, or magnetically-driven; see Woosley & Janka 2005 for a review), a pair-instability pulsation, a pair-instability explosion, or some other form of explosion. For a SN-like display to occur, the inner shell must be fast to catch up with the CS material and cause a violent shock. A short delay between the two mass ejections will raise the probability for detection. A large kinetic energy is involved, and the conversion

of kinetic to thermal energy supplies the internal/radiant energy inferred from the bolometric light curve. Moreover, mass/energy distribution of both shells may not be spherical (Leonard et al. 2000; Hoffman et al. 2007) and thus, viewing effects may complicate further the dynamics of the interaction and the interpretation of the emitted light. Finally, the bolometric display may be altered by an additional contribution from radioactive decay of unstable isotopes, which are normally associated with SN ejecta.

An attempt to quantitatively interpret the Type IIn SN 1994W was undertaken by C04 who performed radiation-hydrodynamics and radiative-transfer calculations to model very high quality multi-epoch spectroscopic and photometric observations (see also SCL). For SN 1994W, C04 associate the narrow line core with an expanding CS envelope. The broad line wings arise from a combination of shocked cool gas in the forward post-shock region, and multiple electron scattering in the CS envelope. They associate the absence of broad P Cygni line profiles with obscuration by an optically-thick cold dense shell (CDS) that forms at the interface of SN ejecta and a CS envelope. They inferred a CS envelope with a particle density $n \sim 10^9 \text{ cm}^{-3}$, a radial extent of a few 10^{15} cm , an electron-scattering optical depth of $\gtrsim 2.5$, explosively ejected $\sim 1.5 \text{ yr}$ prior to the SN explosion. The light curve showed a rise time to peak of about 30 days (after the reference date of the 14th of July 1994), followed by a slow decline by about two magnitudes until 110 days, and a sudden decline beyond that date (see Fig. 1 in SCL).

Despite all the complexities that surround this ejecta/CS-envelope interaction, the inferred presence by C04 of an optically-thick CDS suggests that the approach we follow for the modeling of photospheric-phase Type II-Plateau (II-P) SNe (Dessart & Hillier 2005ab, 2006, 2008; Dessart et al. 2008) may also apply here. In this work, we provide insights into the spectroscopic and light-curve evolutions of SN 1994W between day 20 and 100, thus covering from ~ 10 days before peak, through to the slow decline that follows until 10 days before the steep brightness drop.

The main results from this work are that although the outward-moving CDS is likely opaque until the peak of the light curve, the photosphere recedes both in mass and radius for post-peak times as the material cools and recombines. In this context, the sharp drop at 110 days is the transition to the nebular phase, when the ejecta/CSM is entirely optically-thin, in analogy with the end of the plateau phase in Type II-P SNe. We also find that the broad wings on the Balmer lines can be explained by multiple electron scattering in the photosphere — we do not need multiple density structures to explain the observed spectrum.

In the next section, we discuss the reddening and distance used in our study of SN 1994W. In Section 3, we evaluate various timescales that characterize Type IIn SNe. We then summarize our modeling approach in Section 4, presenting the various approximations we make to mimic as best we can the complicated configuration of the interacting SN 1994W. In Section 5, we present the ejecta properties we infer from the modeling of the photometric and spectroscopic observations at multiple epochs during its optically-bright phase. We reproduce the narrow line core and the broad line wings by invoking a single region of emission/absorption (the photosphere), rather than the CDS and CS-envelope configuration. In Section 6, we discuss the line formation process in our models of SN 1994W, and emphasize the important role of electron-scattering in some Type IIn SN photospheres that are characterized by low, and perhaps nearly constant, expansion velocities. We finally present our conclusions and discuss the implication of our results for interacting SNe in a more general context in Section 7.

2 REDDENING & DISTANCE

Following SCL we adopt a distance to SN 1994W of 25.4 Mpc which is based on $H_0 = 65 \text{ km s}^{-1} \text{ Mpc}^{-1}$ and the Virgo infall model of Kraan-Korteweg (1986). This is somewhat larger than the distance estimate of 18.0 Mpc by Gao & Solomon (2004) which used $H_0 = 75 \text{ km s}^{-1} \text{ Mpc}^{-1}$ and was corrected for motion of the local group. While the choice of distance will effect the adopted luminosity and inferred photospheric radii other conclusions in this paper (including T_{phot}) are not affected. The reddening is more problematical since it can affect the relative flux distribution. SCL find $E(B - V) = 0.17 \pm 0.06$ mag based on the equivalent width of the NaID doublet and its correlation with $E(B - V)$ while C04 estimate 0.15 mag from blackbody fits to spectra at several different dates. As the galactic extinction in the direction of SN 1994W is low, most of the reddening must be internal to the host galaxy (SCL). Our present model, particularly of spectra past the peak, supports the SCL reddening although values of 0.15 to 0.20 mag are also compatible with the observations. In this work, we employ a reddening of 0.15–0.17, but also explore the effects of reducing the reddening to 0.07 on Day 21.

3 TIMESCALES

A typical expansion velocity for SN 1994W, as measured from the narrow line profiles, is 800 km s^{-1} . We can use this to define an expansion timescale using a typical photospheric radius of $4 \times 10^{15} \text{ cm}$. This gives an expansion time-scale of 1.6 years. As noted earlier, this, together with the large luminosity, and the difficulty of creating SNe with a low expansion velocity, are reasons for the argument that the 800 km s^{-1} is not an intrinsic SN expansion velocity. C04 suggest it is the velocity of CS material that was ejected prior to the SN explosion. Alternatively, it could reflect the velocity of a shell of gas that has arisen from the interaction of circumstellar gas with the SN ejecta. The largest red-supergiants have radii of 10^{14} cm (see, e.g., Levesque et al. 2005), significantly smaller than the inferred photospheric radius.

The light travel time across the SN is $2R/c \sim 3.1$ days. This is marginally significant, and indicates that the observed light curve will be averaged over this timescale. The diffusion time is of order $\tau R/cn$, where n is the exponent of the power law density. This will also have a significant impact on the observed light curve, although it is less clear whether it will affect our spectroscopic modeling in which we fix the luminosity at the base of the photosphere.

4 MODEL PRESENTATION

In hydrogen-rich environments, having an optically-thick layer simplifies considerably the radiative transfer problem. The associated large bound-free opacities ensure that the radiation is thermalized before escaping through the photosphere — all photons at depth will be absorbed and re-emitted according to a blackbody distribution characterized by the local electron temperature, irrespective of the details of the interaction. Hence, we have a setup that is analogous to that of a typical stellar atmosphere. Not accounted for in this configuration is the potential contribution from the optically-thin layers above the photosphere that have been shocked. These regions can contribute to the electromagnetic display directly, as they often do in the X-ray and radio ranges, or alter the photospheric conditions through external irradiation. How well we reproduce the observations may be a gauge on how much these regions contribute

to the total SN luminosity and affect the photospheric conditions. In the case of SN 1994W we can reproduce the observations after the peak by photospheric radiation alone. However before the peak we cannot fully reproduce the observations accurately, possibly indicating that optically thin gas makes an important contribution. Alternatively, neglected effects such as departures from spherical symmetry and time dependent effects, may be important at such early times (Dessart & Hillier 2008).

We model the observations with the non-LTE steady-state one-dimensional radiative transfer code CMFGEN (Hillier & Miller 1998; Dessart & Hillier 2005a) which solves self-consistently the radiative transfer equation and the statistical equilibrium equations under the constraint of radiative equilibrium. Of particular relevance for this work, CMFGEN treats accurately the electron-scattering source function. With our adopted distance and a reddening of $E(B - V) = 0.17$ mag a blackbody emitter, with a temperature of 10^4 K and a radius of 10^{15} cm , would have an observed V-band magnitude of ~ 14.5 , in close agreement with the observed value around Day 50 (see Fig. 1 of SCL98). We therefore started our model analysis with a typical Type II-P SN model just prior to hydrogen recombination (as in Dessart & Hillier 2005a, 2006 or Dessart et al. 2008), and modified the radius and luminosity to agree with the above brightness estimate. We also adopt a supergiant-like composition, i.e. $X_{\text{H}} = 0.55$, $X_{\text{He}} = 0.44$, $X_{\text{C}} = 5.3 \times 10^{-4}$, $X_{\text{N}} = 2 \times 10^{-3}$, $X_{\text{O}} = 2.8 \times 10^{-3}$. Metal abundances are taken at the solar value. We use the same model atom for all investigations presented here, with HI , HeI , CI , CII , NI , NII , NaI , MgII , SII , CaII , AlIII , AlIII , OI , OII , SII , SIII , CrII , CrIII , MnII , MnIII , TII , TIII , CoII , CoIII , NiII , NiIII , FeII , FeIII , FeIV (details on the levels treated are omitted, but our choice is such that increasing the number of levels does not alter the computed ejecta properties nor the emergent synthetic spectrum). References to the atomic data used in this work are given in Dessart & Hillier (2005a).

Dynamical simulations by Chevalier (1982) and C04 suggest that in the present context a very steep density fall-off would prevail above the CDS, while the velocity would be decreasing from the CDS outward into the shocked CS envelope. Adopting a power-law density distribution of the form $\rho(R) = \rho_0(R_0/R)^n$, where ρ_0 and R_0 are, respectively, the density and the radius at the optically-thick model base, we enforce a steep density fall off by taking a density exponent n equal to 10. Flatter density distributions, as in a wind solution with $n = 2$, yield optical line fluxes that are systematically stronger than observed. Steeper density distributions lead to weaker line fluxes and/or absorption lines. With our current approach and from extensive experimentation, we indeed find that the density distribution at the photosphere has to be steep, in fact comparable to that used for the modeling of Type II-P SNe.¹

The transfer equation solver in CMFGEN requires *monotonically* expanding ejecta. In SN ejecta, the steep density profile tends to make the line and continuum formation quite confined in space, so the material properties on a large scale tend to matter little compared to the properties in the immediate vicinity of the photosphere. In our approach, we assume homologous expansion for simplicity, and adjust the ejecta velocity to match the observed line profile widths. (note that in the line transfer problem, it is the magnitude of the velocity gradient at the photosphere, rather than its sign, that matters; see Sobolev 1960, Castor, Abbott, & Klein 1975). Obviously, this is a numerical convenience and we do not

¹ Note that recombination to a neutral state may attenuate the spectral dependence on the density distribution above the photosphere.

Table 1. Model Characteristics for SN 1994W. For each date in our sample of observations, we provide the following CMFGEN model parameters: Base comoving-frame luminosity L_{CMF, R_0} and emergent observer-frame luminosity $L_{\text{OBS}, R_{\text{Max}}}$ (in $10^8 L_{\odot}$), photospheric conditions describing the electron temperature T_{phot} (in K), the radius R_{phot} (in 10^{15} cm), the velocity V_{phot} (in km s^{-1}), the mass density (in $10^{-14} \text{ g cm}^{-3}$), and the free-electron density $N_{e,\text{phot}}$ (in 10^9 cm^{-3}). In all models, a density exponent $n = 10$ characterizes the density law $\rho(R) = \rho_{\text{phot}}(R_{\text{phot}}/R)^n$. M_V and m_V correspond to V -band absolute, and reddened plus distance-diluted (using a distance of 25.4 Mpc and a reddening of 0.17 with $R_V = 3.1$), synthetic magnitudes. Because there are clear inconsistencies between our model and the observations on Days 21 and 31, we quote the corresponding model parameters on those dates only for completeness - we do not suggest they accurately describe SN 1994W on these two dates. ^a: Days after 14.0 July 1994. ^b: So-called hot model, used to fit observations on the 4th and the 14th of August, both poorly. ^c: So-called cool model, used to fit observations on the 4th and on the 14th of August (but poorly for both dates), and on the 1st of September (satisfactorily).

Day YY-MM-DD	Phase ^a Days	L_{CMF, R_0} ($10^8 L_{\odot}$)	$L_{\text{OBS}, R_{\text{Max}}}$	T_{phot} (K)	R_{phot} (10^{15} cm)	V_{phot} (km s^{-1})	ρ_{phot} ($10^{-14} \text{ g cm}^{-3}$)	$N_{e,\text{phot}}$ (10^9 cm^{-3})	M_V synthetic	m_V
1994-08-04 ^b	21.5	66.0	61.7	10350	2.86	830	0.82	3.3	-18.78	13.37
1994-08-14 ^b	31.5	66.0	61.7	10350	2.86	830	0.82	3.3	-18.78	13.37
1994-09-01 ^c	49.5	47.0	42.0	7480	4.32	830	0.62	2.1	-18.80	13.75
1994-09-09	56.9	27.0	24.0	7450	3.33	840	0.84	2.7	-18.37	14.18
1994-10-01	79.5	9.8	8.7	6310	2.37	790	2.7	5.2	-17.61	14.94
1994-10-11	89.5	9.0	8.0	6020	2.32	712	7.6	7.5	-17.59	14.96

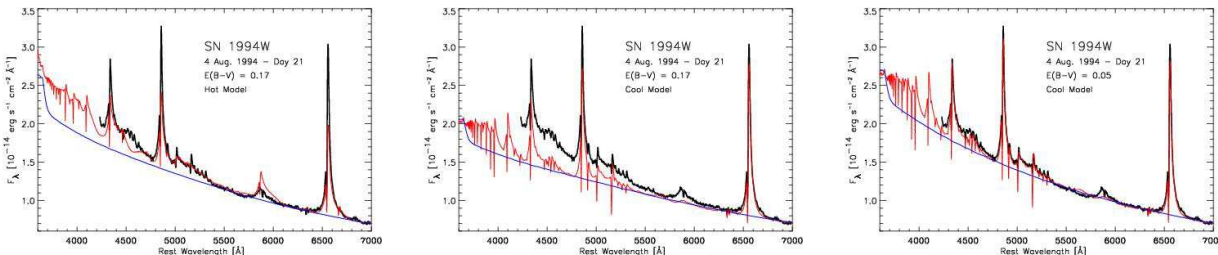


Figure 1. *Left:* Comparison between the reddened ($E(B-V) = 0.17$ mag) full (red) and continuum-only (blue) synthetic spectrum and the observations of SN 1994W on the 4th of August 1994 (Day 21; black). The synthetic flux is scaled by a factor of 1.06 to adjust to the absolute level of the observed flux. The ejecta ionization predicted with our model parameters reproduces the slope of the SED adequately, but it over-estimates the strength of $\text{HeI } 5875\text{\AA}$ and underestimates the strength of FeII lines. Note however the good fit to the Balmer lines. *Middle:* Same as left, but now with a cooler model used to fit observations on 1 September 1994 (see Fig. 3; we use a flux scaling of 0.93). Note the bad fit to the SED slope, but the improved fit to observed line profiles. *Right:* Same as middle, but using a reddening of 0.05 instead of 0.17. Now, the fit to both the continuum and lines is good. What causes this combination of blue continuum and lines of low-ionization species is unclear. Being short-lived, it may be related to shocked material above the photosphere, rather than to large changes in photospheric conditions. Reducing the reddening is only a proxy for getting a good fit, for exploratory purposes at this date.

suggest that in reality the velocity increases linearly with radius outwards, although it might. Later on, to test the dependence on the velocity gradient at the photosphere, we try out different values for the exponent β entering our parameterized velocity law, i.e. $V(R) = V_0(R/R_0)^\beta$, with β varying from 1 (homologous expansion) to 0.2, and 0.01 (near-constant velocity ejecta; here, V_0 is the model-base velocity). Moreover, to ensure the radiation is thermalized at the inner boundary, we extend our grid inwards to a radius where the Rosseland optical depth is ~ 100 . Finally, when comparing to observations, we first redden our synthetic spectra with the Cardelli law (Cardelli et al. 1989), and then adjust the synthetic flux (at most by a few percent) to get the desired overlap. This is a convenience, equivalent to a change in photospheric radius or distance (scaling with the square root of that scaling factor), that saves us from re-running a model that would otherwise have the same properties and spectrum (see discussion in Dessart & Hillier 2005a).

5 RESULTS

We have performed a spectroscopic analyzes of the data presented in SCL and C04 for the observations taken on the 4th and 14th (Section 5.1) of August, the 1st and the 9th of September, and the

1st and 11th of October 1994 (the last four dates are presented in Section 5.2), which correspond to days 21, 31, 49, 57, 79, and 89 after the 14th of July 1994 (we adopt that reference date for compatibility with SCL, who associate it with the “optical outburst” of SN 1994W).

These observations correspond to a phase of optical brightening prior to Day 30, followed by an 80-day long phase of slow optical fading ($\Delta m \sim 1.5$ mag), eventually followed by a sudden fading of the SN past day 110. We omit from our sample the lower quality data obtained on Day 18, as well as the late time, nebular spectrum obtained on Day 121. Model parameters for each epoch are stored in Table 1.

All observed spectra have been de-redshifted assuming a heliocentric velocity of 1249 km s^{-1} (C04). Using the Cardelli et al. (1989) law, we redden our synthetic spectra to match observations, using $E(B-V) = 0.17$ mag, unless otherwise stated. We also provide, as online material, the list of all lines between 3200\AA and 10500\AA that contribute an equivalent width (approximate since computed using the Sobolev approximation, and quoted merely to indicate the main contributors; Sobolev 1960) of at least 1\AA (in absolute value). Each line, in absorption, emission, or both, may appear as a single feature, or may overlap with neighboring lines to yield a complicated feature.

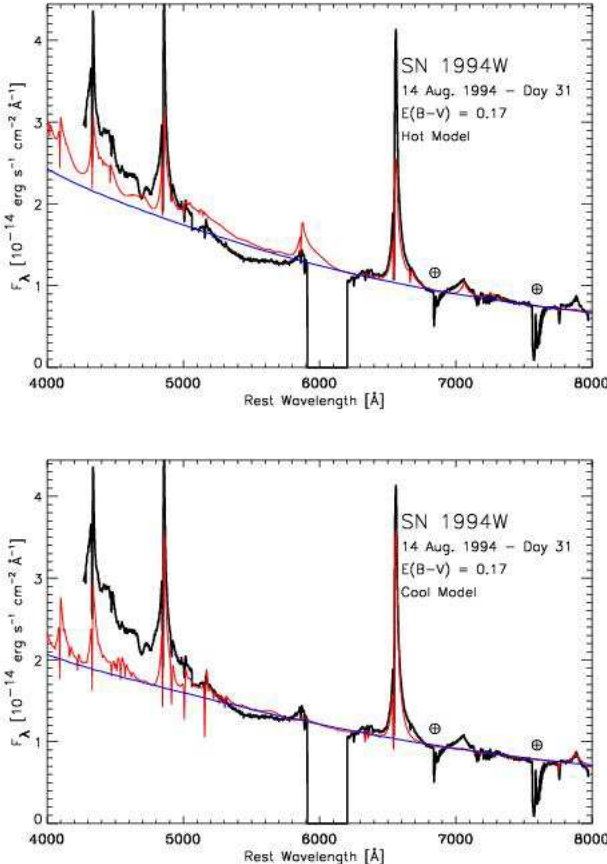


Figure 2. Top: Comparison between the reddened ($E(B-V)=0.17$ mag) full (red) and continuum-only (blue) synthetic spectra for a hot model and the observations of SN 1994W on the 14th of August 1994 (Day 31; black). The synthetic flux is scaled by a factor of 1.37 to adjust to the absolute level of the observed flux. Bottom: Same as left, but now with the (cooler) model employed for the observations of the 1st of September (we apply a flux scaling of 1.2). Notice how the $MgII$ 7877–7896Å (HeI 7065Å) line is well fitted with the cool (hot) model, but not both at the same time, suggesting two different sites/mechanisms for the origin of these lines. By contrast, the electron scattering wings are well reproduced in both models, despite the ejecta ionization changes.

5.1 Observations pre-peak optical brightness: Days 21 and 31

The spectral evolution of Type II-P SNe is governed by ejecta cooling and the increased effects of metal line blanketing. The SED is blue during the first 10 days after shock breakout and reddens dramatically as hydrogen recombines in the ejecta. Balmer lines are the strongest lines at all times, initially accompanied by HeI lines (5875Å is the most conspicuous, but other optical HeI lines are present) and then by FeII lines. These proceed in a monotonic sequence, so that HeI and FeII lines are not seen simultaneously.

In Type IIn SNe, and by contrast with Type II-P SNe, such smooth and monotonic evolution does not systematically hold. The spectrum of SN 1994W on Day 21 shows the simultaneous presence of both FeII and HeI optical lines (with absorption and emission components), in combination with a blue continuum. To illustrate this peculiarity, we show in Fig. 1 three different fits to the observations of SN 1994W on Day 21. In the left panel, we use a “hot model” with the following properties:

$R_{\text{phot}} = 2.86 \times 10^{15}$ cm, $V_{\text{phot}} = 830$ km s $^{-1}$, $T_{\text{phot}} = 10350$ K, $\rho_{\text{phot}} = 8.2 \times 10^{-15}$ g cm $^{-3}$, $N_{\text{e,phot}} = 3.3 \times 10^9$ cm $^{-3}$, and $L_{\text{OBS,RMax}} = 6.17 \times 10^9 L_{\odot}$. (We have scaled the synthetic flux by a factor of 1.06.) The model ejecta are relatively hot, nearly fully ionized (only helium is partially ionized just above the photosphere). The observed shape of the SED is approximately matched, but there are severe discrepancies. HeI 5875Å is too strong, both in the emission strength and width (note that using a solar composition for hydrogen and helium reduces, but does not resolve, this discrepancy). Numerous lines around 4500Å (TiII and FeII), as well as around 5200Å (mostly FeII), are strongly underestimated. Balmer lines are underestimated in strength, but well fitted in width. The absorption at ~ 800 km s $^{-1}$ from line center is also well reproduced.

In the middle panel of Fig. 1, we show the fits to the same observations, but using a cooler model ($T_{\text{phot}} = 7480$ K; we have scaled the synthetic flux by a factor of 0.93), the one that fits the observations of SN 1994W on the 1st of September 1994 (see Table 1 for characteristics). The slope of the synthetic SED is now in greater disagreement, but the ionization seems more adequate, as we predict all the observed lines, merely shifted vertically due to a redder/weaker continuum. As an experimentation, we reduced the reddening from 0.17 to 0.05, and, as evident in the right panel of Fig. 1, the fits to both the continuum and the lines become excellent. We do not support this reddening, as it is incompatible with past works (SCL, C04) and with the modeling done for later dates, even within the uncertainties. But, this experimentation suggests that two distinct regions contribute, one to form a blue nearly-featureless SED (as we do not see high-ionization lines), and another to produce the lines from low-ionization species (FeII). This is a distinctive feature of SN 1994W, not seen in Type II-P SNe, and only visible on this day and on day 31.

On day 31, the optical spectroscopic observations of SN 1994W undergo a drastic and atypical change, with the SED becoming bluer (C04 stress that this change is genuine, and not the result of a poor relative flux calibration), the narrow lines of FeII appearing as weaker and narrow features at, e.g., 5018Å and 5169Å. We identify H_I Balmer lines, HeI 5875Å, HeI 6678Å, and HeI 7065Å, and MgII 7877–7896Å. In the cool model (same as that used to model observations on the 1 September 1994) shown in the bottom panel of Fig. 2, the MgII lines and HeI 5875Å are well reproduced, but HeI 7065Å is not. By contrast, in the hot model (same as the hot model used on Day 21 presented above) shown in the top panel, the reverse is true.

Overall, our fits to these pre-peak brightness observations are very poor. The apparent increase in ionization between Days 21 and 31 is a unique feature of SN 1994W, never quite seen in standard SN ejecta (of any type), which are governed by the cooling associated with expansion, typically mitigated by the release of stored internal energy. The non-monotonic SED evolution of SN 1994W between days 21 and 31, and the simultaneous presence of lines suggestive of both high and low ejecta temperatures point towards two distinct radiating regions (or material), of distinct properties.

5.2 Observations post-peak optical brightness: Days 49, 57, 79, and 89

From day 49 onwards, the visual brightness of SN 1994W decreases slowly, from ~ 13.5 on that day down to ~ 15 on day 110 (SCL). Over that time, the observed spectral evolution is smooth and slow, analogous to that of Type II-P SNe during the plateau phase, and our fits are satisfactory. We present synthetic fits to ob-

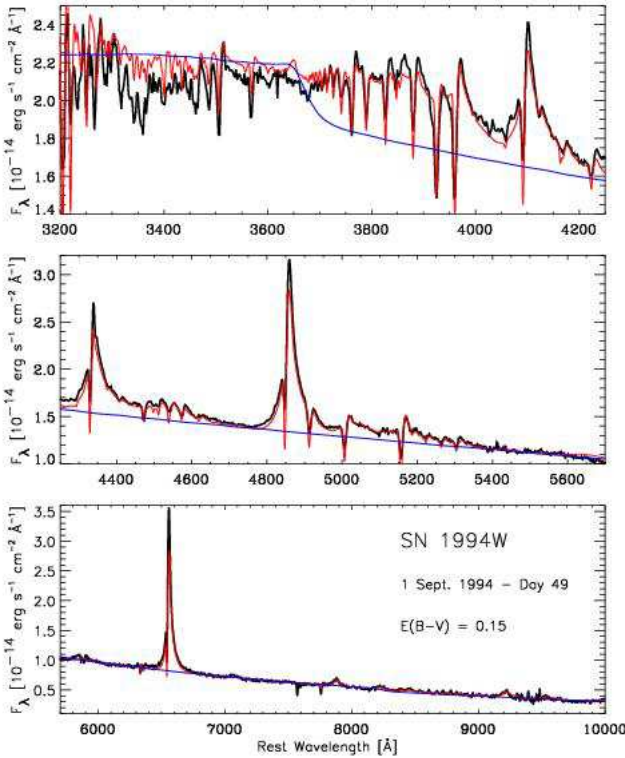


Figure 3. Comparison between the reddened ($E(B-V)=0.15$ mag) full (red) and continuum-only (blue) synthetic spectra and the observations of SN 1994W on the 1st of September 1994 (Day 49; black). The synthetic flux is scaled by a factor of 0.87 to adjust to the absolute level of the observed flux.

servations in Fig. 3 for Day 49, in Fig. 4 for Day 57, in Fig. 5 for Day 79, and in Fig. 6 for Day 89. We also give the corresponding model parameters in Table 1. These spectra are dominated by lines of low-ionization species, such as H α , FeII, NaI, CaII, MgII, with HeI 5875Å disappearing after Day 59 (see tables provided as online material for a complete census of all contributing lines). Observations and our synthetic SED now agree well, suggesting both lines and continuum form in the same region of space, i.e., under similar conditions of density and temperature. As on days 21 and 31, Balmer lines continue to show conspicuous narrow line cores with extended wings. Our fits to the line cores tend to be underestimated (by up to a factor of two on Day 89), but we can reproduce well the strength and width of the profile wings. These profile wings stem from multiple electron-scattering events of photons originally trapped in the line core, a phenomenon, in our approach, which occurs in the photospheric region (see § 6). We also predict the absorption dip at ~ 700 km s $^{-1}$, coincident for all lines within ± 100 km s $^{-1}$. This latter feature is also associated here with absorption internal to the photospheric region. We go back to these two intriguing characteristics in §6. The underestimate of the narrow line H α flux could be due to the neglect of time dependent effects (Dessart & Hillier 2008), or might be due to a change in the density distribution within the SN envelope (as characterized by the exponent n).

In the top panel of Figs. 7–9, we reproduce the fit shown in Fig. 5 but this time zooming on the 3100–4800Å region (Fig. 7), the 4800 to 6800Å region (Fig. 8), and the 6800 to 9800Å region

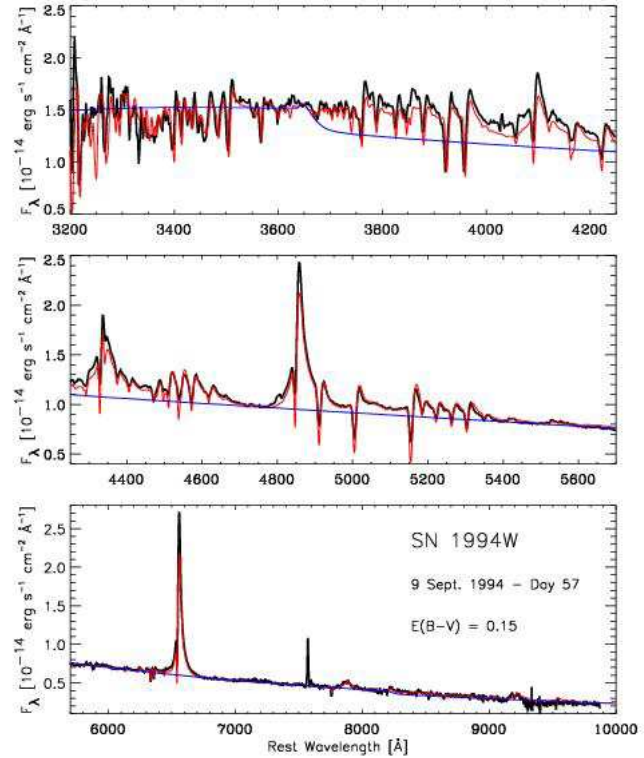


Figure 4. Comparison between the reddened ($E(B-V)=0.15$ mag; this is to reduce a slight discrepancy around 4000–5000Å) full (red) and continuum-only (blue) synthetic spectra and the observations of SN 1994W on the 9th of September 1994 (Day 57; black). The synthetic flux is scaled by a factor of 1.02 to adjust to the absolute level of the observed flux.

(Fig. 9). Moreover, in the bottom panels, we present the contributions of individual species by plotting the rectified synthetic spectra obtained by accounting for bound-bound transitions of individual species, labeled at right. At such a late time, besides Balmer and a few isolated MgII, NaI, SiIII, and CaII lines, we note the presence of a forest of FeII and TiIII lines blueward of ~ 4500 Å. The strengthening contribution of line emission and absorption is also evident in Figs. 3–6, where the blue curve describing the continuum SED departs more and more with time from the red curve including all absorption and emission processes, the more so at shorter wavelength. This makes the continuum level difficult to assess, and the comparison with a blackbody increasingly inadequate. This complication should be kept in mind when using blackbody arguments.

Over this period from Day 49 to 89, which covers the visual fading of the SN by ~ 1.3 mag, we find a modest reduction in the photospheric temperature, of ~ 1400 K ($\lesssim 20\%$), but a large reduction in the photospheric radius, by $\sim 2 \times 10^{15}$ cm (a factor of 2 reduction compared to the value on day 49). In the observer's frame and over these 40 days, this corresponds to a motion of the photosphere inward at an average velocity of ~ 6000 km s $^{-1}$. This is analogous to the reduction in the photospheric radius at the end of the plateau phase of Type II-P SNe, in which an ejecta extending out to a few times 10^{15} cm becomes entirely optically-thin in just ~ 2 weeks. Heuristically, the photometric fading and the strongly correlated B and V magnitudes support a reduction in the photo-

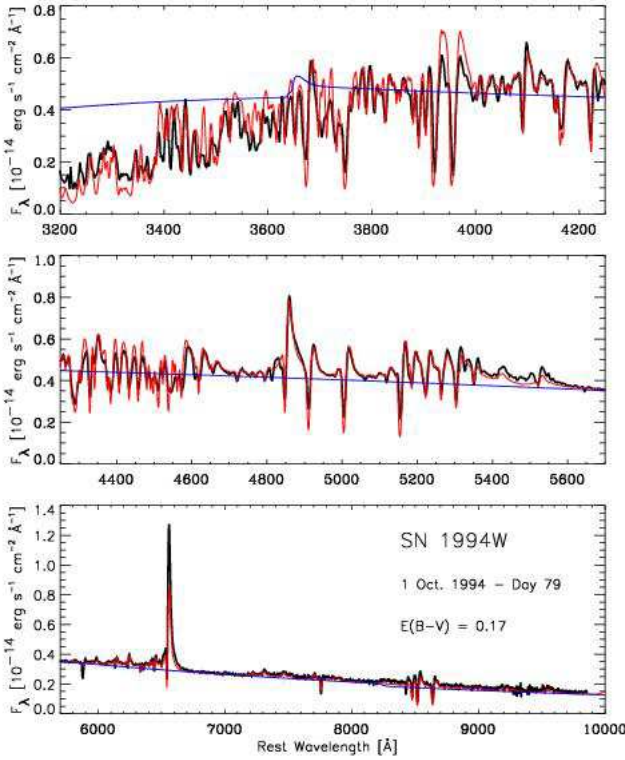


Figure 5. Comparison between the reddened ($E(B-V)=0.17$ mag) full (red) and continuum-only (blue) synthetic spectra and the observations of SN 1994W on the 1st of October 1994 (Day 79; black).

spheric radius and a fairly constant photospheric temperature, respectively.

The dynamics of the CDS is that of linear expansion with time (C04). Our findings suggest that the photosphere does not track the CDS, otherwise this linear expansion in time at near constant photospheric temperature would correspond to a phase of brightening. We instead observe a fading of the SN over that period. C04 associate the broad wings with the CDS deducing an expansion velocity of 4000 km s^{-1} . Over 100 days, the CDS would expand $\sim 3.5 \times 10^{15} \text{ cm}$, compared to our inferred reduction in R_{phot} of $\sim 2 \times 10^{15} \text{ cm}$.

Our models suggest that as time progresses, the photosphere recedes to deeper and deeper layers in a cold shell — probably the SN ejecta (or more generally the inner shell) but possibly also associated with the CDS initially. We surmise that, as time goes on, the emitting material radiates and expands sufficiently to cause ejecta cooling and recombination. The photosphere is completely slaved to the layer of ionized material above which free electrons are too scarce to provide any sizable optical depth. Lines, which form above the photosphere, tend also to track this region of high density and high ionization, in particular those that form primarily through recombination, e.g. Balmer lines. Since the ejecta are hydrogen-rich, this occurs at a temperature of $\sim 7000 \text{ K}$, and that temperature is essentially fixed. With further cooling, it is not the temperature at the photosphere but instead the radius of the photosphere that adjusts, shrinking to deeper layers.

This process has already been identified as the primary cause for the plateau phase of Type II-P SNe: the photospheric tempera-

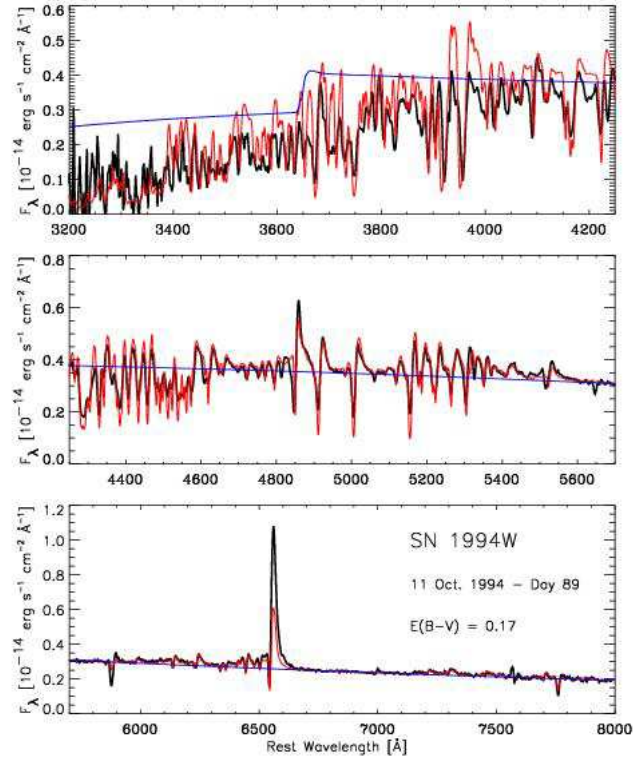


Figure 6. Comparison between the reddened ($E(B-V)=0.17$ mag) full (red) and continuum-only (blue) synthetic spectra and the observations of SN 1994W on the 11th of October 1994 (Day 89; black). The synthetic flux is scaled by a factor of 0.87 to adjust to the absolute level of the observed flux.

ture remains fixed at $\sim 7000 \text{ K}$, with a recession in mass coordinate of the photosphere, compensated in this case by the fast expansion of the ejecta so that the photospheric radius remains roughly constant during that phase (see Fig. 16 in Dessart et al. 2008). The end of the plateau phase and the fast drop into the nebular phase will correspond to the time when the inward-traveling photosphere no longer sustains a high enough density and ionization to remain optically thick. In other words, the end of the plateau phase would not correspond to the time when the CDS reaches the outer edge of the outer shell (C04), but to the time when the photosphere eventually reaches the cold, fully-recombined, inner layers of the SN ejecta/inner-shell.

Since the CDS seems to be optically thin after the epoch of peak-brightness, it cannot obscure the SN ejecta buried at depth. The absence of broad SN-like spectral features may then result from the ejecta deceleration by the reverse shock. Some deceleration is expected if conversion of kinetic energy into internal energy is to power the SN brightness, but the exact circumstances that cause the absence of ejecta material with velocity at the photosphere greater than $\sim 800 \text{ km s}^{-1}$ at all times are unclear. Even at day 121, in the nebular phase, the expansion velocities indicated by $\text{H}\alpha$ are consistent with an expansion of $\sim 800 \text{ km s}^{-1}$ (C04). This is consistent with the idea that we are observing a shell of material moving with near constant velocity, but which is now in the nebular phase.

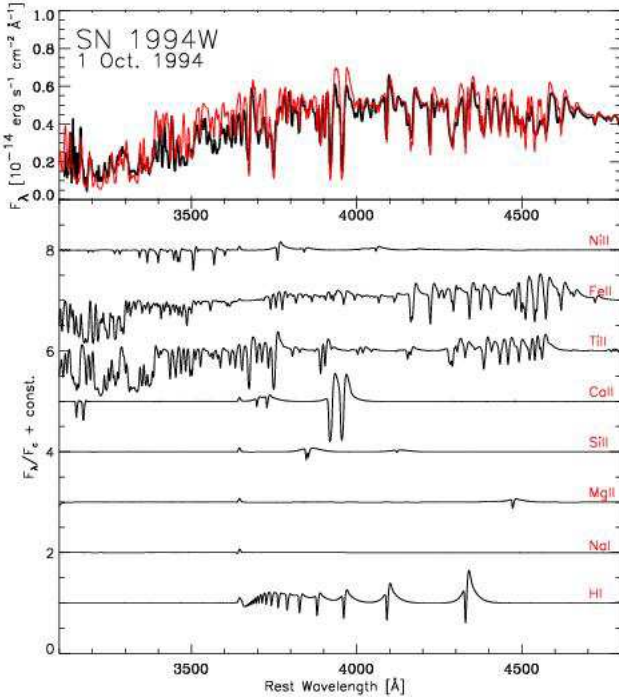


Figure 7. Top: Comparison between the reddened ($E(B-V)=0.17$ mag) synthetic spectrum (red) and the observations of SN 1994W on the 1st of October 1994 (Day 79; black), between 3100 and 4800Å. Bottom: Rectified synthetic spectra for the model shown at top, but including bound-bound transitions only of the individual species labeled on the right.

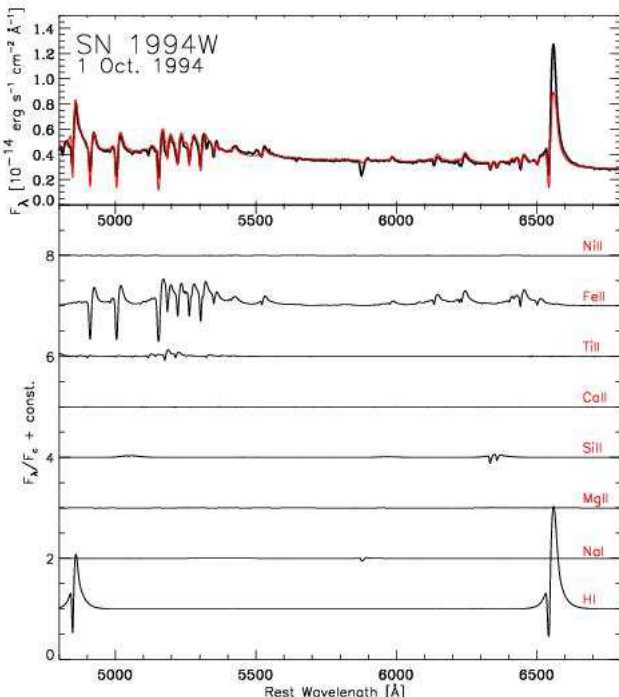


Figure 8. Same as Fig. 7, but for the range 4800 to 6800Å.

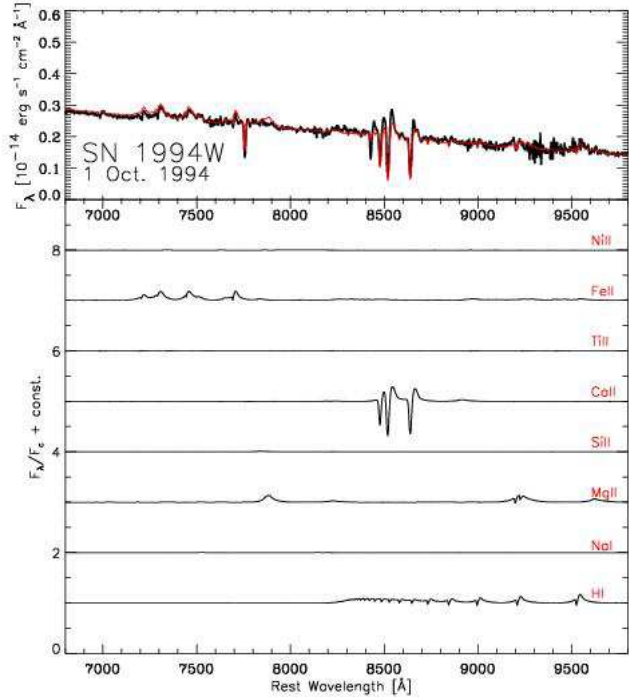


Figure 9. Same as Fig. 7, but for the range 6800 to 9800Å.

6 DISCUSSION OF LINE PROFILE FORMATION AND THE ELECTRON SCATTERING WINGS

6.1 Observational aspects

The distinctive feature of Type IIn SNe is the presence of narrow, and usually symmetric, line cores at all times. In some cases, as for SN 1994W, these are accompanied by broad, and relatively symmetric line wings, giving the overall line profile a triangular shape (see Fig. 10). These are in stark contrast with the broad and P-Cygni profiles, observed in Type Ia/b/c and Type II-P SNe, associated with optically-thick line formation in an expanding medium. As shown in the preceding sections, our modeling approach allows us to reproduce this hybrid morphology of a narrow line core and extended line wings, as illustrated more clearly in our fit to the $H\alpha$ line profile on the 1st September 1994 (Fig. 11).

In Type IIn's, the narrow line core has been interpreted as line emission from a slowly expanding region. C04 argue that the lack of SN features in the optical spectrum of SN 1994W is in support of the presence of an *optically-thick* CDS, whose velocity is on the order of ~ 4000 km s^{-1} . The narrow line core flux then stems from the region between the CDS and the outer slowly moving circumstellar shell. The broad wings, according to C04, may stem from various mechanisms/regions. Turbulent, clumpy, and fast moving material above the CDS and underneath the outer shell may contribute. Radiation-driving may also cause some acceleration of the material just above the CDS, which could then be at the origin of some line broadening.

C04 also argue for multiple scattering of line photons by electrons in an optically-thick CS envelope. Such non-coherent electron scatterings redistribute line photons in frequency space, and if multiple, can cause a spreading of the line core flux (see below). Because multiple-scattering of line photons occurs when the electron-

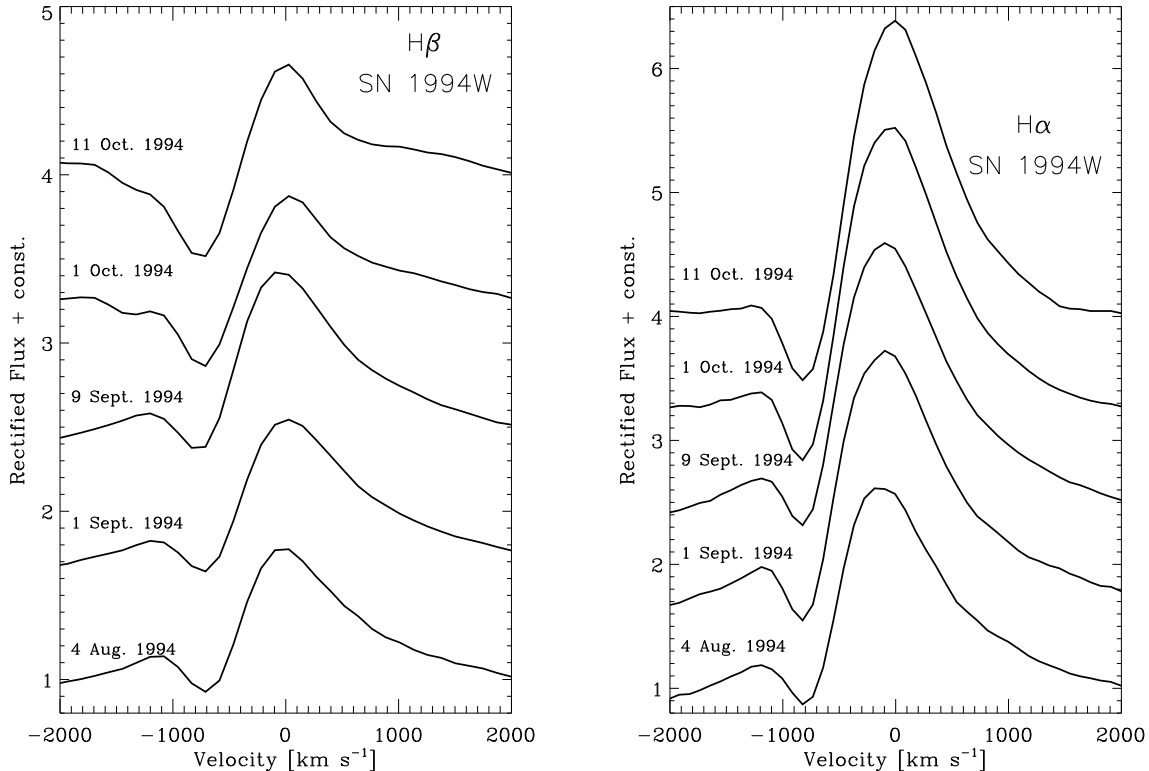


Figure 10. Montage of the evolution (a label gives the date) of the observed H β (left) and H α (right) line profiles versus Doppler velocity (we correct for a redshift of 1249 km s $^{-1}$) for SN 1994W (the spectra are normalized to unity at +2000 km s $^{-1}$ and shifted vertically for visibility). Note the extended wings of the narrow-peak Balmer line profiles, with a blue-wing emission contribution that decays with time, by contrast with the strengthening of the red contribution. Note also the velocity blueshift of the emission peak at early times (see Dessart & Hillier 2005a for a physical interpretation), as well as the near-constancy of the velocity location of maximum absorption.

scattering optical depth is large the presence of such wings has been associated with the presence of an external optically-thick CS envelope. The decrease of the strength of these wings as time progresses (Fig. 10) would then follow from the decrease in the shell thickness above the outward-migrating CDS.²

Insights into the source of electron scattering can be provided by studying different H lines. For example, a test for the presence of a shell external to the line formation region is that the strength of the electron scattering wings should be directly proportional to the line flux. Indeed, given the electron scattering optical-depth of the external shell, the number of line photons that end up in the electron-scattering wings of each line should scale with the number of line photons injected at the base of this optically-thick layer. In the *top-left* panel of Fig. 12, we show the observed (rectified and scaled) Balmer line profiles on 1 September 1994. Having normalized each peak line flux to unity, it is apparent that the flux in the profile wings increases as we progress up the Balmer series, although for H δ the rectification may be somewhat in error (there is a background of overlapping lines contributing in the H δ region). This argues against an external shell as the sole source of electron

scattering. However, the observed behavior can be explained if the regions of line formation and electron scattering overlap.

In the *top-right* panel, we show the corresponding synthetic Balmer line profiles produced with the models described in the previous section. These exhibit the same correlation as the observed profiles — the wings extend \sim 3000 km s $^{-1}$ away from line center, even for the weaker lines in the series, and are “strongest” for the higher series members. Hence, we do not identify a clear (linear) flux correlation between line core and line wing. By contrast, we find that the synthetic line wing strength scales with the electron-scattering optical depth in the formation region of the corresponding line. In Fig. 13, we plot for Balmer lines (black; the thickness of the line differentiates the transition) the variation of the quantity $\zeta(R)$ (which corresponds to the emission interior to R in the line through the integral $\int_{R_0}^R \zeta(R') d \log R'$) with respect to the electron-scattering optical depth integrated inwards from the outer grid radius. The relatively weak (strong) line wings of H α (H β) correlate with the relatively low (high) electron-scattering optical depth in the formation region of the line. In this plot, the situation is most severe for H γ , which forms deepest. Hence, despite the large H α flux, the wing flux in both the blue and the red is relatively weaker than in the other lines.

² Note that as the optically-thick radiating layer migrates outward, the optical-thickness of that external shell above it should decrease and eventually vanish. By contrast, line profiles always show narrow line cores and broad line wings, over the 80-day period covering the bright phase of the supernova.

For completeness, we have also included in the bottom panels the predictions for the Paschen and Bracket series. The enhanced scattered flux for high series members is also seen in the Paschen series, but is not so obvious in the Bracket series. This is a key re-

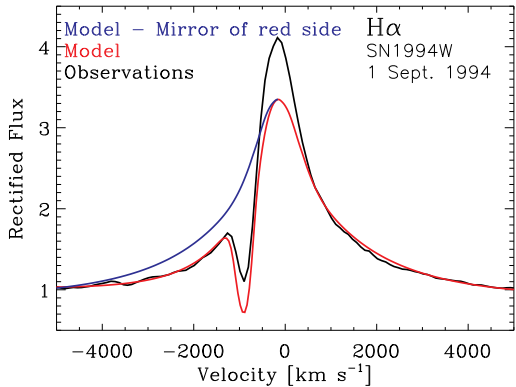


Figure 11. Comparison between the observed (black) and synthetic (red) $H\alpha$ line profile for the 1st of September 1994 (see also Fig. 3). Our model of a single formation region for the continuum and lines reproduces the presence both of a narrow line core (somewhat underestimated) and broad line wings. Numerous line profiles in the spectrum of SN 1994W share this morphology. To illustrate the stronger red wing flux, we mirror the red part of the $H\alpha$ profile and draw it in blue on the blue side.

— $B\alpha$ has a higher optical depth and forms further out in the envelope than does $H\alpha$, and thus exhibits much less obvious electron scattering wings. Observations of Paschen and Brackett lines would help provide key information as to the nature of the broad wings. If the layer is external the fraction of flux in the line wings relative to the line core will be similar for the Balmer and Brackett series, whereas if the electron scattering layer overlaps the line formation region the fraction of line flux in the line wings will be greatest for the Balmer series. In addition, if a significant fraction of the broad wings arise from intrinsic emission by a fast moving shell/envelope, one would anticipate that the broad wings should be easily discernible in $B\alpha$.

To conclude, we find that the strength of the Balmer line profile wings correlates with the electron-scattering optical depth in the corresponding line formation region, the lines forming at greater depths having relatively stronger flux in their wings. In our approach, the broad line wings are thus formed within the photosphere rather than caused by an external optically-thick shell.³ In addition, and unlike C04, we find no need for an extra emission source to contribute to the strength of the broad wings.

6.2 Electron scattering theory

In expanding media, electron-scattering introduces a systematic redshift of line photons in the observer's frame. This is particularly evident in strong spectral lines observed in SNe and hot star spectra. However, to the steep density fall-off in SN ejecta corresponds

³ Another effect could have arisen from the alternate decay channels into transitions that have a lower optical depth. For $H\alpha$, there is no alternate decay route for the upper state but to go into $n = 2$. An $H\beta$ photon can yield a couple of $P\alpha-H\alpha$ photons. For $H\gamma$, there are more options with $P\beta-H\alpha$, $B\alpha-H\beta$, or $B\alpha-P\alpha-H\alpha$. The potential escape allowed through non-coherent electron-scattering for $H\alpha$ could thus be more important compared to higher transitions that have alternate decay routes. If this effect prevailed, the flux in the electron-scattering wings of $H\alpha$ would be stronger relative to higher transitions in the series, and this is not supported by observations.

a steep drop-off in the electron-scattering optical depth, so that generally only a little velocity contrast exists between the emission site of a line photon and the location where it is scattered by a free-electron. Free streaming of such line photons prevails soon above the photosphere. The extent of the red-wing electron-scattering in SN spectral lines is therefore modest, at least in comparison with what is seen in hot star winds and their characteristic $1/R^2$ density distribution.

A second effect, present even in a medium that is globally at rest, is caused by the relatively large thermal velocity ($V_{th,e} = 550\sqrt{T/10^4}$ km s $^{-1}$) of free electrons, even at moderate temperatures. Scattering with free electrons will lead to appreciable Doppler shifts of line photons relative to the narrow intrinsic width of the line which is typically a few km s $^{-1}$ (for an ion with atomic weight A , $V_{Dop} = 12(T/A10^4)$ km s $^{-1}$). Upon scattering out of the line core, the photon may be redistributed in frequency into the line wing where the line optical depth is lower, and thus escape entirely from the line. It is then subject to the electron-scattering opacity which prevents it from free-streaming to infinity; the photon may experience multiple scatterings with free electrons (with blueshifts/redshifts) before escaping. The frequency shifts may add or cancel but the cumulative statistical effect will be to lead to an appreciable flux at many electron Doppler widths from line center, the more so for larger electron-scattering optical depth at the emission site of the photon.

In fast moving SN ejecta, thermal motions are small relative to the expansion velocity; thus the influence on the observed line profiles of incoherent scattering due to the electron thermal motions is small. However, in slower moving SN ejecta the frequency shifts due to the thermal motions of the electrons dominate over that due to expansion, and strong red and blue wings are observed. Lines forming deeper in the photosphere, at higher electron-scattering optical depth, show the strongest wing to peak flux ratio, as observed. Here, these numerous electron-scattering events occur internally to the photosphere, rather than in an outer optically-thick shell.

In our SN models for SN 1994W, two important effects were observed — the profile shape, and to a lesser extent the EW, were strongly dependent on the number of electron scattering iterations that were performed. To understand this finding we first need to explain the computational procedure used to compute the line profiles.

To compute the line profiles we first solve for the atmospheric structure and level populations. These are then used by a separate program, CMF_FLUX (Busche & Hillier 2005), to compute the observed spectrum. For the first iteration, coherent scattering in the comoving frame is assumed. This assumption “conserves” scattered line photons and allows for redistribution effects due to the expansion of the SN envelope. Using the newly computed mean intensity J we now allow for the effects of frequency redistribution by electron scattering using the technique of Rybicki & Hummer (1994), and recompute the mean intensity in the comoving frame. To allow for the effects multiple scattering has on the frequency redistribution of line photons, it is necessary to iterate. For fast moving SNe, two iterations is generally sufficient, but for the slow moving SNe, we sometimes had to perform 10 to 20 iterations to get converged line profiles. For accurate calculations the same Doppler width should be used for both the line-source function and the line profile calculations. However, for normal SNe changes in the adopted Doppler width have only a minor (and well understood) effect on the line profile.

To further assist in understanding the observed behavior we also need to consider the relevant scales for both line formation

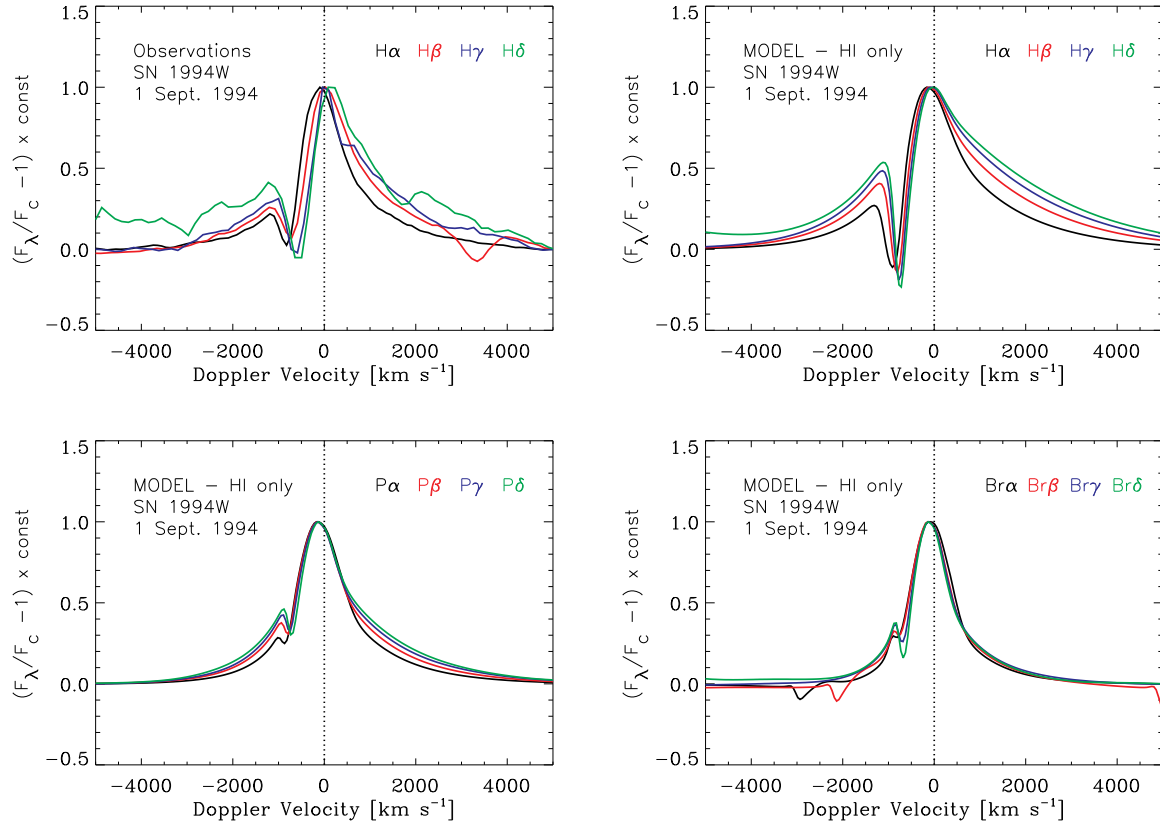


Figure 12. Top: Observed (left) and theoretical (right) Balmer line profiles versus Doppler velocity for the first four terms of the series (α :black; β : red; γ : blue; δ : green). For a better comparison, we use the same ordinate range for the top-left and top-right panels. We also rectify the spectra and normalize to the peak flux for the corresponding line. Bottom: Same as top right, but this time for the Paschen (bottom left) and Brackett (bottom right) series. For this illustration, we use the model for the observations of SN 1994W on 1 September 1994, as shown in Fig. 3, but include only the bound-bound transitions of hydrogen (among the first 30 atomic levels). Note how the flux in the line-profile wings gets relatively stronger compared to the peak value as we move up the Balmer series, from $H\alpha$ to $H\delta$. We find that electron scattering wings are stronger for lines that form at higher optical depth (see Fig. 13). If the profile wings were due to an external scattering layer, the flux in the profile wings would instead scale linearly with the line flux. Note that the blueshifted absorption at ~ 3000 km s^{-1} of $Br\alpha$ and at ~ 2000 km s^{-1} of $Br\beta$ (right panel) are due to $H\alpha$ 4.0198 μm and $H\beta$ 2.6119 μm , respectively.

and electron scattering. Since we have a power law density distribution, with exponent n , the characteristic length scale for electron scattering is $\sim R/(n-1)$. A characteristic scale over which a photon interacts with a line in an expanding medium is the Sobolev length (Sobolev 1960) defined by

$$L_{SOB} = V_{th,eff} / |dV/dR|, \quad (1)$$

where

$$V_{th,eff} = \sqrt{V_{th,i}^2 + V_{turb}^2} \quad (2)$$

is the effective ion thermal velocity, $V_{th,i}$ is the ion thermal velocity, and V_{turb} is a microturbulent velocity that accounts for small-scale turbulent motions. The Sobolev length gives the radial scale over which the velocity changes by $V_{th,eff}$. In other words, it is the approximate size of the resonance zone in which a photon is trapped in a line. In our simulations, we typically adopt $V_{turb} = 50$ km s^{-1} , which spreads the line over a broader frequency range than that given by its intrinsic width of a few km s^{-1} .

In the SN context, we have $L_{SOB}/R_{phot} \approx V_{th,eff}/\beta V_{phot}$. The Sobolev length may thus vary through changes in the velocity gradient (controlled by the parameter β) or in the ejecta ve-

locity (controlled by V_{phot})⁴. In the Type II-P SN 1999em after a few weeks, V_{phot} is on the order of ~ 4000 km s^{-1} , compared to ~ 800 km s^{-1} in SN 1994W. Normalized to R_{phot} and assuming homologous expansion ($\beta = 1$), L_{SOB} is five times larger in SN 1994W compared to SN 1999em.

For SN1994W, $L_{SOB}/R_{phot} = 50/800 = 1/16$ which is only slightly smaller than the electron scattering scale length. As this path length is comparable to the electron scattering scale height, there is a significant probability that a photon will be scattered by an electron within the resonance zone. Further, this can facilitate the escape of line photons as the scattering can effectively “shift” the photon out of the resonance zone by altering its frequency. As we increase L_{SOB} , and assuming a fixed line source function, more photons will be incoherently scattered by electrons in the resonance zone. As most of these photons would normally be destroyed, more photons will escape and the line EW will increase.

⁴ The Sobolev length, in general, varies with direction of photon travel, and for photons traveling perpendicular to the radius vector it is always $RV_{th,eff}/V$, independent of the velocity gradient. For simplicity we retain the formulation above but stress that the average Sobolev length has a much weaker dependence on β than does the radial Sobolev length.

Moreover, since these photons can be subsequently scattered elsewhere, it is necessary to run many iterations to follow their redistribution in frequency space. Because the line EW depends on the adopted Doppler width (and hence Sobolev length) the line source function should be computed using the same Doppler width.⁵

A critical characteristic of Type IIn SNe compared with more normal Type II SNe is their small photospheric velocity, which leads to both a larger Sobolev length, and a larger ratio of $V_{\text{th,eff}}/V_{\text{phot}}$. Both effects facilitate the appearance of broad wings. The larger Sobolev length facilitates the escape of line photons by electron scattering, even from locations where line photons might not normally escape, and potentially at depths where the electron scattering optical depth is still significant. The larger ratio $V_{\text{th,eff}}/V_{\text{phot}}$ makes the incoherent wings due to the thermal motions of the electrons more apparent relative to the observed line width as set by the SN expansion velocity.

We now illustrate these two effects. In Fig. 15, we show a comparison between synthetic $\text{H}\alpha$ line profiles obtained with the model used to fit observations on 11th October 1994, but differing in the adopted values of the base velocity V_0 (the ratio V_{phot}/V_0 is the same in all models; $\beta = 1$ in all cases). Increasing V_0 yields broader line cores, the red wing becomes stronger than the blue wing, and the profile looks increasingly asymmetric. Hence, by merely decreasing V_0 from 1500 km s^{-1} to 500 km s^{-1} , we go from a broad P-Cygni profile typical for a Type II-P SN to a symmetric line profile with a narrow line core and broad wings typical for a Type IIn SN.

In Fig. 16, we show models with different velocity distributions but varying the exponent β entering the velocity law. Recall that reducing β first reduces the maximum velocity, but it also increases the Sobolev length. Hence, by reducing β one can reduce the redistribution of line photons to the red associated with expansion, and increase the importance of electron scattering as a means of escape for line photons. All three models shown in Fig. 16 yield a quasi-symmetric profile that extends from line center out to $\pm 3000 \text{ km s}^{-1}$, although the maximum expansion velocity in the ejecta varies from 4000 , to 1364 , and 1123 km s^{-1} , as we reduce β from 1 , to 0.2 , and 0.01 , respectively. Non-coherent electron scattering is thus the primary line broadening mechanism, so that, paradoxically, the broad line wings testify for slow rather than fast expansion. For smaller β , the blue-wing emission strengthens and arises exclusively from redistribution to the blue of photons in the line core. This occurs at the expense of the line core flux, which indeed decreases correspondingly.

Another element of interest in the observed Balmer line profiles shown in the top left panel of Fig. 12 is the location of the P-Cygni profile dip, which ranges from -900 km s^{-1} for $\text{H}\alpha$ to -500 km s^{-1} for $\text{H}\delta$ on 1 September 1994. The velocity shift of

⁵ All synthetic spectra shown here are computed with a value of 10 km s^{-1} for the turbulent velocity. Note that to limit the computation time, this choice only applies when computing the emergent spectrum from a formal solution of the transfer equation. When solving for the full radiation transport problem including level populations, we assume a turbulent velocity of 50 km s^{-1} , and generally assume that electron-scattering is coherent in the comoving-frame (i.e., we ignore redistribution effects due to the thermal motions of the electrons), so as to allow the linearization of the electron-scattering source function (see Hillier & Miller 1998 for details). Tests we performed show that there is a weak sensitivity of the level populations and the emergent radiation field to variations in the turbulent velocity from 10 to 50 km s^{-1} —the choice of 50 km s^{-1} minimizes computational effort and is numerically advantageous.

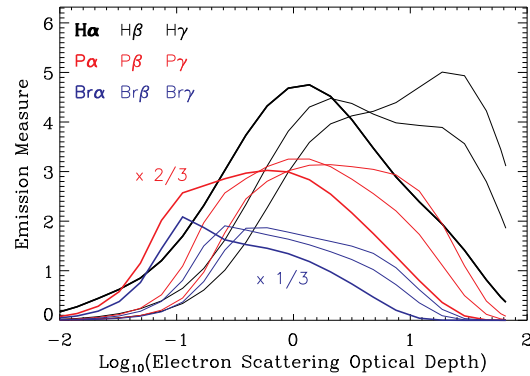


Figure 13. Variation of the emission ζ (Hillier 1987) versus the Log of the electron-scattering optical depth for Balmer (black; scaling of unity), Paschen (red; scaling of $2/3$), and Brackett (blue; scaling of $1/3$) lines for the model shown in Fig. 3. We draw higher series members with thinner lines. The quantity $\zeta(R)$ relates to the total emission interior to R in the line through the integral $\int_{R_0}^R \zeta(R') d \log R'$. $\zeta(R_{\text{Max}})$ is the total emission in the line. Note how the site of emission resides deeper in, i.e., at higher optical depth, for higher energy transitions in each series. There appears to be an increasing outward shift from the Balmer to the Paschen and to the Brackett series. In our synthetic spectra, electron scattering effects are stronger for lines that form deeper in, as observed, and are internal to the photospheric region.

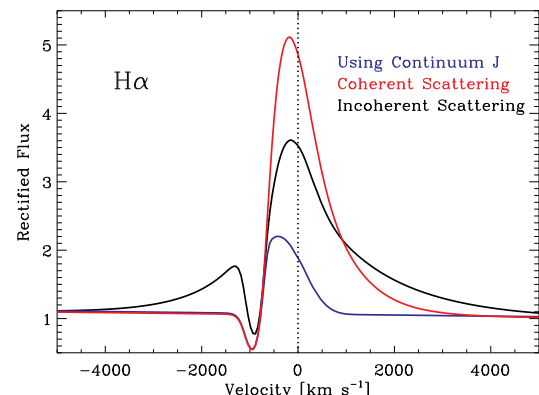


Figure 14. Comparison between the synthetic $\text{H}\alpha$ line profile obtained assuming incoherent (black) or coherent (red) electron scattering in the comoving-frame. In blue, we show the effect of using the continuum (rather than the line) mean intensity when computing the electron-scattering source function, which shows that a large fraction of line photons suffer at least one scattering with free electrons as they escape from their emitting region. For this illustration, we use the same model that fits the observations of SN 1994W on 1 September 1994, whose characteristics are given in Table 1.

this absorption component is well reproduced by our synthetic line profiles, as shown in the top-right panel of Fig. 12. In our modeling approach, which assumes a linearly-increasing velocity with radius, the more optically thick line forms further out, in a region that moves faster, thereby showing a P-Cygni profile absorption further to the blue from line center. In other words, the velocity shift of the absorption minimum amongst the Balmer lines suggests the velocity increases outwards from the photosphere. This is different from the narrow absorption (and sometimes associated narrow emission) that is sometimes seen on top of the strong and broad $\text{H}\alpha$

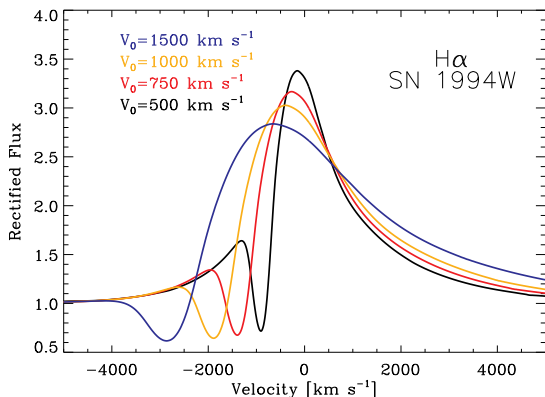


Figure 15. Comparison between synthetic H α line profiles versus Doppler velocity obtained with the model used to fit observations on 11th October 1994, but differing in the adopted values of the base velocity V_0 (the velocity law is of the form $v(R) = V_0(R/R_0)^\beta$). By decreasing V_0 from 1500 km s $^{-1}$ to 500 km s $^{-1}$, we go from a broad P-Cygni profile typical for a Type II-P SN to a symmetric line profile with a narrow line core and broad wings typical for a Type IIn SN. (See text for discussion.)

line profile and that is associated with the CS material exclusively (see Kotak et al. 2004 for the Type Ia SN 2002ic, Smith et al. 2007 for SN 2006gy, and Salamanca et al. 2002 for SN 1997eg).

7 DISCUSSION AND CONCLUSIONS

In this work, we have performed a quantitative spectroscopic analysis of the interacting Type IIn SN 1994W, an unusual Type II event that exhibited narrow line cores with broad line wings in the optical, was unusually luminous, showed erratic spectral behavior prior to peak brightness, and synthesized an extremely low amount of ^{56}Ni . Our study covers specifically from 10-20 days prior to peak until 50 days afterwards, and makes use of a radiative-transfer modeling approach that is one dimensional and steady-state, assumes a (steep) power-law density distribution and a linear velocity law. Importantly, it incorporates non-LTE effects and accurately treats the electron-scattering source function.

During the brightening phase, also characterized by strong spectral variability, we suspect the presence of multiple radiating regions, split between an optically-thick layer contributing to the bulk of the optical light, and shocked (and perhaps clumpy) material above contributing a smaller and rapidly-variable fraction. This fraction is subdominant in the optical but could be much larger in the UV and X-ray ranges. Because this outer material has been shocked to high temperatures, it has a lower density and is thus optically-thin and radiatively less efficient (see Fransson et al. 1996). Such a dichotomy is also supported by the simultaneous presence of optical spectral features testifying for both relatively low and high ionization conditions (i.e., FeII and HeI). Our models during this brightening phase are mostly exploratory, but suggestive of a complex interaction configuration. Observation over a broad spectral band, and extending into at least the near UV, are crucial for understanding these earlier phases.

During the monotonic and slow fading phase, our fits are by contrast very satisfactory. We find that the bolometric light must emerge entirely from a single hydrogen-rich optically-thick layer moving at a near-constant-velocity of ~ 800 km s $^{-1}$. This photosphere recedes in both mass and radius with time, its extent shrink-

ing from 4.3×10^{15} at peak to 2.3×10^{15} cm 50 days later, while cooling modestly from ~ 7300 to ~ 6300 K over that same period. As in Type II-P SNe, the photosphere is slaved to the region of full ionization, which, as the material expands, can only shrink. The steep fading 50 days after the peak is, thus, naturally associated with the emitting material becoming completely optically thin. The near constant photospheric velocity, of ~ 800 km s $^{-1}$, for an extended period (over 60 days), places strong constraints on dynamical models.

As this was a preliminary study, each epoch was modeled independently — we did not attempt to get consistency in the parameters between different dates (i.e., the photospheric density at day 90 is lower than what would be inferred by a power law extrapolation of the photospheric density at day 50). Whether a consistent density/velocity set could be obtained will require a more consistent approach, possibly in conjunction with dynamical modeling. The results of such an investigation would provide crucial constraints on the dynamical model of the emitting region.

By contrast with C04, we do not find that the CDS represents such a key landmark for the understanding of the light coming from SN 1994W. The CDS may be optically-thick at early times, but it must be optically thin after the peak to explain the fading phase of the SN, which would otherwise be a brightening phase given the small photospheric temperature decrease. A corollary is that the steep fading at late times corresponds to the onset of the nebular phase rather than to the CDS leaving the external shell.

We reproduce successfully the narrow-core broad-wing line profile morphology in the optical spectra of SN 1994W at all epochs, thus, downplaying the alleged role of an optically-thick external shell in causing this profile shape. Instead, we find that this hybrid morphology results from the conditions at the photosphere alone. Indeed, we argue that the small photospheric velocity of SN1994W at all times recorded makes electron scattering a key escape mechanism for line photons. The associated frequency kicks redistribute photons from the optically-thick line cores where they are trapped into the more optically-thin line wings, from where they can escape after several scatterings with free electrons. The resulting flux in the wings increases at the expense of the flux in the line core. Paradoxically, the slower the photospheric velocity, the broader and more evident the line wings, which thus reflect the slow rather than the fast expansion of the flow. As C04, we find that the effect is more pronounced for high electron-scattering optical depth, but we associate this effect with the photosphere exclusively, where both lines and continuum form, rather than with an external shell. C04 estimated the properties of this external shell based on estimates of its electron-scattering optical depth through the effect on line profiles. This may need revision since the observed narrow line cores and broad line wings can be understood from multiple-scattering internal to the photosphere.

Let us now speculate on what may be at the origin of the SN 1994W event. The most common Type II SNe, the Type II-P SNe, have a bolometric time-integrated radiation of typically 0.01 B ($1 \text{ B} \equiv 10^{51}$ erg), while the kinetic energy is much larger — on the order of 1 B . The potential to transfer some of this kinetic energy into internal energy (then radiated on a long time scale) offers a means to generate extremely bright events. The extreme brightness of many SNe characterized by narrow lines (e.g. Type IIn) is indeed suggestive that such an interaction takes place. The kinetic energy and mass budget, the conversion efficiency from kinetic to internal energy, and the expected variety of circumstellar material configurations, offers a natural way to explain both the brightness

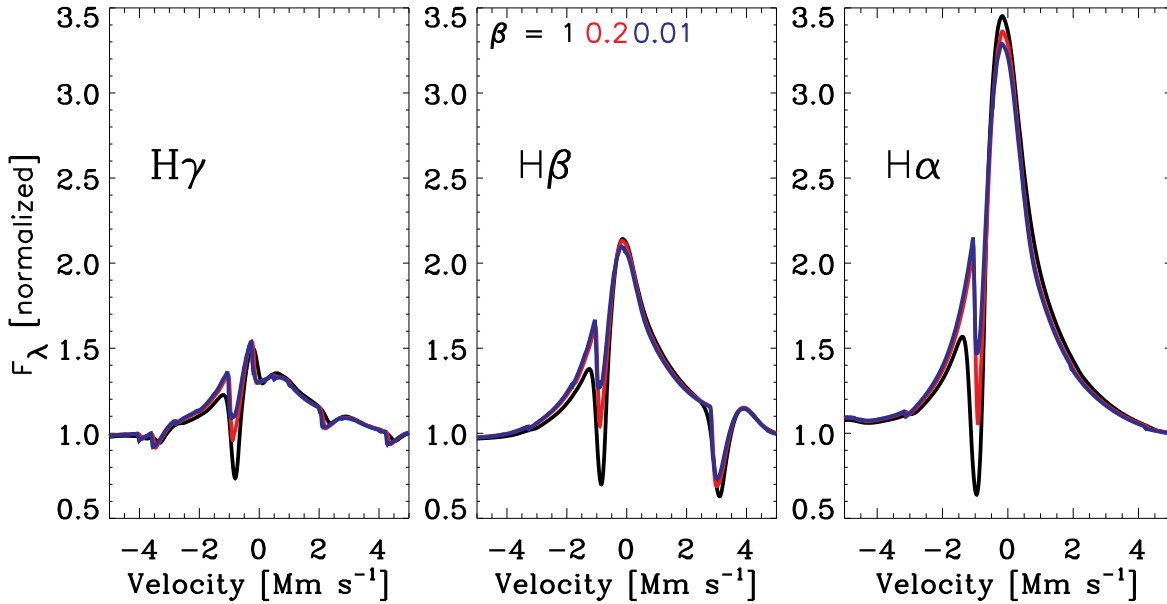


Figure 16. *Left:* Variation of the $H\gamma$ line profile computed for different assumptions on the ejecta velocity distribution, i.e. characterized by $v(R) = V_0(R/R_0)^\beta$, with β equal to 1 (black; $V_{\text{Max}} = 4000 \text{ km s}^{-1}$), 0.2 (red; $V_{\text{Max}} = 1364 \text{ km s}^{-1}$), and 0.01 (blue; $V_{\text{Max}} = 1123 \text{ km s}^{-1}$). *Middle:* Same as left, but this time for $H\beta$. *Right:* Same as left, but this time for $H\alpha$. The reference model with $\beta = 1$ is that used to fit observations of SN 1994W on 1 September 1994 (see Fig. 3 and Table 1). For the latter two models, the base velocity is adjusted so that the photospheric velocity is within 10% of 830 km s^{-1} , thence, producing a similar line core width. Expansion causes little red-wing broadening since these three models, which differ so much in maximum ejecta velocity V_{Max} , show a similar red-wing extent. Effects of non-coherent and multiple scattering by thermal electrons is the primary cause of the extended wings. Note how the profile becomes more symmetric, i.e. shows a stronger blue electron-scattering wing, as β (or the velocity gradient, which controls the escape probability of a photon trapped in the line) is reduced.

and the diversity of Type IIn SNe (see introduction for a short synopsis of this diversity).

What is unclear is whether core collapse is necessarily associated with such SNe. Several critical observations of SN 1994W suggest that we should reexamine this assumption. First, SN 1994W has a very low inferred ^{56}Ni yield, a record low of $0.0026-0.015 \text{ M}_\odot$ (SCL). Second, at no time in the entire spectral evolution do we see broad, SN-like, lines, not even in the nebular phase. Third, the SN was not detected prior to the interaction. The fact that no massive star is known to have a radius larger than 10^{14} cm (RSG, see Levesque et al. 2005), there should be ample time to detect and thoroughly observe the expansion of the inner shell prior to interaction, in fact about $100/V_3$ days (assuming constant velocity expansion). Unfortunately, none of these observations alone are sufficient to rule out a core collapse. For example, a low Ni yield, by itself, does not rule out a core collapse SN. Recent theoretical simulations of $8-10 \text{ M}_\odot$ indicate that these SN can give low Ni yields ($< 0.015 \text{ M}_\odot$) (e.g., Kitaura et al. 2006). SN 2005cs is regarded as a low luminosity SN, is considered to have arisen from a low mass progenitor (e.g., Eldridge et al 2007), and had a low Ni yield of $\sim 0.01 \text{ M}_\odot$ (Pastorello et al. 2006; Tsvetkov et al. 2006).

The observations thus suggest that there might not be any SN ejecta associated with the SN 1994W. C04 inferred the presence of a 0.4 M_\odot CS envelope, while we know that core-collapse SN ejecta have at least 6 M_\odot , typically endowed with 1 B kinetic energy.⁶ Given this unequal mass configuration, it is unlikely the SN ejecta

could be decelerated throughout to velocities below 1000 km s^{-1} . A more favorable configuration for deceleration, supported by the narrow lines at all times, is for two shells of comparable mass. Given the low mass of the CS envelope, this seems to rule out SN ejecta.

An alternative scenario is that SN 1994W is not the result of core-collapse SN ejecta ramming into a CS envelope, but instead the result of the interaction of two shells ejected at 1.5 yr interval. This would not violate any of the energetics involved. The kinetic energy of a shell of mass M moving at constant velocity v is $E_{\text{kin}} \approx 0.01M_1V_3^2B$, where M_1 is the mass in M_\odot , and V_3 is the velocity in 10^3 km s^{-1} . For $M_1=2$ and $V_3=3$, $E_{\text{kin}} \approx 0.2 \text{ B}$. By comparison, adopting a representative luminosity of $2 \times 10^9 \text{ L}_\odot$ over a 100-day period, the time-integrated bolometric light for SN 1994W is $E_{\text{rad}} \approx 0.066 \text{ B}$. With a conversion efficiency of 30%, such a shell-shell interaction would be enough to explain the radiation budget, satisfy the absence of broad lines at all times, and agree with the negligible amount of radioactive isotopes. The mechanism for the ejection of the second shell would be the same one as for the first shell, but the second ejection would have to expand faster to catch up with the first.

The mechanism causing the shell ejections is unknown, but may be related to pulsations or nuclear flashes in the last stages of core burning. For example, within ~ 2 yr of core collapse, 20 M_\odot main-sequence stars go through a ~ 1.5 yr-long oxygen

⁶ Only stars more massive than 8 M_\odot on the main sequence undergo core

collapse, so, leaving aside 2 M_\odot for the neutron star and fallback material leaves us with at least 6 M_\odot . More generic values may be $10-15 \text{ M}_\odot$.

core-burning phase: Instabilities associated with that phase that led to an explosive shell ejection would provide a reproducible time delay before collapse and an attractive mechanism at the origin of some Type IIn SNe like 1994W. Woosley et al. (2007) have invoked the same mechanism, the collision between ejected shells, to explain the extremely luminous supernova SN 2006gy. In the model of Woosley et al. (2007) pair-instability pulsations in massive stars (e.g., $M \sim 110 M_{\odot}$) eject multiple shells which later collide.

Circumstellar envelopes with kinetic energies with $>0.01 B$ ergs are known. In the 1840's, Eta Car underwent a major outburst ejecting over $10 M_{\odot}$ of material at a velocity of 650 km s^{-1} , with greater than $0.04 B$ ergs (Smith et al. 2003). Unfortunately, the duration of the ejection event is not well constrained, and there is no consensus as to the cause of the event. More interestingly, Eta Carinae underwent a second eruption, most likely in the 1890's, although the event was much less significant ($0.1 M_{\odot}$, $V \sim 200 \text{ km s}^{-1}$, $10^{-4} B$; Smith 2003). While the dynamics and kinematics don't satisfy the requirements for a bright circumstellar interaction, they are in the least suggestive that such an interaction might occur. A potential issue with shell ejections from LBVs and similar stars is that the ejection velocities tend to scale with the escape speed. For SN1994, it is likely the second shell needed speeds of order 1500 km s^{-1} , or larger. A direct corollary of the shell interaction scenario is that the progenitor star would not be destroyed (although it might be difficult to detect in the optical if dust formed), and this offers a direct means of distinguishing between the core-collapse and multiple shell-ejection scenarios. Similarly, direct confirmation of Ni/Co decay could be used to distinguish between the two models.

Type IIn SNe gather a very heterogeneous group and our findings should not be applied blindly to other Type IIn SNe. In some cases (e.g., SN 1988Z, Stathakis & Sadler 1991; van Dyk et al. 1993; Turatto et al. 1993; Chugai & Danziger 1994) it is readily apparent that core-collapse SN ejecta, interacting with circumstellar matter, can explain the observed spectral variations. To make further progress, detailed radiation hydrodynamics of the interaction and detailed radiative transfer calculations of emergent spectra need to be performed in partnership, and for a wide range of configurations. Allowance for time-dependent effects and departures from sphericity may also be needed. Observations in the blue (as far to the UV as possible), red, and near IR would provide critical constraints on the models. As a key probe of shocks, X-ray observations are crucial. Finally, public availability of all observational data would help reveal fully the diversity of Type IIn spectra and light curves, thereby helping understand this challenging group of SNe.

ACKNOWLEDGMENTS

We thank Adam Burrows, Rubina Kotak, Jeremiah Murphy, and Steve Smartt for discussion, Robert Cumming for providing the SN 1994W spectroscopic data used here, Nikolai Chugai for his comments, and Stéphane Blondin for a thorough reading of a draft of this paper and for his suggestions. L.D. acknowledges support for this work from the Scientific Discovery through Advanced Computing (SciDAC) program of the DOE, under grant numbers DOE-FC02-01ER41184 and DOE-FC02-06ER41452, and from the NSF under grant number AST-0504947.

Table 1: Line list for model used to match observations on 1 September 1994

λ (Å)	W_λ (Å)	Species	Transition (upper level – lower level)
3213.31	-1.5	FeII	$3d^6 \ 5D \ 4p \ z^4D_{5/2}^o - 3d^7 \ a^4P_{3/2}$
3227.74	-1.6	FeII	$3d^6 \ 5D \ 4p \ z^4D_{7/2}^o - 3d^7 \ a^4P_{5/2}$
3662.26	1.2	HI	30 – 2
3663.40	1.4	HI	29 – 2
3664.68	1.5	HI	28 – 2
3666.09	1.7	HI	27 – 2
3667.68	1.9	HI	26 – 2
3669.46	2.2	HI	25 – 2
3671.47	2.4	HI	24 – 2
3673.76	2.6	HI	23 – 2
3676.36	2.9	HI	22 – 2
3679.35	3.2	HI	21 – 2
3682.81	3.5	HI	20 – 2
3686.83	4.0	HI	19 – 2
3691.55	4.6	HI	18 – 2
3697.15	5.0	HI	17 – 2
3703.85	5.4	HI	16 – 2
3705.02	3.0	HI	$1s7d \ 3D - 1s2p \ 3P^o$
3708.00	1.3	CrIII	$3d^3 \ 4F \ 4p \ 3D_2^o - 3d^3 \ 2P \ 4s \ 3P_1$
3711.97	5.7	HI	15 – 2
3721.94	6.1	HI	14 – 2
3732.88	1.1	HI	$1s7s \ 3S - 1s2p \ 3P^o$
3734.37	6.5	HI	13 – 2
3750.15	6.9	HI	12 – 2
3769.46	2.8	NiII	$3d^8 \ 3F \ 4p \ 4D_{7/2}^o - 3d^8 \ 1D \ 4s \ 2D_{5/2}$
3770.63	7.4	HI	11 – 2
3797.90	8.1	HI	10 – 2
3819.62	3.3	HI	$1s6d \ 3D - 1s2p \ 3P^o$
3835.38	9.0	HI	9 – 2
3853.66	1.5	SiII	$3s^2 \ 1S \ 4p \ 2P_{3/2}^o - 3s3p^2 \ 2D_{3/2}$
3856.02	6.1	SiII	$3s^2 \ 1S \ 4p \ 2P_{3/2}^o - 3s3p^2 \ 2D_{5/2}$
3862.60	4.9	SiII	$3s^2 \ 1S \ 4p \ 2P_{1/2}^o - 3s3p^2 \ 2D_{3/2}$
3867.49	1.8	HI	$1s6s \ 3S - 1s2p \ 3P^o$
3888.64	6.8	HI	$1s3p \ 3P^o - 1s2s \ 3S$
3889.05	10.4	HI	8 – 2
3933.66	3.0	CaII	$3p^6 4p \ 2P_{3/2}^o - 3p^6 4s \ 2S_{1/2}$
3964.73	2.7	HI	$1s4p \ 1P^o - 1s2s \ 1S$
3968.47	3.3	CaII	$3p^6 4p \ 2P_{1/2}^o - 3p^6 4s \ 2S_{1/2}$
3970.07	12.9	HI	7 – 2
4005.04	2.1	FeIII	$3d^5 \ 4G \ 4p \ 3F_4^o - 3d^5 \ 2F_1 \ 4s \ 3F_4$
4009.26	1.5	HI	$1s7d \ 1D - 1s2p \ 1P^o$
4022.35	1.8	FeIII	$3d^5 \ 4G \ 4p \ 3F_3^o - 3d^5 \ 2F_1 \ 4s \ 3F_3$
4026.21	4.0	HI	$1s5d \ 3D - 1s2p \ 3P^o$
4039.16	1.5	FeIII	$3d^5 \ 4G \ 4p \ 3F_2^o - 3d^5 \ 2F_1 \ 4s \ 3F_2$
4101.73	18.1	HI	6 – 2
4120.84	2.8	HI	$1s5s \ 3S - 1s2p \ 3P^o$
4128.06	2.9	SiII	$3s^2 \ 1S \ 4f \ 2F_{5/2}^o - 3s^2 \ 1S \ 3d \ 2D_{3/2}$
4130.90	3.6	SiII	$3s^2 \ 1S \ 4f \ 2F_{7/2}^o - 3s^2 \ 1S \ 3d \ 2D_{5/2}$
4143.76	1.7	HI	$1s6d \ 1D - 1s2p \ 1P^o$
4173.46	1.7	FeII	$3d^6 \ 5D \ 4p \ z^4D_{5/2}^o - 3d^6 \ 3P_2 \ 4s \ b^4P_{5/2}$
4233.17	2.5	FeII	$3d^6 \ 5D \ 4p \ z^4D_{7/2}^o - 3d^6 \ 3P_2 \ 4s \ b^4P_{5/2}$
4340.46	28.0	HI	5 – 2
4351.77	2.2	FeII	$3d^6 \ 5D \ 4p \ z^4D_{5/2}^o - 3d^6 \ 3P_2 \ 4s \ b^4P_{3/2}$
4352.58	2.3	FeIII	$3d^5 \ 6S \ 4p \ 5P_1^o - 3d^5 \ 4P \ 4s \ 5P_2$
4365.64	1.3	FeIII	$3d^5 \ 6S \ 4p \ 5P_1^o - 3d^5 \ 4P \ 4s \ 5P_1$

Table 1 – Continued

λ (Å)	W_λ (Å)	Species	Transition (upper level – lower level)
4371.34	2.4	FeIII	$3d^5 \ 6S \ 4p \ ^5P_2 - 3d^5 \ ^4P \ 4s \ ^5P_3$
4388.15	2.1	HI	$1s5d \ ^1D - 1s2p \ ^1P^o$
4395.76	2.3	FeIII	$3d^5 \ 6S \ 4p \ ^5P_2 - 3d^5 \ ^4P \ 4s \ ^5P_1$
4419.60	3.2	FeIII	$3d^5 \ 6S \ 4p \ ^5P_3 - 3d^5 \ ^4P \ 4s \ ^5P_3$
4431.02	2.4	FeIII	$3d^5 \ 6S \ 4p \ ^5P_3 - 3d^5 \ ^4P \ 4s \ ^5P_2$
4471.50	5.0	HI	$1s4d \ ^3D - 1s2p \ ^3P^o$
4481.13	3.0	MgII	$4f \ ^2F_{7/2} - 3d \ ^2D_{5/2}$
4481.32	2.7	MgII	$4f \ ^2F_{5/2} - 3d \ ^2D_{3/2}$
4508.29	1.4	FeII	$3d^6 \ ^5D \ 4p \ z^4D_{1/2}^o - 3d^6 \ ^3F_2 \ 4s \ b^4F_{3/2}$
4522.63	2.0	FeII	$3d^6 \ ^5D \ 4p \ z^4D_{3/2}^o - 3d^6 \ ^3F_2 \ 4s \ b^4F_{5/2}$
4549.47	3.4	FeII	$3d^6 \ ^5D \ 4p \ z^4D_{5/2}^o - 3d^6 \ ^3F_2 \ 4s \ b^4F_{7/2}$
4555.89	1.3	FeII	$3d^6 \ ^5D \ 4p \ z^4F_{7/2}^o - 3d^6 \ ^3F_2 \ 4s \ b^4F_{7/2}$
4583.84	2.3	FeII	$3d^6 \ ^5D \ 4p \ z^4D_{7/2}^o - 3d^6 \ ^3F_2 \ 4s \ b^4F_{9/2}$
4629.34	1.2	FeII	$3d^6 \ ^5D \ 4p \ z^4F_{9/2}^o - 3d^6 \ ^3F_2 \ 4s \ b^4F_{9/2}$
4713.17	3.6	HI	$1s4s \ ^3S - 1s2p \ ^3P^o$
4815.55	1.4	SII	$3s^2 \ 3p^2 \ ^3P \ 4p \ ^4S_{3/2}^o - 3s^2 \ 3p^2 \ ^3P \ 4s \ ^4P_{5/2}$
4861.32	47.7	HI	4 – 2
4921.93	2.4	HI	$1s4d \ ^1D - 1s2p \ ^1P^o$
4923.93	2.9	FeII	$3d^6 \ ^5D \ 4p \ z^6P_{3/2}^o - 3d^5 \ 4s^2 \ a^6S_{5/2}$
5014.04	1.4	SII	$3s^2 \ 3p^2 \ ^3P \ 4p \ ^2P_{3/2}^o - 3s^2 \ 3p^2 \ ^3P \ 4s \ ^2P_{3/2}$
5015.68	4.6	HI	$1s3p \ ^1P^o - 1s2s \ ^1S$
5018.44	3.4	FeII	$3d^6 \ ^5D \ 4p \ z^6P_{5/2}^o - 3d^5 \ 4s^2 \ a^6S_{5/2}$
5041.04	3.2	SII	$3s^2 \ ^1S \ 4d \ ^2D_{3/2} - 3s^2 \ ^1S \ 4p \ ^2P_{1/2}^o$
5047.74	1.4	HI	$1s4s \ ^1S - 1s2p \ ^1P^o$
5056.00	5.0	SIII	$3s^2 \ ^1S \ 4d \ ^2D_{5/2} - 3s^2 \ ^1S \ 4p \ ^2P_{3/2}^o$
5063.42	1.3	FeIII	$3d^5 \ ^6S \ 4p \ ^5P_1^o - 3d^5 \ ^4D \ 4s \ ^5D_0$
5073.90	2.1	FeIII	$3d^5 \ ^6S \ 4p \ ^5P_1^o - 3d^5 \ ^4D \ 4s \ ^5D_1$
5086.70	1.8	FeIII	$3d^5 \ ^6S \ 4p \ ^5P_1^o - 3d^5 \ ^4D \ 4s \ ^5D_2$
5114.63	1.1	FeIII	$3d^5 \ ^6S \ 4p \ ^5P_2^o - 3d^5 \ ^4D \ 4s \ ^5D_1$
5127.39	3.0	FeIII	$3d^5 \ ^6S \ 4p \ ^5P_2^o - 3d^5 \ ^4D \ 4s \ ^5D_3$
5127.63	2.3	FeIII	$3d^5 \ ^6S \ 4p \ ^5P_2^o - 3d^5 \ ^4D \ 4s \ ^5D_2$
5156.11	4.0	FeIII	$3d^5 \ ^6S \ 4p \ ^5P_3^o - 3d^5 \ ^4D \ 4s \ ^5D_4$
5169.03	4.1	FeII	$3d^6 \ ^5D \ 4p \ z^6P_{7/2}^o - 3d^5 \ 4s^2 \ a^6S_{5/2}$
5193.91	2.1	FeIII	$3d^5 \ ^6S \ 4p \ ^5P_3^o - 3d^5 \ ^4D \ 4s \ ^5D_3$
5197.58	1.2	FeII	$3d^6 \ ^5D \ 4p \ z^4F_{3/2}^o - 3d^6 \ ^3G \ 4s \ a^4G_{5/2}$
5234.62	1.4	FeII	$3d^6 \ ^5D \ 4p \ z^4F_{5/2}^o - 3d^6 \ ^3G \ 4s \ a^4G_{7/2}$
5276.00	1.8	FeII	$3d^6 \ ^5D \ 4p \ z^4F_{7/2}^o - 3d^6 \ ^3G \ 4s \ a^4G_{9/2}$
5316.62	2.3	FeII	$3d^6 \ ^5D \ 4p \ z^4F_{9/2}^o - 3d^6 \ ^3G \ 4s \ a^4G_{11/2}$
5639.98	2.7	SII	$3s^2 \ 3p^2 \ ^3P \ 4p \ ^2D_{5/2}^o - 3s^2 \ 3p^2 \ ^3P \ 4s \ ^2P_{3/2}$
5647.02	1.9	SII	$3s^2 \ 3p^2 \ ^3P \ 4p \ ^2D_{3/2}^o - 3s^2 \ 3p^2 \ ^3P \ 4s \ ^2P_{1/2}$
5875.66	7.4	HI	$1s3d \ ^3D - 1s2p \ ^3P^o$
5978.93	1.7	SIII	$3s^2 \ ^1S \ 5s \ ^2S_{1/2} - 3s^2 \ ^1S \ 4p \ ^2P_{3/2}^o$
6562.79	104.7	HI	3 – 2
6578.05	5.9	CII	$2s2s3p \ ^2P_{3/2}^o - 2s2s3s \ ^2S_{1/2}$
6582.88	4.1	CII	$2s2s3p \ ^2P_{1/2}^o - 2s2s3s \ ^2S_{1/2}$
6678.15	3.0	HI	$1s3d \ ^1D - 1s2p \ ^1P^o$
7065.25	5.1	HI	$1s3s \ ^3S - 1s2p \ ^3P^o$
7281.35	2.0	HI	$1s3s \ ^1S - 1s2p \ ^1P^o$
7771.94	-1.5	OI	$2s^2 \ 2p^3 \ ^4S^o \ 3p \ ^5P_3 - 2s^2 \ 2p^3 \ ^4S^o \ 3s \ ^5S_2^o$
7774.17	-1.1	OI	$2s^2 \ 2p^3 \ ^4S^o \ 3p \ ^5P_2 - 2s^2 \ 2p^3 \ ^4S^o \ 3s \ ^5S_2^o$
7849.72	1.1	SIII	$3s^2 \ ^1S \ 5f \ ^2F_{7/2}^o - 3s^2 \ ^1S \ 4d \ ^2D_{5/2}$
7877.05	5.2	MgII	$4d \ ^2D_{3/2} - 4p \ ^2P_{1/2}^o$
7896.04	1.1	MgII	$4d \ ^2D_{3/2} - 4p \ ^2P_{3/2}^o$
7896.37	8.6	MgII	$4d \ ^2D_{5/2} - 4p \ ^2P_{3/2}^o$
8213.99	2.2	MgII	$5s \ ^2S_{1/2} - 4p \ ^2P_{1/2}^o$

Table 1 – Continued

λ (Å)	W_λ (Å)	Species	Transition (upper level – lower level)
8234.64	5.3	MgII	$5s\ ^2S_{1/2} - 4p\ ^2P_{3/2}^o$
8446.36	1.9	OI	$2s^2 2p^3\ ^4S^o\ 3p\ ^3P_2 - 2s^2 2p^3\ ^4S^o\ 3s\ ^3S_1^o$
8446.76	1.2	OI	$2s^2 2p^3\ ^4S^o\ 3p\ ^3P_1 - 2s^2 2p^3\ ^4S^o\ 3s\ ^3S_1^o$
8467.26	1.1	HI	17 – 3
8502.49	1.3	HI	16 – 3
8545.39	1.6	HI	15 – 3
8598.39	1.9	HI	14 – 3
8665.02	2.3	HI	13 – 3
8750.48	2.8	HI	12 – 3
8862.79	3.6	HI	11 – 3
8927.36	1.4	CaII	$3p^6 4f\ ^2F_{7/2}^o - 3p^6 4d\ ^2D_{5/2}$
9014.91	4.7	HI	10 – 3
9218.25	15.5	MgII	$4p\ ^2P_{3/2}^o - 4s\ ^2S_{1/2}$
9229.02	6.6	HI	9 – 3
9244.26	10.3	MgII	$4p\ ^2P_{1/2}^o - 4s\ ^2S_{1/2}$
9297.27	1.7	FeII	$3d^5\ ^4P\ 4s4p\ ^3P\ ^6D_{9/2}^o - 3d^6\ ^5D\ 5s\ ^6D_{9/2}$
9463.58	1.1	HI	$1s5p\ ^3P^o - 1s3s\ ^3S$
9545.97	9.5	HI	8 – 3
9631.89	1.8	MgII	$5f\ ^2F_{7/2}^o - 4d\ ^2D_{5/2}$
9632.43	1.3	MgII	$5f\ ^2F_{5/2}^o - 4d\ ^2D_{3/2}$
9997.58	2.7	FeII	$3d^5 4s^2\ b^4G_{11/2} - 3d^6\ ^5D\ 4p\ z^4F_{9/2}^o$
10049.37	14.8	HI	7 – 3
10501.50	1.7	FeII	$3d^5 4s^2\ b^4G_{9/2} - 3d^6\ ^5D\ 4p\ z^4F_{7/2}^o$

Table 2: Line list for model used to match observations on 9 September 1994

λ (Å)	W_λ (Å)	Species	Transition (upper level – lower level)
3210.44	-1.4	FII	$3d^6 \ 5D \ 4p \ z^4D_{3/2}^o - 3d^7 \ a^4P_{1/2}$
3213.31	-2.1	FII	$3d^6 \ 5D \ 4p \ z^4D_{5/2}^o - 3d^7 \ a^4P_{3/2}$
3227.74	-2.2	FII	$3d^6 \ 5D \ 4p \ z^4D_{7/2}^o - 3d^7 \ a^4P_{5/2}$
3408.76	-1.2	CrII	$3d^4 \ 5D \ 4p \ z^6D_{5/2}^o - 3d^4 \ 5D \ 4s \ a^4D_{7/2}$
3422.73	-1.0	CrII	$3d^4 \ 5D \ 4p \ z^4P_{3/2}^o - 3d^4 \ 5D \ 4s \ a^4D_{5/2}$
3441.99	-1.1	MnII	$3d^5 \ 6S \ 4p \ z^5P_3^o - 3d^6 \ a^5D_4$
3513.99	-1.3	NiII	$3d^8 \ 3F \ 4p \ 4D_{7/2}^o - 3d^8 \ 3P \ 4s \ 4P_{5/2}$
3662.26	1.2	HI	30 – 2
3663.40	1.4	HI	29 – 2
3664.68	1.6	HI	28 – 2
3666.09	1.8	HI	27 – 2
3667.68	2.0	HI	26 – 2
3669.46	2.2	HI	25 – 2
3671.47	2.5	HI	24 – 2
3673.76	2.7	HI	23 – 2
3676.36	3.0	HI	22 – 2
3679.35	3.2	HI	21 – 2
3682.81	3.5	HI	20 – 2
3686.83	4.0	HI	19 – 2
3691.55	4.5	HI	18 – 2
3697.15	4.9	HI	17 – 2
3703.85	5.3	HI	16 – 2
3705.02	2.2	HeI	$1s7d \ 3D - 1s2p \ 3P^o$
3711.97	5.6	HI	15 – 2
3721.94	6.0	HI	14 – 2
3734.37	6.4	HI	13 – 2
3736.90	1.0	CaII	$3p^6 5s \ 2S_{1/2} - 3p^6 4p \ 2P_{3/2}^o$
3748.48	1.3	FII	$3d^6 \ 3P_2 \ 4p \ z^2P_{3/2}^o - 3d^6 \ 1D_2 \ 4s \ c \ 2D_{5/2}$
3750.15	6.8	HI	12 – 2
3769.46	4.6	NiII	$3d^8 \ 3F \ 4p \ 4D_{7/2}^o - 3d^8 \ 1D \ 4s \ 2D_{5/2}$
3770.63	7.2	HI	11 – 2
3797.90	7.8	HI	10 – 2
3819.62	2.5	HeI	$1s6d \ 3D - 1s2p \ 3P^o$
3835.38	8.7	HI	9 – 2
3853.66	2.1	SiII	$3s^2 \ 1S \ 4p \ 2P_{3/2}^o - 3s3p^2 \ 2D_{3/2}$
3856.02	6.4	SiII	$3s^2 \ 1S \ 4p \ 2P_{3/2}^o - 3s3p^2 \ 2D_{5/2}$
3862.60	5.6	SiII	$3s^2 \ 1S \ 4p \ 2P_{1/2}^o - 3s3p^2 \ 2D_{3/2}$
3867.49	1.4	HeI	$1s6s \ 3S - 1s2p \ 3P^o$
3888.64	5.1	HeI	$1s3p \ 3P^o - 1s2s \ 3S$
3889.05	10.1	HI	8 – 2
3933.66	3.1	CaII	$3p^6 4p \ 2P_{3/2}^o - 3p^6 4s \ 2S_{1/2}$
3964.73	1.9	HeI	$1s4p \ 1P^o - 1s2s \ 1S$
3968.47	3.4	CaII	$3p^6 4p \ 2P_{1/2}^o - 3p^6 4s \ 2S_{1/2}$
3970.07	12.5	HI	7 – 2
4005.04	1.4	FIII	$3d^5 \ 4G \ 4p \ 3F_4^o - 3d^5 \ 2F_1 \ 4s \ 3F_4$
4009.26	1.0	HeI	$1s7d \ 1D - 1s2p \ 1P^o$
4022.35	1.2	FIII	$3d^5 \ 4G \ 4p \ 3F_3^o - 3d^5 \ 2F_1 \ 4s \ 3F_3$
4026.21	2.9	HeI	$1s5d \ 3D - 1s2p \ 3P^o$
4039.16	1.0	FIII	$3d^5 \ 4G \ 4p \ 3F_2^o - 3d^5 \ 2F_1 \ 4s \ 3F_2$
4067.03	1.4	NiII	$3d^8 \ 3F \ 4p \ 2F_{7/2}^o - 3d^8 \ 1G \ 4s^2 Ge_{9/2}$
4101.73	17.8	HI	6 – 2
4120.84	2.0	HeI	$1s5s \ 3S - 1s2p \ 3P^o$
4128.06	2.9	SiII	$3s^2 \ 1S \ 4f \ 2F_{5/2}^o - 3s^2 \ 1S \ 3d \ 2D_{3/2}$
4130.90	3.6	SiII	$3s^2 \ 1S \ 4f \ 2F_{7/2}^o - 3s^2 \ 1S \ 3d \ 2D_{5/2}$
4143.76	1.2	HeI	$1s6d \ 1D - 1s2p \ 1P^o$

Table 2 – Continued

λ (Å)	W_λ (Å)	Species	Transition (upper level – lower level)
4173.46	2.8	FII	$3d^6 \ 5D \ 4p \ z^4D_{5/2}^o - 3d^6 \ 3P_2 \ 4s \ b^4P_{5/2}$
4178.86	1.7	FII	$3d^6 \ 5D \ 4p \ z^4F_{7/2}^o - 3d^6 \ 3P_2 \ 4s \ b^4P_{5/2}$
4233.17	4.0	FII	$3d^6 \ 5D \ 4p \ z^4D_{7/2}^o - 3d^6 \ 3P_2 \ 4s \ b^4P_{5/2}$
4303.18	1.7	FII	$3d^6 \ 5D \ 4p \ z^4D_{3/2}^o - 3d^6 \ 3P_2 \ 4s \ b^4P_{3/2}$
4340.46	27.7	HI	5 – 2
4351.77	3.6	FII	$3d^6 \ 5D \ 4p \ z^4D_{5/2}^o - 3d^6 \ 3P_2 \ 4s \ b^4P_{3/2}$
4352.58	1.7	FIII	$3d^5 \ 6S \ 4p \ 5P_1^o - 3d^5 \ 4P \ 4s \ 5P_2$
4371.34	1.8	FIII	$3d^5 \ 6S \ 4p \ 5P_2^o - 3d^5 \ 4P \ 4s \ 5P_3$
4385.39	1.5	FII	$3d^6 \ 5D \ 4p \ z^4D_{1/2}^o - 3d^6 \ 3P_2 \ 4s \ b^4P_{1/2}$
4388.15	1.4	HeI	$1s5d \ 1D - 1s2p \ 1P^o$
4395.76	1.7	FIII	$3d^5 \ 6S \ 4p \ 5P_2^o - 3d^5 \ 4P \ 4s \ 5P_1$
4416.83	1.4	FII	$3d^6 \ 5D \ 4p \ z^4D_{3/2}^o - 3d^6 \ 3P_2 \ 4s \ b^4P_{1/2}$
4419.60	2.5	FIII	$3d^5 \ 6S \ 4p \ 5P_3^o - 3d^5 \ 4P \ 4s \ 5P_3$
4431.02	1.7	FIII	$3d^5 \ 6S \ 4p \ 5P_3^o - 3d^5 \ 4P \ 4s \ 5P_2$
4471.50	3.6	HeI	$1s4d \ 3D - 1s2p \ 3P^o$
4481.13	2.4	MgII	$4f \ 2F_{7/2}^o - 3d \ 2D_{5/2}$
4481.32	2.2	MgII	$4f \ 2F_{5/2}^o - 3d \ 2D_{3/2}$
4508.29	2.5	FII	$3d^6 \ 5D \ 4p \ z^4D_{1/2}^o - 3d^6 \ 3F_2 \ 4s \ b^4F_{3/2}$
4515.34	1.5	FII	$3d^6 \ 5D \ 4p \ z^4F_{5/2}^o - 3d^6 \ 3F_2 \ 4s \ b^4F_{5/2}$
4520.22	1.3	FII	$3d^6 \ 5D \ 4p \ z^4F_{7/2}^o - 3d^6 \ 3F_2 \ 4s \ b^4F_{9/2}$
4522.63	3.4	FII	$3d^6 \ 5D \ 4p \ z^4D_{3/2}^o - 3d^6 \ 3F_2 \ 4s \ b^4F_{5/2}$
4549.47	5.0	FII	$3d^6 \ 5D \ 4p \ z^4D_{3/2}^o - 3d^6 \ 3F_2 \ 4s \ b^4F_{7/2}$
4555.89	2.3	FII	$3d^6 \ 5D \ 4p \ z^4F_{7/2}^o - 3d^6 \ 3F_2 \ 4s \ b^4F_{7/2}$
4583.84	3.8	FII	$3d^6 \ 5D \ 4p \ z^4D_{7/2}^o - 3d^6 \ 3F_2 \ 4s \ b^4F_{9/2}$
4629.34	2.2	FII	$3d^6 \ 5D \ 4p \ z^4F_{9/2}^o - 3d^6 \ 3F_2 \ 4s \ b^4F_{9/2}$
4713.17	2.6	HeI	$1s4s \ 3S - 1s2p \ 3P^o$
4815.55	1.2	SII	$3s^2 3p^2 \ 3P \ 4p \ 4S_{3/2}^o - 3s^2 3p^2 \ 3P \ 4s \ 4P_{5/2}$
4861.32	47.2	HI	4 – 2
4921.93	1.6	HeI	$1s4d \ 1D - 1s2p \ 1P^o$
4923.93	3.2	FII	$3d^6 \ 5D \ 4p \ z^6P_{3/2}^o - 3d^5 4s^2 \ a^6S_{5/2}$
5014.04	1.3	SII	$3s^2 3p^2 \ 3P \ 4p \ 2P_{3/2}^o - 3s^2 3p^2 \ 3P \ 4s \ 2P_{3/2}$
5015.68	3.3	HeI	$1s3p \ 1P^o - 1s2s \ 1S$
5018.44	3.5	FII	$3d^6 \ 5D \ 4p \ z^6P_{5/2}^o - 3d^5 4s^2 \ a^6S_{5/2}$
5041.04	3.0	SIII	$3s^2 \ 1S \ 4d \ 2D_{3/2} - 3s^2 \ 1S \ 4p \ 2P_{1/2}^o$
5047.74	1.0	HeI	$1s4s \ 1S - 1s2p \ 1P^o$
5056.00	4.5	SIII	$3s^2 \ 1S \ 4d \ 2D_{5/2} - 3s^2 \ 1S \ 4p \ 2P_{3/2}^o$
5073.90	1.5	FIII	$3d^5 \ 6S \ 4p \ 5P_1^o - 3d^5 \ 4D \ 4s \ 5D_1$
5086.70	1.3	FIII	$3d^5 \ 6S \ 4p \ 5P_1^o - 3d^5 \ 4D \ 4s \ 5D_2$
5127.39	2.3	FIII	$3d^5 \ 6S \ 4p \ 5P_2^o - 3d^5 \ 4D \ 4s \ 5D_3$
5127.63	1.7	FIII	$3d^5 \ 6S \ 4p \ 5P_2^o - 3d^5 \ 4D \ 4s \ 5D_2$
5156.11	3.2	FIII	$3d^5 \ 6S \ 4p \ 5P_3^o - 3d^5 \ 4D \ 4s \ 5D_4$
5169.03	3.9	FII	$3d^6 \ 5D \ 4p \ z^6P_{7/2}^o - 3d^5 4s^2 \ a^6S_{5/2}$
5193.91	1.5	FIII	$3d^5 \ 6S \ 4p \ 5P_3^o - 3d^5 \ 4D \ 4s \ 5D_3$
5197.58	2.3	FII	$3d^6 \ 5D \ 4p \ z^4F_{3/2}^o - 3d^6 \ 3G \ 4s \ a^4G_{5/2}$
5234.62	2.6	FII	$3d^6 \ 5D \ 4p \ z^4F_{5/2}^o - 3d^6 \ 3G \ 4s \ a^4G_{7/2}$
5276.00	3.3	FII	$3d^6 \ 5D \ 4p \ z^4F_{7/2}^o - 3d^6 \ 3G \ 4s \ a^4G_{9/2}$
5316.62	3.9	FII	$3d^6 \ 5D \ 4p \ z^4F_{9/2}^o - 3d^6 \ 3G \ 4s \ a^4G_{11/2}$
5639.98	2.4	SII	$3s^2 3p^2 \ 3P \ 4p \ 2D_{5/2}^o - 3s^2 3p^2 \ 3P \ 4s \ 2P_{3/2}$
5647.02	1.7	SII	$3s^2 3p^2 \ 3P \ 4p \ 2D_{3/2}^o - 3s^2 3p^2 \ 3P \ 4s \ 2P_{1/2}$
5875.66	5.1	HeI	$1s3d \ 3D - 1s2p \ 3P^o$
5978.93	1.6	SIII	$3s^2 \ 1S \ 5s \ 2S_{1/2} - 3s^2 \ 1S \ 4p \ 2P_{3/2}^o$
6456.38	1.1	FII	$3d^6 \ 5D \ 4p \ z^4P_{5/2}^o - 3d^6 \ 3D \ 4s \ b^4D_{7/2}$
6562.79	103.6	HI	3 – 2
6578.05	4.3	CII	$2s2s3p \ 2P_{3/2}^o - 2s2s3s \ 2S_{1/2}$
6582.88	2.9	CII	$2s2s3p \ 2P_{1/2}^o - 2s2s3s \ 2S_{1/2}$

Table 2 – Continued

λ (Å)	W_λ (Å)	Species	Transition (upper level – lower level)
6678.15	1.8	HeI	1s3d 1D – 1s2p $^1P^o$
7065.25	3.3	HeI	1s3s 3S – 1s2p $^3P^o$
7281.35	1.2	HeI	1s3s 1S – 1s2p $^1P^o$
7771.94	-1.7	OI	$2s^2 2p^3$ $^4S^o$ 3p 5P_3 – $2s^2 2p^3$ $^4S^o$ 3s $^5S_2^o$
7774.17	-1.3	OI	$2s^2 2p^3$ $^4S^o$ 3p 5P_2 – $2s^2 2p^3$ $^4S^o$ 3s $^5S_2^o$
7848.80	1.0	SiII	$3s^2$ 1S 5f $^2F_{5/2}^o$ – $3s^2$ 1S 4d $^2D_{3/2}$
7849.72	1.4	SiII	$3s^2$ 1S 5f $^2F_{7/2}^o$ – $3s^2$ 1S 4d $^2D_{5/2}$
7877.05	5.8	MgII	4d $^2D_{3/2}$ – 4p $^2P_{1/2}^o$
7896.04	1.3	MgII	4d $^2D_{3/2}$ – 4p $^2P_{3/2}^o$
7896.37	9.4	MgII	4d $^2D_{5/2}$ – 4p $^2P_{3/2}^o$
8213.99	2.3	MgII	5s $^2S_{1/2}$ – 4p $^2P_{1/2}^o$
8234.64	5.3	MgII	5s $^2S_{1/2}$ – 4p $^2P_{3/2}^o$
8437.96	1.0	HI	18 – 3
8446.36	2.0	OI	$2s^2 2p^3$ $^4S^o$ 3p 3P_2 – $2s^2 2p^3$ $^4S^o$ 3s $^3S_1^o$
8446.76	1.2	OI	$2s^2 2p^3$ $^4S^o$ 3p 3P_1 – $2s^2 2p^3$ $^4S^o$ 3s $^3S_1^o$
8467.26	1.2	HI	17 – 3
8502.49	1.4	HI	16 – 3
8545.39	1.6	HI	15 – 3
8598.39	1.9	HI	14 – 3
8665.02	2.3	HI	13 – 3
8750.48	2.8	HI	12 – 3
8862.79	3.5	HI	11 – 3
8912.07	1.1	CaII	$3p^6 4f$ $^2F_{5/2}^o$ – $3p^6 4d$ $^2D_{3/2}$
8927.36	1.6	CaII	$3p^6 4f$ $^2F_{7/2}^o$ – $3p^6 4d$ $^2D_{5/2}$
9014.91	4.5	HI	10 – 3
9218.25	15.3	MgII	4p $^2P_{3/2}^o$ – 4s $^2S_{1/2}$
9229.02	6.3	HI	9 – 3
9244.26	10.8	MgII	4p $^2P_{3/2}^o$ – 4s $^2S_{1/2}$
9297.27	2.0	FII	$3d^5$ 4P 4s4p 3P $^6D_{9/2}^o$ – $3d^6$ 5D 5s $e^6D_{9/2}$
9545.97	9.1	HI	8 – 3
9631.89	2.2	MgII	5f $^2F_{7/2}^o$ – 4d $^2D_{5/2}$
9632.43	1.6	MgII	5f $^2F_{5/2}^o$ – 4d $^2D_{3/2}$
9997.58	4.6	FII	$3d^5 4s^2$ $b^4G_{11/2}$ – $3d^6$ 5D 4p $z^4F_{9/2}^o$
10049.37	14.2	HI	7 – 3
10087.73	1.0	MgII	$5z^2Z$ – 4f $^2F_{7/2}^o$
10366.17	1.1	FII	$3d^6$ 3F_2 4p $y^4G_{11/2}^o$ – $3d^5 4s^2$ $b^4G_{11/2}$
10501.50	3.0	FII	$3d^5 4s^2$ $b^4G_{9/2}$ – $3d^6$ 5D 4p $z^4F_{7/2}^o$

Table 3: Line list for model used to match observations on 1 October 1994

λ (Å)	W_λ (Å)	Species	Transition (upper level – lower level)
3202.54	-3.4	TiIII	$3d^2 \ ^1D \ 4p \ y^2F_{5/2}^o - 3d^2 \ ^1D \ 4s \ a^2D_{3/2}$
3203.44	-1.4	TiIII	$3d^2 \ ^3F \ 4p \ z^2F_{5/2}^o - 3d^2 \ ^3F \ 4s \ a^4F_{3/2}$
3210.44	-5.1	FeII	$3d^6 \ ^5D \ 4p \ z^4D_{3/2}^o - 3d^7 \ a^4P_{1/2}$
3211.08	-1.1	FeII	$3d^6 \ ^3F_2 \ 4p \ x^4D_{7/2}^o - 3d^7 \ b^2F_{5/2}$
3212.02	-2.7	FeII	$3d^6 \ ^3H \ 4p \ z^4I_{9/2}^o - 3d^6 \ ^3G \ 4s \ b^2G_{9/2}$
3213.31	-6.4	FeII	$3d^6 \ ^5D \ 4p \ z^4D_{5/2}^o - 3d^7 \ a^4P_{3/2}$
3214.78	-2.0	TiIII	$3d^2 \ ^3F \ 4p \ z^2F_{7/2}^o - 3d^2 \ ^3F \ 4s \ a^4F_{9/2}$
3217.06	-4.1	TiIII	$3d^2 \ ^3F \ 4p \ z^4F_{9/2}^o - 3d^2 \ ^3F \ 4s \ a^4F_{7/2}$
3218.26	-2.4	TiIII	$3d^2 \ ^1G \ 4p \ y^2G_{7/2}^o - 3d^3 \ a^2H_{9/2}$
3222.84	-4.4	TiIII	$3d^2 \ ^3F \ 4p \ z^4F_{7/2}^o - 3d^2 \ ^3F \ 4s \ a^4F_{5/2}$
3224.24	-2.5	TiIII	$3d^2 \ ^1G \ 4p \ y^2G_{9/2}^o - 3d^3 \ a^2H_{11/2}$
3227.74	-6.6	FeII	$3d^6 \ ^5D \ 4p \ z^4D_{7/2}^o - 3d^7 \ a^4P_{5/2}$
3228.60	-3.0	TiIII	$3d^2 \ ^1D \ 4p \ z^2P_{1/2}^o - 3d^2 \ ^1D \ 4s \ a^2D_{3/2}$
3229.20	-4.0	TiIII	$3d^2 \ ^3F \ 4p \ z^4F_{5/2}^o - 3d^2 \ ^3F \ 4s \ a^4F_{3/2}$
3229.43	-3.1	TiIII	$3d^2 \ ^1D \ 4p \ y^2F_{7/2}^o - 3d^3 \ a^2G_{9/2}$
3231.32	-1.8	TiIII	$3d^2 \ ^3F \ 4p \ z^2D_{5/2}^o - 3d^3 \ b^4F_{7/2}$
3231.71	-2.1	FeII	$3d^6 \ ^3H \ 4p \ z^2G_{7/2}^o - 3d^6 \ ^3D \ 4s \ b^4D_{5/2}$
3232.28	-2.6	TiIII	$3d^2 \ ^1D \ 4p \ y^2F_{5/2}^o - 3d^3 \ a^2G_{7/2}$
3232.78	-2.3	FeII	$3d^6 \ ^3F_2 \ 4p \ z^2F_{5/2}^o - 3d^6 \ ^1G_2 \ 4s \ c^2G_{7/2}$
3234.52	-6.5	TiIII	$3d^2 \ ^3F \ 4p \ z^4F_{9/2}^o - 3d^2 \ ^3F \ 4s \ a^4F_{9/2}$
3234.93	-1.3	FeII	$3d^6 \ ^5D \ 4p \ z^6D_{5/2}^o - 3d^6 \ ^5D \ 4s \ a^4D_{7/2}$
3236.12	-2.6	TiIII	$3d^2 \ ^1D \ 4p \ y^2D_{3/2}^o - 3d^2 \ ^1D \ 4s \ a^2D_{3/2}$
3236.58	-6.0	TiIII	$3d^2 \ ^3F \ 4p \ z^4F_{7/2}^o - 3d^2 \ ^3F \ 4s \ a^4F_{7/2}$
3237.40	-1.8	FeII	$3d^6 \ ^3F_2 \ 4p \ y^4F_{3/2}^o - 3d^6 \ ^3D \ 4s \ b^4D_{3/2}$
3237.82	-2.8	FeII	$3d^6 \ ^3F_2 \ 4p \ y^4F_{3/2}^o - 3d^6 \ ^3D \ 4s \ b^4D_{1/2}$
3239.04	-5.6	TiIII	$3d^2 \ ^3F \ 4p \ z^4F_{5/2}^o - 3d^2 \ ^3F \ 4s \ a^4F_{5/2}$
3239.66	-2.0	TiIII	$3d^2 \ ^1D \ 4p \ y^2D_{3/2}^o - 3d^2 \ ^1D \ 4s \ a^2D_{5/2}$
3241.99	-5.3	TiIII	$3d^2 \ ^3F \ 4p \ z^4F_{3/2}^o - 3d^2 \ ^3F \ 4s \ a^4F_{3/2}$
3243.72	-2.5	FeII	$3d^6 \ ^3F_2 \ 4p \ z^2F_{7/2}^o - 3d^6 \ ^1G_2 \ 4s \ c^2G_{9/2}$
3247.17	-3.0	FeII	$3d^6 \ ^3F_2 \ 4p \ y^4F_{5/2}^o - 3d^6 \ ^3D \ 4s \ b^4D_{3/2}$
3247.39	-1.1	FeII	$3d^6 \ ^3F_2 \ 4p \ z^2F_{7/2}^o - 3d^6 \ ^1G_2 \ 4s \ c^2G_{7/2}$
3248.60	-4.0	TiIII	$3d^2 \ ^3P \ 4p \ y^4D_{7/2}^o - 3d^2 \ ^3P \ 4s \ b^4P_{5/2}$
3248.70	-1.1	TiIII	$3d^2 \ ^3F \ 4p \ z^2D_{3/2}^o - 3d^3 \ b^4F_{5/2}$
3249.37	-2.0	TiIII	$3d^2 \ ^1D \ 4p \ y^2D_{5/2}^o - 3d^2 \ ^1D \ 4s \ a^2D_{3/2}$
3249.66	-1.7	FeII	$3d^6 \ ^3F_2 \ 4p \ y^4F_{5/2}^o - 3d^6 \ ^3D \ 4s \ b^4D_{5/2}$
3249.92	-1.6	FeII	$3d^6 \ ^3P_2 \ 4p \ z^2D_{3/2}^o - 3d^6 \ ^3D \ 4s \ b^4D_{3/2}$
3250.34	-1.2	FeII	$3d^6 \ ^3P_2 \ 4p \ z^2D_{3/2}^o - 3d^6 \ ^3D \ 4s \ b^4D_{1/2}$
3251.92	-3.9	TiIII	$3d^2 \ ^3F \ 4p \ z^4F_{3/2}^o - 3d^2 \ ^3F \ 4s \ a^4F_{5/2}$
3252.92	-4.2	TiIII	$3d^2 \ ^3F \ 4p \ z^4F_{5/2}^o - 3d^2 \ ^3F \ 4s \ a^4F_{7/2}$
3252.94	-2.7	TiIII	$3d^2 \ ^1D \ 4p \ y^2D_{5/2}^o - 3d^2 \ ^1D \ 4s \ a^2D_{5/2}$
3254.25	-3.9	TiIII	$3d^2 \ ^3F \ 4p \ z^4F_{7/2}^o - 3d^2 \ ^3F \ 4s \ a^4F_{9/2}$
3255.89	-4.6	FeII	$3d^6 \ ^5D \ 4p \ z^6D_{7/2}^o - 3d^6 \ ^5D \ 4s \ a^4D_{7/2}$
3258.03	-1.4	FeII	$3d^5 \ ^6S \ 4s4p \ ^3P \ y^6P_{5/2}^o - 3d^6 \ ^3D \ 4s \ b^4D_{3/2}$
3258.77	-3.1	FeII	$3d^6 \ ^3F_2 \ 4p \ y^4F_{7/2}^o - 3d^6 \ ^3D \ 4s \ b^4D_{5/2}$
3259.05	-3.3	FeII	$3d^6 \ ^3F_2 \ 4p \ y^4F_{9/2}^o - 3d^6 \ ^3D \ 4s \ b^4D_{7/2}$
3261.59	-3.3	TiIII	$3d^2 \ ^1G \ 4p \ z^2H_{11/2}^o - 3d^2 \ ^1G \ 4s \ b^2G_{9/2}$
3261.62	-3.3	TiIII	$3d^2 \ ^3P \ 4p \ y^4D_{5/2}^o - 3d^2 \ ^3P \ 4s \ b^4P_{3/2}$
3263.68	-1.4	TiIII	$3d^2 \ ^3P \ 4p \ z^4S_{3/2}^o - 3d^3 \ a^4P_{3/2}$
3264.76	-2.0	FeII	$3d^6 \ ^5D \ 4p \ z^6D_{3/2}^o - 3d^6 \ ^5D \ 4s \ a^4D_{5/2}$
3266.94	-1.5	FeII	$3d^6 \ ^3H \ 4p \ z^4H_{9/2}^o - 3d^6 \ ^3G \ 4s \ b^2G_{9/2}$
3268.51	-1.1	FeII	$3d^6 \ ^3F_2 \ 4p \ y^4G_{5/2}^o - 3d^6 \ ^1G_2 \ 4s \ c^2G_{7/2}$
3271.66	-2.6	TiIII	$3d^2 \ ^3P \ 4p \ y^4D_{5/2}^o - 3d^2 \ ^3P \ 4s \ b^4P_{5/2}$
3272.07	-2.4	TiIII	$3d^2 \ ^3P \ 4p \ y^4D_{3/2}^o - 3d^2 \ ^3P \ 4s \ b^4P_{1/2}$

Table 3 – Continued

λ (Å)	W_λ (Å)	Species	Transition (upper level – lower level)
3276.60	-1.8	FeII	$3d^6 \ ^3H\ 4p\ z^2G_{7/2}^o - 3d^7\ b^2F_{5/2}$
3276.77	-1.9	TiIII	$3d^2\ ^3P\ 4p\ z^4S_{3/2}^o - 3d^3\ a^4P_{5/2}$
3277.35	-4.6	FeII	$3d^6\ ^5D\ 4p\ z^6D_{9/2}^o - 3d^6\ ^5D\ 4s\ a^4D_{7/2}$
3278.29	-2.7	TiIII	$3d^2\ ^3P\ 4p\ y^4D_{3/2}^o - 3d^2\ ^3P\ 4s\ b^4P_{3/2}$
3278.92	-3.3	TiIII	$3d^2\ ^1D\ 4p\ z^2P_{3/2}^o - 3d^2\ ^1D\ 4s\ a^2D_{5/2}$
3279.99	-1.7	TiIII	$3d^2\ ^1D\ 4p\ y^2D_{5/2}^o - 3d^3\ a^2G_{7/2}$
3281.29	-4.0	FeII	$3d^6\ ^5D\ 4p\ z^6D_{5/2}^o - 3d^6\ ^5D\ 4s\ a^4D_{5/2}$
3282.33	-2.4	TiIII	$3d^2\ ^3P\ 4p\ y^4D_{1/2}^o - 3d^2\ ^3P\ 4s\ b^4P_{1/2}$
3285.41	-2.0	FeII	$3d^6\ ^5D\ 4p\ z^6D_{1/2}^o - 3d^6\ ^5D\ 4s\ a^4D_{3/2}$
3287.66	-3.1	TiIII	$3d^2\ ^1G\ 4p\ z^2H_{9/2}^o - 3d^2\ ^1G\ 4s\ b^2G_{7/2}$
3289.35	-2.3	FeII	$3d^6\ ^3H\ 4p\ z^4H_{7/2}^o - 3d^6\ ^3G\ 4s\ b^2G_{7/2}$
3295.23	-1.3	FeII	$3d^6\ ^3P_2\ 4p\ y^4D_{7/2}^o - 3d^6\ ^3D\ 4s\ b^4D_{5/2}$
3295.82	-3.5	FeII	$3d^6\ ^5D\ 4p\ z^6D_{3/2}^o - 3d^6\ ^5D\ 4s\ a^4D_{3/2}$
3296.84	-1.0	FeII	$3d^6\ ^3H\ 4p\ z^2G_{7/2}^o - 3d^7\ b^2F_{7/2}$
3297.88	-1.5	FeII	$3d^6\ ^3P_2\ 4p\ z^2D_{3/2}^o - 3d^7\ b^2F_{5/2}$
3302.86	-2.5	FeII	$3d^6\ ^5D\ 4p\ z^6D_{7/2}^o - 3d^6\ ^5D\ 4s\ a^4D_{5/2}$
3303.46	-3.9	FeII	$3d^6\ ^5D\ 4p\ z^6D_{1/2}^o - 3d^6\ ^5D\ 4s\ a^4D_{1/2}$
3308.81	-2.3	TiIII	$3d^2\ ^3F\ 4p\ z^4F_{9/2}^o - 3d^3\ b^4F_{7/2}$
3313.99	-1.7	FeII	$3d^6\ ^5D\ 4p\ z^6D_{3/2}^o - 3d^6\ ^5D\ 4s\ a^4D_{1/2}$
3315.31	-1.5	TiIII	$3d^2\ ^3P\ 4p\ z^4S_{3/2}^o - 3d^2\ ^3P\ 4s\ b^4P_{1/2}$
3318.02	-2.6	TiIII	$3d^2\ ^3F\ 4p\ z^4F_{7/2}^o - 3d^3\ b^4F_{5/2}$
3321.70	-2.5	TiIII	$3d^2\ ^3P\ 4p\ z^4S_{3/2}^o - 3d^2\ ^3P\ 4s\ b^4P_{3/2}$
3322.94	-4.9	TiIII	$3d^2\ ^3F\ 4p\ z^4F_{9/2}^o - 3d^3\ b^4F_{9/2}$
3323.06	-2.1	FeII	$3d^6\ ^3H\ 4p\ z^2G_{9/2}^o - 3d^7\ b^2F_{7/2}$
3326.78	-2.4	TiIII	$3d^2\ ^3F\ 4p\ z^4F_{5/2}^o - 3d^3\ b^4F_{3/2}$
3329.11	-1.1	FeII	$3d^6\ ^3H\ 4p\ z^4I_{9/2}^o - 3d^6\ ^3D\ 4s\ b^4D_{7/2}$
3329.45	-4.5	TiIII	$3d^2\ ^3F\ 4p\ z^4F_{7/2}^o - 3d^3\ b^4F_{7/2}$
3332.11	-2.9	TiIII	$3d^2\ ^3P\ 4p\ z^4S_{3/2}^o - 3d^2\ ^3P\ 4s\ b^4P_{5/2}$
3335.20	-4.1	TiIII	$3d^2\ ^3F\ 4p\ z^4F_{5/2}^o - 3d^3\ b^4F_{5/2}$
3338.52	-1.3	FeII	$3d^6\ ^3P_2\ 4p\ y^4P_{3/2}^o - 3d^6\ ^3D\ 4s\ b^4D_{5/2}$
3340.36	-3.8	TiIII	$3d^2\ ^3F\ 4p\ z^4F_{3/2}^o - 3d^3\ b^4F_{3/2}$
3341.88	-4.3	TiIII	$3d^2\ ^3F\ 4p\ z^2G_{7/2}^o - 3d^2\ ^3F\ 4s\ a^2F_{5/2}$
3343.77	-2.2	TiIII	$3d^2\ ^3F\ 4p\ z^4F_{7/2}^o - 3d^3\ b^4F_{9/2}$
3346.75	-2.5	TiIII	$3d^2\ ^3F\ 4p\ z^4F_{5/2}^o - 3d^3\ b^4F_{7/2}$
3348.85	-2.2	TiIII	$3d^2\ ^3F\ 4p\ z^4F_{3/2}^o - 3d^3\ b^4F_{5/2}$
3349.04	-4.5	TiIII	$3d^2\ ^3F\ 4p\ z^2G_{9/2}^o - 3d^2\ ^3F\ 4s\ a^2F_{7/2}$
3349.41	-5.2	TiIII	$3d^2\ ^3F\ 4p\ z^4G_{11/2}^o - 3d^2\ ^3F\ 4s\ a^4F_{9/2}$
3350.42	-1.2	NiIII	$3d^8\ ^3F\ 4p\ z^4D_{3/2}^o - 3d^8\ ^1D\ 4s\ ^2D_{3/2}$
3361.22	-5.0	TiIII	$3d^2\ ^3F\ 4p\ z^4G_{9/2}^o - 3d^2\ ^3F\ 4s\ a^4F_{7/2}$
3372.21	-1.6	TiIII	$3d^2\ ^3F\ 4p\ z^2G_{7/2}^o - 3d^2\ ^3F\ 4s\ a^2F_{7/2}$
3372.80	-4.7	TiIII	$3d^2\ ^3F\ 4p\ z^4G_{7/2}^o - 3d^2\ ^3F\ 4s\ a^4F_{5/2}$
3373.97	-1.8	NiIII	$3d^8\ ^3F\ 4p\ z^4D_{5/2}^o - 3d^8\ ^3P\ 4s\ ^4P_{5/2}$
3380.28	-3.3	TiIII	$3d^2\ ^3F\ 4p\ z^4G_{9/2}^o - 3d^2\ ^3F\ 4s\ a^4F_{9/2}$
3381.36	-1.5	FeII	$3d^6\ ^5D\ 4p\ z^6P_{5/2}^o - 3d^7\ a^4P_{3/2}$
3383.77	-4.5	TiIII	$3d^2\ ^3F\ 4p\ z^4G_{5/2}^o - 3d^2\ ^3F\ 4s\ a^4F_{3/2}$
3387.30	-1.0	FeII	$3d^6\ ^3H\ 4p z^4I_{9/2}^o - 3d^7\ b^2F_{7/2}$
3387.85	-3.4	TiIII	$3d^2\ ^3F\ 4p\ z^4G_{7/2}^o - 3d^2\ ^3F\ 4s\ a^4F_{7/2}$
3394.58	-3.2	TiIII	$3d^2\ ^3F\ 4p\ z^4G_{5/2}^o - 3d^2\ ^3F\ 4s\ a^4F_{5/2}$
3407.30	-1.7	NiIII	$3d^8\ ^3F\ 4p\ z^4D_{1/2}^o - 3d^8\ ^3P\ 4s\ ^4P_{1/2}$
3416.02	-2.4	FeII	$3d^6\ ^5D\ 4p\ z^4P_{1/2}^o - 3d^7\ a^2P_{3/2}$
3425.57	-1.4	FeII	$3d^6\ ^5D\ 4p\ z^6P_{7/2}^o - 3d^7\ a^2P_{5/2}$
3436.11	-1.1	FeII	$3d^6\ ^3P_2\ 4p\ z^2D_{5/2}^o - 3d^7\ b^2F_{7/2}$
3443.83	-1.8	FeII	$3d^6\ ^5D\ 4p\ z^4P_{3/2}^o - 3d^7\ a^2P_{3/2}$
3444.31	-2.7	TiIII	$3d^2\ ^3F\ 4p\ z^4G_{11/2}^o - 3d^3\ b^4F_{9/2}$

Table 3 – Continued

λ (Å)	W_λ (Å)	Species	Transition (upper level – lower level)
3454.16	-1.5	NiII	$3d^8 \ ^3F \ 4p \ ^4D_{5/2}^o - 3d^8 \ ^1D \ 4s \ ^2D_{3/2}$
3456.39	-1.7	TiIII	$3d^2 \ ^3P \ 4p \ y^2P_{3/2}^o - 3d^2 \ ^3P \ 4s \ b^2P_{3/2}$
3456.92	-1.2	FeII	$3d^6 \ ^3P_2 \ 4p \ y^4P_{5/2}^o - 3d^6 \ ^3D \ 4s \ b^4D_{7/2}$
3461.49	-2.5	TiIII	$3d^2 \ ^3F \ 4p \ z^4G_{9/2}^o - 3d^3 \ b^4F_{7/2}$
3465.64	-1.6	NiII	$3d^8 \ ^3F \ 4p \ ^4D_{3/2}^o - 3d^8 \ ^3P \ 4s \ ^4P_{3/2}$
3468.68	-1.8	FeII	$3d^6 \ ^3H \ 4p z^2G_{7/2}^o - 3d^6 \ ^1G_2 \ 4s \ c^2G_{7/2}$
3471.39	-1.6	NiII	$3d^8 \ ^3F \ 4p \ ^4D_{3/2}^o - 3d^8 \ ^3P \ 4s \ ^4P_{1/2}$
3475.74	-1.3	FeII	$3d^6 \ ^5D \ 4p \ z^6F_{7/2}^o - 3d^7 \ a^4P_{5/2}$
3477.19	-2.3	TiIII	$3d^2 \ ^3F \ 4p \ z^4G_{7/2}^o - 3d^3 \ b^4F_{5/2}$
3479.91	-1.6	FeII	$3d^6 \ ^5D \ 4p \ z^6F_{3/2}^o - 3d^7 \ a^4P_{3/2}$
3487.99	-1.1	FeII	$3d^6 \ ^5D \ 4p \ z^6F_{5/2}^o - 3d^7 \ a^4P_{3/2}$
3491.07	-2.1	TiIII	$3d^2 \ ^3F \ 4p z^4G_{5/2}^o - 3d^3 \ b^4F_{3/2}$
3493.47	-2.3	FeII	$3d^6 \ ^3H \ 4p z^2G_{9/2}^o - 3d^6 \ ^1G_2 \ 4s \ c^2G_{9/2}$
3494.67	-2.1	FeII	$3d^6 \ ^5D \ 4p \ z^4P_{5/2}^o - 3d^7 \ a^2P_{3/2}$
3503.47	-1.2	FeII	$3d^6 \ ^5D \ 4p \ z^6F_{1/2}^o - 3d^7 \ a^4P_{1/2}$
3504.90	-2.8	TiIII	$3d^2 \ ^1G \ 4p \ y^2G_{9/2}^o - 3d^2 \ ^1G \ 4s \ b^2G_{9/2}$
3507.40	-1.5	FeII	$3d^6 \ ^5D \ 4p \ z^4P_{3/2}^o - 3d^7 \ a^2P_{1/2}$
3510.84	-2.6	TiIII	$3d^2 \ ^1G \ 4p \ y^2G_{7/2}^o - 3d^2 \ ^1G \ 4s \ b^2G_{7/2}$
3513.99	-2.4	NiII	$3d^8 \ ^3F \ 4p \ ^4D_{7/2}^o - 3d^8 \ ^3P \ 4s \ ^4P_{5/2}$
3520.26	-1.5	TiIII	$3d^2 \ ^3P \ 4p \ x^2D_{3/2}^o - 3d^2 \ ^3P \ 4s \ b^2P_{1/2}$
3535.41	-1.8	TiIII	$3d^2 \ ^3P \ 4p \ x^2D_{5/2}^o - 3d^2 \ ^3P \ 4s \ b^2P_{3/2}$
3564.53	-1.3	FeII	$3d^6 \ ^3H \ 4p \ z^4I_{9/2}^o - 3d^6 \ ^1G_2 \ 4s \ c^2G_{9/2}$
3573.73	-1.0	TiIII	$3d^2 \ ^3F \ 4p \ z^4D_{3/2}^o - 3d^2 \ ^3F \ 4s \ a^2F_{5/2}$
3576.76	-1.8	NiII	$3d^8 \ ^3F \ 4p \ ^4D_{5/2}^o - 3d^8 \ ^3P \ 4s \ ^4P_{3/2}$
3596.05	-1.9	TiIII	$3d^2 \ ^3F \ 4p \ z^4D_{5/2}^o - 3d^2 \ ^3F \ 4s \ a^2F_{7/2}$
3608.81	-1.0	NiII	$3d^8 \ ^3F \ 4p \ ^4D_{5/2}^o - 3d^8 \ ^1D \ 4s \ ^2D_{5/2}$
3624.82	-1.6	TiIII	$3d^2 \ ^3P \ 4p \ z^2S_{1/2}^o - 3d^3 \ a^2P_{1/2}$
3641.33	-2.0	TiIII	$3d^2 \ ^3P \ 4p \ z^2S_{1/2}^o - 3d^3 \ a^2P_{3/2}$
3662.26	1.0	HI	30 – 2
3663.40	1.2	HI	29 – 2
3664.68	1.4	HI	28 – 2
3666.09	1.6	HI	27 – 2
3667.68	1.8	HI	26 – 2
3669.46	1.9	HI	25 – 2
3671.47	2.1	HI	24 – 2
3673.76	2.2	HI	23 – 2
3676.36	2.3	HI	22 – 2
3679.35	2.4	HI	21 – 2
3682.81	2.5	HI	20 – 2
3686.83	2.6	HI	19 – 2
3691.55	2.7	HI	18 – 2
3697.15	2.8	HI	17 – 2
3703.85	2.8	HI	16 – 2
3706.02	1.9	CaII	$3p^6 5s \ ^2S_{1/2} - 3p^6 4p \ ^2P_{1/2}^o$
3711.97	2.8	HI	15 – 2
3721.94	2.8	HI	14 – 2
3734.37	2.8	HI	13 – 2
3736.90	2.6	CaII	$3p^6 5s \ ^2S_{1/2} - 3p^6 4p \ ^2P_{3/2}^o$
3748.48	1.5	FeII	$3d^6 \ ^3P_2 \ 4p \ z^2P_{3/2}^o - 3d^6 \ ^1D_2 \ 4s \ c \ ^2D_{5/2}$
3750.15	2.8	HI	12 – 2
3769.46	2.8	NiII	$3d^8 \ ^3F \ 4p \ ^4D_{7/2}^o - 3d^8 \ ^1D \ 4s \ ^2D_{5/2}$
3770.63	2.8	HI	11 – 2
3783.35	1.0	FeII	$3d^6 \ ^5D \ 4p \ z^4D_{5/2}^o - 3d^7 \ a^2P_{3/2}$
3797.90	3.0	HI	10 – 2
3835.38	3.3	HI	9 – 2

Table 3 – Continued

λ (Å)	W_λ (Å)	Species	Transition (upper level – lower level)
3845.18	1.1	FeII	$3d^6 \ ^3P_2 4p \ z^2D_{3/2}^o - 3d^6 \ ^3D \ 4s \ b^2D_{3/2}$
3849.55	1.5	NiIII	$3d^8 \ ^3F \ 4p \ ^2F_{5/2}^o - 3d^8 \ ^1G \ 4s^2G_{7/2}$
3853.66	2.1	SiIII	$3s^2 \ ^1S \ 4p \ ^2P_{3/2}^o - 3s3p^2 \ ^2D_{3/2}$
3856.02	1.5	SiIII	$3s^2 \ ^1S \ 4p \ ^2P_{3/2}^o - 3s3p^2 \ ^2D_{5/2}$
3862.60	1.8	SiIII	$3s^2 \ ^1S \ 4p \ ^2P_{1/2}^o - 3s3p^2 \ ^2D_{3/2}$
3888.64	1.6	HI	$1s3p \ ^3P^o - 1s2s \ ^3S$
3889.05	3.9	HI	$8 - 2$
3914.50	1.6	FeII	$3d^6 \ ^5D \ 4p \ z^6D_{3/2}^o - 3d^7 \ a^4P_{5/2}$
3930.30	1.7	FeII	$3d^6 \ ^5D \ 4p \ z^6D_{1/2}^o - 3d^7 \ a^4P_{3/2}$
3933.66	3.0	CaII	$3p^64p \ ^2P_{3/2}^o - 3p^64s \ ^2S_{1/2}$
3938.29	2.1	FeII	$3d^6 \ ^5D \ 4p \ z^6D_{5/2}^o - 3d^7 \ a^4P_{5/2}$
3945.21	1.3	FeII	$3d^6 \ ^5D \ 4p \ z^6D_{3/2}^o - 3d^7 \ a^4P_{3/2}$
3968.47	3.4	CaII	$3p^64p \ ^2P_{1/2}^o - 3p^64s \ ^2S_{1/2}$
3969.39	2.5	FeII	$3d^6 \ ^5D \ 4p \ z^6D_{7/2}^o - 3d^7 \ a^4P_{5/2}$
3970.07	5.2	HI	$7 - 2$
3974.17	1.0	FeII	$3d^6 \ ^5D \ 4p \ z^4P_{5/2}^o - 3d^6 \ ^3P_2 \ 4s \ b^4P_{3/2}$
4002.08	1.0	FeII	$3d^6 \ ^5D \ 4p \ z^4P_{3/2}^o - 3d^6 \ ^3P_2 \ 4s \ b^4P_{1/2}$
4015.47	1.0	NiIII	$3d^8 \ ^3F \ 4p \ ^2D_{5/2}^o - 3d^8 \ ^1G \ 4s^2G_{7/2}$
4024.55	1.2	FeII	$3d^6 \ ^3P_2 \ 4p \ z^2D_{5/2}^o - 3d^6 \ ^3D \ 4s \ b^2D_{5/2}$
4067.03	2.3	NiIII	$3d^8 \ ^3F \ 4p \ ^2F_{7/2}^o - 3d^8 \ ^1G \ 4s^2G_{9/2}$
4075.95	1.7	FeII	$3d^6 \ ^5D \ 4p \ z^4D_{3/2}^o - 3d^7 \ a^2D_{5/2}$
4101.73	7.9	HI	$6 - 2$
4122.67	1.7	FeII	$3d^6 \ ^5D \ 4p \ z^4F_{5/2}^o - 3d^6 \ ^3P_2 \ 4s \ b^4P_{5/2}$
4128.75	1.0	FeII	$3d^6 \ ^5D \ 4p \ z^4D_{3/2}^o - 3d^6 \ ^3P_2 \ 4s \ b^4P_{5/2}$
4173.46	2.9	FeII	$3d^6 \ ^5D \ 4p \ z^4D_{5/2}^o - 3d^6 \ ^3P_2 \ 4s \ b^4P_{5/2}$
4177.69	1.3	FeII	$3d^6 \ ^5D \ 4p \ z^4D_{7/2}^o - 3d^7 \ a^2D_{5/2}$
4178.86	2.9	FeII	$3d^6 \ ^5D \ 4p \ z^4F_{7/2}^o - 3d^6 \ ^3P_2 \ 4s \ b^4P_{5/2}$
4180.98	2.6	FeII	$3d^6 \ ^3P_2 \ 4p \ z^2D_{3/2}^o - 3d^6 \ ^1D \ 4s \ c \ ^2D_{3/2}$
4233.17	3.3	FeII	$3d^6 \ ^5D \ 4p \ z^4D_{7/2}^o - 3d^6 \ ^3P_2 \ 4s \ b^4P_{5/2}$
4258.15	2.0	FeII	$3d^6 \ ^5D \ 4p \ z^4F_{3/2}^o - 3d^6 \ ^3P_2 \ 4s \ b^4P_{3/2}$
4273.33	2.3	FeII	$3d^6 \ ^5D \ 4p \ z^4D_{1/2}^o - 3d^6 \ ^3P_2 \ 4s \ b^4P_{3/2}$
4278.16	1.1	FeII	$3d^6 \ ^5D \ 4p \ z^4F_{5/2}^o - 3d^6 \ ^3H \ 4s \ a^4H_{7/2}$
4290.22	1.0	TiIII	$3d^2 \ ^3F \ 4p \ z^4D_{5/2}^o - 3d^3 \ a^4P_{3/2}$
4296.57	2.9	FeII	$3d^6 \ ^5D \ 4p \ z^4F_{5/2}^o - 3d^6 \ ^3P_2 \ 4s \ b^4P_{3/2}$
4300.05	1.5	TiIII	$3d^2 \ ^3F \ 4p \ z^4D_{7/2}^o - 3d^3 \ a^4P_{5/2}$
4303.18	3.6	FeII	$3d^6 \ ^5D \ 4p \ z^4D_{3/2}^o - 3d^6 \ ^3P_2 \ 4s \ b^4P_{3/2}$
4314.31	1.9	FeII	$3d^6 \ ^5D \ 4p \ z^4F_{7/2}^o - 3d^6 \ ^3H \ 4s \ a^4H_{9/2}$
4340.46	13.5	HI	$5 - 2$
4351.77	4.0	FeII	$3d^6 \ ^5D \ 4p \ z^4D_{5/2}^o - 3d^6 \ ^3P_2 \ 4s \ b^4P_{3/2}$
4369.41	1.4	FeII	$3d^6 \ ^5D \ 4p \ z^4F_{3/2}^o - 3d^6 \ ^3P_2 \ 4s \ b^4P_{1/2}$
4384.32	2.1	FeII	$3d^6 \ ^5D \ 4p \ z^4F_{9/2}^o - 3d^6 \ ^3H \ 4s \ a^4H_{11/2}$
4385.39	3.9	FeII	$3d^6 \ ^5D \ 4p \ z^4D_{1/2}^o - 3d^6 \ ^3P_2 \ 4s \ b^4P_{1/2}$
4395.03	1.2	TiIII	$3d^2 \ ^3F \ 4p \ z^2F_{7/2}^o - 3d^2 \ ^1D \ 4s \ a^2D_{5/2}$
4413.60	1.2	FeII	$3d^6 \ ^5D \ 4p \ z^4F_{9/2}^o - 3d^6 \ ^3H \ 4s \ a^4H_{9/2}$
4416.83	4.0	FeII	$3d^6 \ ^5D \ 4p \ z^4D_{3/2}^o - 3d^6 \ ^3P_2 \ 4s \ b^4P_{1/2}$
4443.79	1.3	TiIII	$3d^2 \ ^3F \ 4p \ z^2F_{5/2}^o - 3d^2 \ ^1D \ 4s \ a^2D_{3/2}$
4468.51	1.4	TiIII	$3d^2 \ ^3F \ 4p \ z^2F_{7/2}^o - 3d^3 \ a^2G_{9/2}$
4472.93	2.1	FeII	$3d^6 \ ^5D \ 4p \ z^4F_{3/2}^o - 3d^6 \ ^3F_2 \ 4s \ b^4F_{5/2}$
4481.13	1.3	MgII	$4f \ ^2F_{7/2}^o - 3d \ ^2D_{5/2}$
4481.32	1.4	MgII	$4f \ ^2F_{5/2}^o - 3d \ ^2D_{3/2}$
4489.18	3.4	FeII	$3d^6 \ ^5D \ 4p \ z^4F_{5/2}^o - 3d^6 \ ^3F_2 \ 4s \ b^4F_{7/2}$
4491.41	3.9	FeII	$3d^6 \ ^5D \ 4p \ z^4F_{3/2}^o - 3d^6 \ ^3F_2 \ 4s \ b^4F_{3/2}$
4501.27	1.4	TiIII	$3d^2 \ ^3F \ 4p \ z^2F_{5/2}^o - 3d^3 \ a^2G_{7/2}$
4508.29	4.4	FeII	$3d^6 \ ^5D \ 4p \ z^4D_{1/2}^o - 3d^6 \ ^3F_2 \ 4s \ b^4F_{3/2}$

Continued on Next Page...

Table 3 – Continued

λ (Å)	W_λ (Å)	Species	Transition (upper level – lower level)
4515.34	4.3	FeII	$3d^6 \ ^5D \ 4p \ z^4F_{5/2}^o - 3d^6 \ ^3F_2 \ 4s \ b^4F_{5/2}$
4520.22	4.2	FeII	$3d^6 \ ^5D \ 4p \ z^4F_{7/2}^o - 3d^6 \ ^3F_2 \ 4s \ b^4F_{9/2}$
4522.63	4.5	FeII	$3d^6 \ ^5D \ 4p \ z^4D_{3/2}^o - 3d^6 \ ^3F_2 \ 4s \ b^4F_{5/2}$
4533.97	2.2	TiIII	$3d^2 \ ^3F \ 4p \ z^2D_{5/2}^o - 3d^3 \ a^2P_{3/2}$
4534.17	2.1	FeII	$3d^6 \ ^5D \ 4p \ z^4F_{5/2}^o - 3d^6 \ ^3F_2 \ 4s \ b^4F_{3/2}$
4541.52	3.4	FeII	$3d^6 \ ^5D \ 4p \ z^4D_{3/2}^o - 3d^6 \ ^3F_2 \ 4s \ b^4F_{3/2}$
4549.47	4.7	FeII	$3d^6 \ ^5D \ 4p \ z^4D_{5/2}^o - 3d^6 \ ^3F_2 \ 4s \ b^4F_{7/2}$
4549.62	2.9	TiIII	$3d^2 \ ^3F \ 4p \ z^2G_{9/2}^o - 3d^3 \ a^2H_{11/2}$
4555.89	4.6	FeII	$3d^6 \ ^5D \ 4p \ z^4F_{7/2}^o - 3d^6 \ ^3F_2 \ 4s \ b^4F_{7/2}$
4563.76	1.9	TiIII	$3d^2 \ ^3F \ 4p \ z^2D_{3/2}^o - 3d^3 \ a^2P_{1/2}$
4571.97	2.8	TiIII	$3d^2 \ ^3F \ 4p \ z^2G_{7/2}^o - 3d^3 \ a^2H_{9/2}$
4576.34	3.5	FeII	$3d^6 \ ^5D \ 4p \ z^4D_{5/2}^o - 3d^6 \ ^3F_2 \ 4s \ b^4F_{5/2}$
4580.06	2.1	FeII	$3d^6 \ ^5D \ 4p \ z^6P_{7/2}^o - 3d^6 \ ^3P_2 \ 4s \ b^4P_{5/2}$
4582.84	3.4	FeII	$3d^6 \ ^5D \ 4p \ z^4F_{7/2}^o - 3d^6 \ ^3F_2 \ 4s \ b^4F_{5/2}$
4583.84	4.9	FeII	$3d^6 \ ^5D \ 4p \ z^4D_{7/2}^o - 3d^6 \ ^3F_2 \ 4s \ b^4F_{9/2}$
4620.52	3.0	FeII	$3d^6 \ ^5D \ 4p \ z^4D_{7/2}^o - 3d^6 \ ^3F_2 \ 4s \ b^4F_{7/2}$
4629.34	4.9	FeII	$3d^6 \ ^5D \ 4p \ z^4F_{9/2}^o - 3d^6 \ ^3F_2 \ 4s \ b^4F_{9/2}$
4656.98	1.0	FeII	$3d^6 \ ^5D \ 4p \ z^4D_{5/2}^o - 3d^5 \ 4s^2 \ a^6S_{5/2}$
4666.76	3.0	FeII	$3d^6 \ ^5D \ 4p \ z^4F_{9/2}^o - 3d^6 \ ^3F_2 \ 4s \ b^4F_{7/2}$
4670.18	1.2	FeII	$3d^6 \ ^5D \ 4p \ z^6F_{7/2}^o - 3d^6 \ ^3P_2 \ 4s \ b^4P_{5/2}$
4731.45	1.6	FeII	$3d^6 \ ^5D \ 4p \ z^4D_{7/2}^o - 3d^5 \ 4s^2 \ a^6S_{5/2}$
4861.32	24.0	H I	4 – 2
4871.28	1.3	FeII	$3d^6 \ ^5D \ 4p \ z^6F_{5/2}^o - 3d^6 \ ^3P_2 \ 4s \ b^4P_{3/2}$
4923.93	2.1	FeII	$3d^6 \ ^5D \ 4p \ z^6P_{3/2}^o - 3d^5 \ 4s^2 \ a^6S_{5/2}$
4993.36	2.5	FeII	$3d^6 \ ^5D \ 4p \ z^6P_{7/2}^o - 3d^6 \ ^3F_2 \ 4s \ b^4F_{9/2}$
5018.44	2.4	FeII	$3d^6 \ ^5D \ 4p \ z^6P_{5/2}^o - 3d^5 \ 4s^2 \ a^6S_{5/2}$
5041.04	1.2	S III	$3s^2 \ ^1S \ 4d \ ^2D_{3/2} - 3s^2 \ ^1S \ 4p \ ^2P_{1/2}^o$
5056.00	1.2	S III	$3s^2 \ ^1S \ 4d \ ^2D_{5/2} - 3s^2 \ ^1S \ 4p \ ^2P_{3/2}^o$
5132.67	1.0	FeII	$3d^6 \ ^5D \ 4p \ z^6F_{9/2}^o - 3d^6 \ ^3F_2 \ 4s \ b^4F_{9/2}$
5146.13	1.7	FeII	$3d^6 \ ^5D \ 4p \ z^6F_{7/2}^o - 3d^6 \ ^3F_2 \ 4s \ b^4F_{7/2}$
5154.41	1.1	FeII	$3d^6 \ ^5D \ 4p \ z^6F_{5/2}^o - 3d^6 \ ^3F_2 \ 4s \ b^4F_{5/2}$
5169.03	2.7	FeII	$3d^6 \ ^5D \ 4p \ z^6P_{7/2}^o - 3d^5 \ 4s^2 \ a^6S_{5/2}$
5188.68	1.2	TiIII	$3d^2 \ ^3F \ 4p \ z^2D_{5/2}^o - 3d^3 \ b^2D_{5/2}$
5197.58	6.7	FeII	$3d^6 \ ^5D \ 4p \ z^4F_{3/2}^o - 3d^6 \ ^3G \ 4s \ a^4G_{5/2}$
5234.62	6.9	FeII	$3d^6 \ ^5D \ 4p \ z^4F_{5/2}^o - 3d^6 \ ^3G \ 4s \ a^4G_{7/2}$
5254.93	3.3	FeII	$3d^6 \ ^5D \ 4p \ z^4F_{5/2}^o - 3d^6 \ ^3G \ 4s \ a^4G_{5/2}$
5264.81	3.5	FeII	$3d^6 \ ^5D \ 4p \ z^4D_{3/2}^o - 3d^6 \ ^3G \ 4s \ a^4G_{5/2}$
5276.00	7.1	FeII	$3d^6 \ ^5D \ 4p \ z^4F_{7/2}^o - 3d^6 \ ^3G \ 4s \ a^4G_{9/2}$
5284.11	3.1	FeII	$3d^6 \ ^5D \ 4p \ z^6F_{7/2}^o - 3d^5 \ 4s^2 \ a^6S_{5/2}$
5316.62	7.4	FeII	$3d^6 \ ^5D \ 4p \ z^4F_{9/2}^o - 3d^6 \ ^3G \ 4s \ a^4G_{11/2}$
5316.78	5.0	FeII	$3d^6 \ ^5D \ 4p \ z^4D_{5/2}^o - 3d^6 \ ^3G \ 4s \ a^4G_{7/2}$
5325.55	6.1	FeII	$3d^6 \ ^5D \ 4p \ z^4F_{7/2}^o - 3d^6 \ ^3G \ 4s \ a^4G_{7/2}$
5337.73	1.1	FeII	$3d^6 \ ^5D \ 4p \ z^4D_{5/2}^o - 3d^6 \ ^3G \ 4s \ a^4G_{5/2}$
5362.87	5.8	FeII	$3d^6 \ ^5D \ 4p \ z^4D_{7/2}^o - 3d^6 \ ^3G \ 4s \ a^4G_{9/2}$
5414.07	1.4	FeII	$3d^6 \ ^5D \ 4p \ z^4D_{7/2}^o - 3d^6 \ ^3G \ 4s \ a^4G_{7/2}$
5425.26	3.1	FeII	$3d^6 \ ^5D \ 4p \ z^4F_{9/2}^o - 3d^6 \ ^3G \ 4s \ a^4G_{9/2}$
5427.83	1.2	FeII	$3d^6 \ ^3D \ 4p \ z^4F_{9/2}^o - 3d^5 \ 4s^2 \ b^4G_{11/2}$
5432.97	1.8	FeII	$3d^6 \ ^5D \ 4p \ z^4F_{7/2}^o - 3d^6 \ ^3H \ 4s \ b^2H_{9/2}$
5534.85	5.3	FeII	$3d^6 \ ^5D \ 4p \ z^4F_{9/2}^o - 3d^6 \ ^3H \ 4s \ b^2H_{11/2}$
5991.38	3.0	FeII	$3d^6 \ ^5D \ 4p \ z^6F_{9/2}^o - 3d^6 \ ^3G \ 4s \ a^4G_{11/2}$
6084.11	1.8	FeII	$3d^6 \ ^5D \ 4p \ z^6F_{7/2}^o - 3d^6 \ ^3G \ 4s \ a^4G_{9/2}$
6147.74	4.3	FeII	$3d^6 \ ^5D \ 4p \ z^4P_{1/2}^o - 3d^6 \ ^3D \ 4s \ b^4D_{3/2}$
6149.26	4.3	FeII	$3d^6 \ ^5D \ 4p \ z^4P_{1/2}^o - 3d^6 \ ^3D \ 4s \ b^4D_{1/2}$
6238.39	4.9	FeII	$3d^6 \ ^5D \ 4p \ z^4P_{3/2}^o - 3d^6 \ ^3D \ 4s \ b^4D_{3/2}$

Table 3 – Continued

λ (Å)	W_λ (Å)	Species	Transition (upper level – lower level)
6239.95	1.3	FeII	$3d^6 \ ^5D \ 4p \ z^4P_{3/2}^o - 3d^6 \ ^3D \ 4s \ b^4D_{1/2}$
6247.56	6.4	FeII	$3d^6 \ ^5D \ 4p \ z^4P_{3/2}^o - 3d^6 \ ^3D \ 4s \ b^4D_{5/2}$
6416.92	4.5	FeII	$3d^6 \ ^5D \ 4p \ z^4P_{5/2}^o - 3d^6 \ ^3D \ 4s \ b^4D_{5/2}$
6432.68	2.6	FeII	$3d^6 \ ^5D \ 4p \ z^6D_{5/2}^o - 3d^54s^2 \ a^6S_{5/2}$
6456.38	7.6	FeII	$3d^6 \ ^5D \ 4p \ z^4P_{5/2}^o - 3d^6 \ ^3D \ 4s \ b^4D_{7/2}$
6516.08	3.7	FeII	$3d^6 \ ^5D \ 4p \ z^6D_{7/2}^o - 3d^54s^2 \ a^6S_{5/2}$
6562.79	55.6	HI	3 – 2
7222.39	2.2	FeII	$3d^6 \ ^5D \ 4p \ z^4D_{1/2}^o - 3d^6 \ ^3D \ 4s \ b^4D_{3/2}$
7224.49	2.5	FeII	$3d^6 \ ^5D \ 4p \ z^4D_{1/2}^o - 3d^6 \ ^3D \ 4s \ b^4D_{1/2}$
7289.05	1.0	FeII	$3d^6 \ ^5D \ 4p \ z^4F_{5/2}^o - 3d^6 \ ^3D \ 4s \ b^4D_{3/2}$
7308.07	3.7	FeII	$3d^6 \ ^5D \ 4p \ z^4D_{3/2}^o - 3d^6 \ ^3D \ 4s \ b^4D_{3/2}$
7310.22	2.0	FeII	$3d^6 \ ^5D \ 4p \ z^4D_{3/2}^o - 3d^6 \ ^3D \ 4s \ b^4D_{1/2}$
7320.65	2.6	FeII	$3d^6 \ ^5D \ 4p \ z^4D_{3/2}^o - 3d^6 \ ^3D \ 4s \ b^4D_{5/2}$
7449.33	2.3	FeII	$3d^6 \ ^5D \ 4p \ z^4D_{5/2}^o - 3d^6 \ ^3D \ 4s \ b^4D_{3/2}$
7462.41	5.5	FeII	$3d^6 \ ^5D \ 4p \ z^4D_{5/2}^o - 3d^6 \ ^3D \ 4s \ b^4D_{5/2}$
7479.69	1.3	FeII	$3d^6 \ ^5D \ 4p \ z^4F_{7/2}^o - 3d^6 \ ^3D \ 4s \ b^4D_{5/2}$
7515.83	1.8	FeII	$3d^6 \ ^5D \ 4p \ z^4D_{5/2}^o - 3d^6 \ ^3D \ 4s \ b^4D_{7/2}$
7655.49	1.4	FeII	$3d^6 \ ^5D \ 4p \ z^4D_{7/2}^o - 3d^6 \ ^3D \ 4s \ b^4D_{5/2}$
7711.72	6.8	FeII	$3d^6 \ ^5D \ 4p \ z^4D_{7/2}^o - 3d^6 \ ^3D \ 4s \ b^4D_{7/2}$
7771.94	-2.8	OI	$2s^22p^3 \ ^4S^o \ 3p \ ^5P_3 - 2s^22p^3 \ ^4S^o \ 3s \ ^5S^o_2$
7774.17	-2.5	OI	$2s^22p^3 \ ^4S^o \ 3p \ ^5P_2 - 2s^22p^3 \ ^4S^o \ 3s \ ^5S^o_2$
7775.39	-1.9	OI	$2s^22p^3 \ ^4S^o \ 3p \ ^5P_1 - 2s^22p^3 \ ^4S^o \ 3s \ ^5S^o_2$
7841.39	1.0	FeII	$3d^6 \ ^5D \ 4p \ z^4F_{9/2}^o - 3d^6 \ ^3D \ 4s \ b^4D_{7/2}$
7849.72	1.1	SiII	$3s^2 \ ^1S \ 5f \ ^2F_{7/2}^o - 3s^2 \ ^1S \ 4d \ ^2D_{5/2}$
7877.05	3.4	MgII	$4d \ ^2D_{3/2} - 4p \ ^2P_{1/2}^o$
7896.04	1.2	MgII	$4d \ ^2D_{3/2} - 4p \ ^2P_{3/2}^o$
7896.37	4.2	MgII	$4d \ ^2D_{5/2} - 4p \ ^2P_{3/2}^o$
8234.64	1.2	MgII	$5s \ ^2S_{1/2} - 4p \ ^2P_{3/2}^o$
8446.36	2.3	OI	$2s^22p^3 \ ^4S^o \ 3p \ ^3P_2 - 2s^22p^3 \ ^4S^o \ 3s \ ^3S^o_1$
8446.76	1.6	OI	$2s^22p^3 \ ^4S^o \ 3p \ ^3P_1 - 2s^22p^3 \ ^4S^o \ 3s \ ^3S^o_1$
8498.02	-1.2	CaII	$3p^64p \ ^2P_{3/2}^o - 3p^63d \ ^2D_{3/2}$
8542.09	-2.5	CaII	$3p^64p \ ^2P_{3/2}^o - 3p^63d \ ^2D_{5/2}$
8545.39	1.0	HI	15 – 3
8598.39	1.0	HI	14 – 3
8662.14	-2.3	CaII	$3p^64p \ ^2P_{1/2}^o - 3p^63d \ ^2D_{3/2}$
8665.02	1.2	HI	13 – 3
8750.48	1.3	HI	12 – 3
8862.79	1.7	HI	11 – 3
8912.07	1.2	CaII	$3p^64f \ ^2F_{5/2}^o - 3p^64d \ ^2D_{3/2}$
8927.36	1.8	CaII	$3p^64f \ ^2F_{7/2}^o - 3p^64d \ ^2D_{5/2}$
8981.13	1.2	FeII	$3d^6 \ ^3H \ 4pz^2H_{11/2}^o - 3d^54s^2 \ b^4G_{11/2}$
9014.91	2.1	HI	10 – 3
9218.25	4.4	MgII	$4p \ ^2P_{3/2}^o - 4s \ ^2S_{1/2}$
9229.02	3.1	HI	9 – 3
9244.26	4.2	MgII	$4p \ ^2P_{1/2}^o - 4s \ ^2S_{1/2}$
9297.27	1.5	FeII	$3d^5 \ ^4P \ 4s4p \ ^3P \ ^6D_{9/2}^o - 3d^6 \ ^5D \ 5s \ e^6D_{9/2}$
9545.97	4.7	HI	8 – 3
9550.31	1.4	FeII	$3d^6 \ ^3H \ 4pz^4G_{11/2}^o - 3d^6 \ ^3F_1 \ 4s \ c \ ^4F_{9/2}$
9631.89	3.6	MgII	$5f \ ^2F_{7/2}^o - 4d \ ^2D_{5/2}$
9632.43	2.6	MgII	$5f \ ^2F_{5/2}^o - 4d \ ^2D_{3/2}$
9956.31	1.0	FeII	$3d^54s^2 \ b^4G_{9/2} - 3d^6 \ ^5D \ 4p \ z^4F_{9/2}^o$
9997.58	8.7	FeII	$3d^54s^2 \ b^4G_{11/2} - 3d^6 \ ^5D \ 4p \ z^4F_{9/2}^o$
10049.37	8.1	HI	7 – 3
10245.54	1.3	FeII	$3d^6 \ ^3F_2 \ 4p \ y^4G_{7/2}^o - 3d^54s^2 \ b^4G_{7/2}$
10332.93	2.1	FeII	$3d^6 \ ^3F_2 \ 4p \ y^4G_{9/2}^o - 3d^54s^2 \ b^4G_{9/2}$

Table 3 – Continued

λ (Å)	W_λ (Å)	Species	Transition (upper level – lower level)
10366.17	3.0	FeII	$3d^6$ 3F_2 4p $y^4G_{11/2}^o$ – $3d^5 4s^2$ $b^4G_{11/2}$
10490.94	1.0	FeII	$3d^5 4s^2$ $b^4G_{7/2}$ – $3d^6$ 5D 4p $z^4F_{7/2}^o$
10501.50	6.4	FeII	$3d^5 4s^2$ $b^4G_{9/2}$ – $3d^6$ 5D 4p $z^4F_{7/2}^o$

Table 4: Line list for model used to match observations on 11 October 1994

λ (Å)	W_λ (Å)	Species	Transition (upper level – lower level)
3202.54	-4.0	TiIII	$3d^2 \ ^1D \ 4p \ y^2F_{5/2}^o - 3d^2 \ ^1D \ 4s \ a^2D_{3/2}$
3203.44	-2.7	TiIII	$3d^2 \ ^3F \ 4p \ z^2F_{5/2}^o - 3d^2 \ ^3F \ 4s \ a^4F_{3/2}$
3210.44	-4.8	FeII	$3d^6 \ ^5D \ 4p \ z^4D_{3/2}^o - 3d^7 \ a^4P_{1/2}$
3212.02	-2.3	FeII	$3d^6 \ ^3H \ 4p \ z4I_{9/2}^o - 3d^6 \ ^3G \ 4s \ b^2G_{9/2}$
3213.31	-6.2	FeII	$3d^6 \ ^5D \ 4p \ z^4D_{5/2}^o - 3d^7 \ a^4P_{3/2}$
3214.78	-3.2	TiIII	$3d^2 \ ^3F \ 4p \ z^2F_{7/2}^o - 3d^2 \ ^3F \ 4s \ a^4F_{9/2}$
3216.90	-1.5	TiIII	$3d^2 \ ^1D \ 4p \ y^2F_{7/2}^o - 3d^3 \ a^2G_{7/2}$
3217.06	-5.5	TiIII	$3d^2 \ ^3F \ 4p \ z^4F_{9/2}^o - 3d^2 \ ^3F \ 4s \ a^4F_{7/2}$
3218.26	-3.1	TiIII	$3d^2 \ ^1G \ 4p \ y^2G_{7/2}^o - 3d^3 \ a^2H_{9/2}$
3222.84	-5.8	TiIII	$3d^2 \ ^3F \ 4p \ z^4F_{7/2}^o - 3d^2 \ ^3F \ 4s \ a^4F_{5/2}$
3224.24	-3.2	TiIII	$3d^2 \ ^1G \ 4p \ y^2G_{9/2}^o - 3d^3 \ a^2H_{11/2}$
3226.78	-2.2	TiIII	$3d^2 \ ^3F \ 4p \ z^2F_{5/2}^o - 3d^2 \ ^3F \ 4s \ a^4F_{7/2}$
3227.74	-6.4	FeII	$3d^6 \ ^5D \ 4p \ z^4D_{7/2}^o - 3d^7 \ a^4P_{5/2}$
3228.60	-3.6	TiIII	$3d^2 \ ^1D \ 4p \ z^2P_{1/2}^o - 3d^2 \ ^1D \ 4s \ a^2D_{3/2}$
3229.20	-5.3	TiIII	$3d^2 \ ^3F \ 4p \ z^4F_{5/2}^o - 3d^2 \ ^3F \ 4s \ a^4F_{3/2}$
3229.43	-3.7	TiIII	$3d^2 \ ^1D \ 4p \ y^2F_{7/2}^o - 3d^3 \ a^2G_{9/2}$
3231.32	-3.1	TiIII	$3d^2 \ ^3F \ 4p \ z^2D_{5/2}^o - 3d^3 \ b^4F_{7/2}$
3231.71	-1.8	FeII	$3d^6 \ ^3H \ 4p \ z^2G_{7/2}^o - 3d^6 \ ^3D \ 4s \ b^4D_{5/2}$
3232.28	-3.3	TiIII	$3d^2 \ ^1D \ 4p \ y^2F_{5/2}^o - 3d^3 \ a^2G_{7/2}$
3232.78	-1.9	FeII	$3d^6 \ ^3F_2 \ 4p \ z^2F_{5/2}^o - 3d^6 \ ^1G_2 \ 4s \ c^2G_{7/2}$
3234.52	-8.4	TiIII	$3d^2 \ ^3F \ 4p \ z^4F_{9/2}^o - 3d^2 \ ^3F \ 4s \ a^4F_{9/2}$
3234.93	-1.6	FeII	$3d^6 \ ^5D \ 4p \ z^6D_{5/2}^o - 3d^6 \ ^5D \ 4s \ a^4D_{7/2}$
3236.12	-3.3	TiIII	$3d^2 \ ^1D \ 4p \ y^2D_{3/2}^o - 3d^2 \ ^1D \ 4s \ a^2D_{3/2}$
3236.58	-7.8	TiIII	$3d^2 \ ^3F \ 4p \ z^4F_{7/2}^o - 3d^2 \ ^3F \ 4s \ a^4F_{7/2}$
3237.40	-1.6	FeII	$3d^6 \ ^3F_2 \ 4p \ y^4F_{3/2}^o - 3d^6 \ ^3D \ 4s \ b^4D_{3/2}$
3237.82	-2.4	FeII	$3d^6 \ ^3F_2 \ 4p \ y^4F_{3/2}^o - 3d^6 \ ^3D \ 4s \ b^4D_{1/2}$
3239.04	-7.2	TiIII	$3d^2 \ ^3F \ 4p \ z^4F_{5/2}^o - 3d^2 \ ^3F \ 4s \ a^4F_{5/2}$
3239.66	-2.8	TiIII	$3d^2 \ ^1D \ 4p \ y^2D_{3/2}^o - 3d^2 \ ^1D \ 4s \ a^2D_{5/2}$
3241.99	-6.9	TiIII	$3d^2 \ ^3F \ 4p \ z^4F_{3/2}^o - 3d^2 \ ^3F \ 4s \ a^4F_{3/2}$
3243.72	-2.0	FeII	$3d^6 \ ^3F_2 \ 4p \ z^2F_{7/2}^o - 3d^6 \ ^1G_2 \ 4s \ c^2G_{9/2}$
3247.17	-2.6	FeII	$3d^6 \ ^3F_2 \ 4p \ y^4F_{5/2}^o - 3d^6 \ ^3D \ 4s \ b^4D_{3/2}$
3247.39	-1.0	FeII	$3d^6 \ ^3F_2 \ 4p \ z^2F_{7/2}^o - 3d^6 \ ^1G_2 \ 4s \ c^2G_{7/2}$
3248.60	-4.8	TiIII	$3d^2 \ ^3P \ 4p \ y^4D_{7/2}^o - 3d^2 \ ^3P \ 4s \ b^4P_{5/2}$
3248.70	-2.5	TiIII	$3d^2 \ ^3F \ 4p \ z^2D_{3/2}^o - 3d^3 \ b^4F_{5/2}$
3249.37	-2.8	TiIII	$3d^2 \ ^1D \ 4p \ y^2D_{5/2}^o - 3d^2 \ ^1D \ 4s \ a^2D_{3/2}$
3249.66	-1.4	FeII	$3d^6 \ ^3F_2 \ 4p \ y^4F_{5/2}^o - 3d^6 \ ^3D \ 4s \ b^4D_{5/2}$
3249.92	-1.4	FeII	$3d^6 \ ^3P_2 \ 4p \ z^2D_{3/2}^o - 3d^6 \ ^3D \ 4s \ b^4D_{3/2}$
3250.34	-1.0	FeII	$3d^6 \ ^3P_2 \ 4p \ z^2D_{3/2}^o - 3d^6 \ ^3D \ 4s \ b^4D_{1/2}$
3251.92	-5.2	TiIII	$3d^2 \ ^3F \ 4p \ z^4F_{3/2}^o - 3d^2 \ ^3F \ 4s \ a^4F_{5/2}$
3252.92	-5.6	TiIII	$3d^2 \ ^3F \ 4p \ z^4F_{5/2}^o - 3d^2 \ ^3F \ 4s \ a^4F_{7/2}$
3252.94	-3.3	TiIII	$3d^2 \ ^1D \ 4p \ y^2D_{5/2}^o - 3d^2 \ ^1D \ 4s \ a^2D_{5/2}$
3254.25	-5.2	TiIII	$3d^2 \ ^3F \ 4p \ z^4F_{7/2}^o - 3d^2 \ ^3F \ 4s \ a^4F_{9/2}$
3255.89	-4.7	FeII	$3d^6 \ ^5D \ 4p \ z^6D_{7/2}^o - 3d^6 \ ^5D \ 4s \ a^4D_{7/2}$
3258.03	-1.3	FeII	$3d^5 \ ^6S \ 4s4p \ ^3P \ y^6P_{5/2}^o - 3d^6 \ ^3D \ 4s \ b^4D_{3/2}$
3258.77	-2.6	FeII	$3d^6 \ ^3F_2 \ 4p \ y^4F_{7/2}^o - 3d^6 \ ^3D \ 4s \ b^4D_{5/2}$
3259.05	-2.8	FeII	$3d^6 \ ^3F_2 \ 4p \ y^4F_{9/2}^o - 3d^6 \ ^3D \ 4s \ b^4D_{7/2}$
3260.27	-2.0	TiIII	$3d^2 \ ^3P \ 4p \ z^4S_{3/2}^o - 3d^3 \ a^4P_{1/2}$
3261.59	-3.9	TiIII	$3d^2 \ ^1G \ 4p \ z^2H_{11/2}^o - 3d^2 \ ^1G \ 4s \ b^2G_{9/2}$
3261.62	-4.2	TiIII	$3d^2 \ ^3P \ 4p \ y^4D_{5/2}^o - 3d^2 \ ^3P \ 4s \ b^4P_{3/2}$
3263.68	-2.4	TiIII	$3d^2 \ ^3P \ 4p \ z^4S_{3/2}^o - 3d^3 \ a^4P_{3/2}$
3264.76	-2.1	FeII	$3d^6 \ ^5D \ 4p \ z^6D_{3/2}^o - 3d^6 \ ^5D \ 4s \ a^4D_{5/2}$
3266.44	-1.3	TiIII	$3d^2 \ ^3P \ 4p \ y^4D_{5/2}^o - 3d^3 \ a^2P_{3/2}$
3266.94	-1.3	FeII	$3d^6 \ ^3H \ 4p \ z^4H_{9/2}^o - 3d^6 \ ^3G \ 4s \ b^2G_{9/2}$

Table 4 – Continued

λ (Å)	W_λ (Å)	Species	Transition (upper level – lower level)
3269.74	-1.4	TiII	$3d^2 \ ^3P \ 4p \ y^4D_{3/2}^o - 3d^3 \ a^2P_{1/2}$
3271.66	-3.5	TiII	$3d^2 \ ^3P \ 4p \ y^4D_{5/2}^o - 3d^2 \ ^3P \ 4s \ b^4P_{5/2}$
3272.07	-3.3	TiII	$3d^2 \ ^3P \ 4p \ y^4D_{3/2}^o - 3d^2 \ ^3P \ 4s \ b^4P_{1/2}$
3276.60	-1.5	FeII	$3d^6 \ ^3H \ 4p \ z^2G_{7/2}^o - 3d^7 \ b^2F_{5/2}$
3276.77	-2.7	TiII	$3d^2 \ ^3P \ 4p \ z^4S_{3/2}^o - 3d^3 \ a^4P_{5/2}$
3277.35	-4.7	FeII	$3d^6 \ ^5D \ 4p \ z^6D_{9/2}^o - 3d^6 \ ^5D \ 4s \ a^4D_{7/2}$
3278.29	-3.6	TiII	$3d^2 \ ^3P \ 4p \ y^4D_{3/2}^o - 3d^2 \ ^3P \ 4s \ b^4P_{3/2}$
3278.92	-3.9	TiII	$3d^2 \ ^1D \ 4p \ z^2P_{3/2}^o - 3d^2 \ ^1D \ 4s \ a^2D_{5/2}$
3279.97	-1.2	TiII	$3d^2 \ ^3P \ 4p \ y^4D_{1/2}^o - 3d^3 \ a^2P_{1/2}$
3279.99	-2.6	TiII	$3d^2 \ ^1D \ 4p \ y^2D_{5/2}^o - 3d^3 \ a^2G_{7/2}$
3281.29	-4.1	FeII	$3d^6 \ ^5D \ 4p \ z^6D_{5/2}^o - 3d^6 \ ^5D \ 4s \ a^4D_{5/2}$
3282.33	-3.3	TiII	$3d^2 \ ^3P \ 4p \ y^4D_{1/2}^o - 3d^2 \ ^3P \ 4s \ b^4P_{1/2}$
3283.16	-1.0	TiII	$3d^2 \ ^3P \ 4p \ y^4D_{3/2}^o - 3d^3 \ a^2P_{3/2}$
3285.41	-2.1	FeII	$3d^6 \ ^5D \ 4p \ z^6D_{1/2}^o - 3d^6 \ ^5D \ 4s \ a^4D_{3/2}$
3287.66	-3.7	TiII	$3d^2 \ ^1G \ 4p \ z^2H_{9/2}^o - 3d^2 \ ^1G \ 4s \ b^2G_{7/2}$
3288.15	-1.6	TiII	$3d^2 \ ^3F \ 4p \ z^2F_{7/2}^o - 3d^3 \ b^4F_{7/2}$
3288.43	-1.8	TiII	$3d^2 \ ^3P \ 4p \ y^4D_{3/2}^o - 3d^2 \ ^3P \ 4s \ b^4P_{5/2}$
3288.58	-2.1	TiII	$3d^2 \ ^3P \ 4p \ y^4D_{1/2}^o - 3d^2 \ ^3P \ 4s \ b^4P_{3/2}$
3289.35	-1.9	FeII	$3d^6 \ ^3H \ 4p \ z^4H_{7/2}^o - 3d^6 \ ^3G \ 4s \ b^2G_{7/2}$
3295.23	-1.2	FeII	$3d^6 \ ^3P_2 \ 4p \ y^4D_{7/2}^o - 3d^6 \ ^3D \ 4s \ b^4D_{5/2}$
3295.82	-3.6	FeII	$3d^6 \ ^5D \ 4p \ z^6D_{3/2}^o - 3d^6 \ ^5D \ 4s \ a^4D_{3/2}$
3297.88	-1.2	FeII	$3d^6 \ ^3P_2 \ 4p \ z^2D_{3/2}^o - 3d^7 \ b^2F_{5/2}$
3302.11	-1.7	TiII	$3d^2 \ ^3F \ 4p \ z^2F_{7/2}^o - 3d^3 \ b^4F_{9/2}$
3302.86	-2.6	FeII	$3d^6 \ ^5D \ 4p \ z^6D_{7/2}^o - 3d^6 \ ^5D \ 4s \ a^4D_{5/2}$
3303.46	-3.9	FeII	$3d^6 \ ^5D \ 4p \ z^6D_{1/2}^o - 3d^6 \ ^5D \ 4s \ a^4D_{1/2}$
3308.81	-3.6	TiII	$3d^2 \ ^3F \ 4p \ z^4F_{9/2}^o - 3d^3 \ b^4F_{7/2}$
3312.92	-1.4	TiII	$3d^2 \ ^3P \ 4p \ z^4S_{3/2}^o - 3d^3 \ a^2P_{1/2}$
3313.99	-1.9	FeII	$3d^6 \ ^5D \ 4p \ z^6D_{3/2}^o - 3d^6 \ ^5D \ 4s \ a^4D_{1/2}$
3315.31	-2.6	TiII	$3d^2 \ ^3P \ 4p \ z^4S_{3/2}^o - 3d^2 \ ^3P \ 4s \ b^4P_{1/2}$
3318.02	-3.9	TiII	$3d^2 \ ^3F \ 4p \ z^4F_{7/2}^o - 3d^3 \ b^4F_{5/2}$
3321.70	-3.4	TiII	$3d^2 \ ^3P \ 4p \ z^4S_{3/2}^o - 3d^2 \ ^3P \ 4s \ b^4P_{3/2}$
3322.94	-6.4	TiII	$3d^2 \ ^3F \ 4p \ z^4F_{9/2}^o - 3d^3 \ b^4F_{9/2}$
3323.06	-1.7	FeII	$3d^6 \ ^3H \ 4p \ z^2G_{9/2}^o - 3d^7 \ b^2F_{7/2}$
3326.78	-3.7	TiII	$3d^2 \ ^3F \ 4p \ z^4F_{5/2}^o - 3d^3 \ b^4F_{3/2}$
3326.85	-1.1	TiII	$3d^2 \ ^1D \ 4p \ y^2F_{7/2}^o - 3d^2 \ ^3P \ 4s \ b^4P_{5/2}$
3329.11	-1.0	FeII	$3d^6 \ ^3H \ 4p \ z4I_{9/2}^o - 3d^6 \ ^3D \ 4s \ b^4D_{7/2}$
3329.45	-6.0	TiII	$3d^2 \ ^3F \ 4p \ z^4F_{7/2}^o - 3d^3 \ b^4F_{7/2}$
3332.11	-3.7	TiII	$3d^2 \ ^3P \ 4p \ z^4S_{3/2}^o - 3d^2 \ ^3P \ 4s \ b^4P_{5/2}$
3335.20	-5.5	TiII	$3d^2 \ ^3F \ 4p \ z^4F_{5/2}^o - 3d^3 \ b^4F_{5/2}$
3337.86	-1.8	TiII	$3d^2 \ ^1D \ 4p \ y^2F_{5/2}^o - 3d^3 \ a^2P_{3/2}$
3338.52	-1.1	FeII	$3d^6 \ ^3P_2 \ 4p \ y^4P_{3/2}^o - 3d^6 \ ^3D \ 4s \ b^4D_{5/2}$
3340.36	-5.2	TiII	$3d^2 \ ^3F \ 4p \ z^4F_{3/2}^o - 3d^3 \ b^4F_{3/2}$
3341.88	-5.2	TiII	$3d^2 \ ^3F \ 4p \ z^2G_{7/2}^o - 3d^2 \ ^3F \ 4s \ a^2F_{5/2}$
3343.77	-3.5	TiII	$3d^2 \ ^3F \ 4p \ z^4F_{7/2}^o - 3d^3 \ b^4F_{9/2}$
3346.75	-3.8	TiII	$3d^2 \ ^3F \ 4p \ z^4F_{5/2}^o - 3d^3 \ b^4F_{7/2}$
3348.85	-3.5	TiII	$3d^2 \ ^3F \ 4p \ z^4F_{3/2}^o - 3d^3 \ b^4F_{5/2}$
3349.04	-5.4	TiII	$3d^2 \ ^3F \ 4p \ z^2G_{9/2}^o - 3d^2 \ ^3F \ 4s \ a^2F_{7/2}$
3349.41	-7.1	TiII	$3d^2 \ ^3F \ 4p \ z^4G_{11/2}^o - 3d^2 \ ^3F \ 4s \ a^4F_{9/2}$
3350.42	-1.0	NiII	$3d^8 \ ^3F \ 4p \ ^4D_{3/2}^o - 3d^8 \ ^1D \ 4s \ ^2D_{3/2}$
3352.07	-1.5	TiII	$3d^2 \ ^1D \ 4p \ z^2P_{1/2}^o - 3d^3 \ a^2P_{1/2}$
3361.22	-6.7	TiII	$3d^2 \ ^3F \ 4p \ z^4G_{9/2}^o - 3d^2 \ ^3F \ 4s \ a^4F_{7/2}$
3366.18	-1.8	TiII	$3d^2 \ ^1D \ 4p \ z^2P_{1/2}^o - 3d^3 \ a^2P_{3/2}$
3372.21	-2.5	TiII	$3d^2 \ ^3F \ 4p \ z^2G_{7/2}^o - 3d^2 \ ^3F \ 4s \ a^2F_{7/2}$
3372.80	-6.4	TiII	$3d^2 \ ^3F \ 4p \ z^4G_{7/2}^o - 3d^2 \ ^3F \ 4s \ a^4F_{5/2}$

Table 4 – Continued

λ (Å)	W_λ (Å)	Species	Transition (upper level – lower level)
3373.97	-1.5	NiII	$3d^8 \ 3F \ 4p \ 4D_{5/2}^o - 3d^8 \ 3P \ 4s \ 4P_{5/2}$
3374.35	-1.5	TiII	$3d^2 \ 1D \ 4p \ y^2D_{3/2}^o - 3d^3 \ a^2P_{3/2}$
3380.28	-4.3	TiII	$3d^2 \ 3F \ 4p \ z^4G_{9/2}^o - 3d^2 \ 3F \ 4s \ a^4F_{9/2}$
3381.36	-1.5	FeII	$3d^6 \ 5D \ 4p \ z^6P_{5/2}^o - 3d^7 \ a^4P_{3/2}$
3383.77	-6.0	TiII	$3d^2 \ 3F \ 4p \ z^4G_{5/2}^o - 3d^2 \ 3F \ 4s \ a^4F_{3/2}$
3387.85	-4.5	TiII	$3d^2 \ 3F \ 4p \ z^4G_{7/2}^o - 3d^2 \ 3F \ 4s \ a^4F_{7/2}$
3388.76	-1.6	TiII	$3d^2 \ 1D \ 4p \ y^2D_{5/2}^o - 3d^3 \ a^2P_{3/2}$
3394.58	-4.2	TiII	$3d^2 \ 3F \ 4p \ z^4G_{5/2}^o - 3d^2 \ 3F \ 4s \ a^4F_{5/2}$
3402.42	-1.6	TiII	$3d^2 \ 1D \ 4p \ z^2P_{3/2}^o - 3d^3 \ a^2P_{1/2}$
3407.21	-1.8	TiII	$3d^2 \ 3F \ 4p \ z^4G_{7/2}^o - 3d^2 \ 3F \ 4s \ a^4F_{9/2}$
3407.30	-1.5	NiII	$3d^8 \ 3F \ 4p \ 4D_{1/2}^o - 3d^8 \ 3P \ 4s \ 4P_{1/2}$
3409.82	-2.0	TiII	$3d^2 \ 3F \ 4p \ z^4G_{5/2}^o - 3d^2 \ 3F \ 4s \ a^4F_{7/2}$
3416.02	-2.1	FeII	$3d^6 \ 5D \ 4p \ z^4P_{1/2}^o - 3d^7 \ a^2P_{3/2}$
3416.96	-1.6	TiII	$3d^2 \ 1D \ 4p \ z^2P_{3/2}^o - 3d^3 \ a^2P_{3/2}$
3425.57	-1.4	FeII	$3d^6 \ 5D \ 4p \ z^6P_{7/2}^o - 3d^7 \ a^4P_{5/2}$
3443.83	-1.6	FeII	$3d^6 \ 5D \ 4p \ z^4P_{3/2}^o - 3d^7 \ a^2P_{3/2}$
3444.31	-3.8	TiII	$3d^2 \ 3F \ 4p \ z^4G_{11/2}^o - 3d^3 \ b^4F_{9/2}$
3452.48	-1.7	TiII	$3d^2 \ 3P \ 4p \ y^2P_{1/2}^o - 3d^2 \ 3P \ 4s \ b^2P_{1/2}$
3454.16	-1.2	NiII	$3d^8 \ 3F \ 4p \ 4D_{5/2}^o - 3d^8 \ 1D \ 4s \ 2D_{3/2}$
3456.39	-2.2	TiII	$3d^2 \ 3P \ 4p \ y^2P_{3/2}^o - 3d^2 \ 3P \ 4s \ b^2P_{3/2}$
3456.92	-1.1	FeII	$3d^6 \ 3P_2 \ 4p \ y^4P_{5/2}^o - 3d^6 \ 3D \ 4s \ b^4D_{7/2}$
3461.49	-3.6	TiII	$3d^2 \ 3F \ 4p \ z^4G_{9/2}^o - 3d^3 \ b^4F_{7/2}$
3465.55	-1.3	TiII	$3d^2 \ 3P \ 4p \ y^2P_{1/2}^o - 3d^2 \ 3P \ 4s \ b^2P_{3/2}$
3465.64	-1.4	NiII	$3d^8 \ 3F \ 4p \ 4D_{3/2}^o - 3d^8 \ 3P \ 4s \ 4P_{3/2}$
3468.68	-1.4	FeII	$3d^6 \ 3H \ 4p \ z^2G_{7/2}^o - 3d^6 \ 1G_2 \ 4s \ c^2G_{7/2}$
3471.39	-1.4	NiII	$3d^8 \ 3F \ 4p \ 4D_{3/2}^o - 3d^8 \ 3P \ 4s \ 4P_{1/2}$
3475.74	-1.4	FeII	$3d^6 \ 5D \ 4p \ z^6F_{7/2}^o - 3d^7 \ a^4P_{5/2}$
3476.97	-1.2	TiII	$3d^2 \ 3F \ 4p \ z^4G_{9/2}^o - 3d^3 \ b^4F_{9/2}$
3477.19	-3.4	TiII	$3d^2 \ 3F \ 4p \ z^4G_{7/2}^o - 3d^3 \ b^4F_{5/2}$
3479.91	-1.6	FeII	$3d^6 \ 5D \ 4p \ z^6F_{3/2}^o - 3d^7 \ a^4P_{3/2}$
3480.88	-1.1	TiII	$3d^2 \ 3P \ 4p \ z^2S_{1/2}^o - 3d^2 \ 1D \ 4s \ a^2D_{3/2}$
3487.99	-1.2	FeII	$3d^6 \ 5D \ 4p \ z^6F_{5/2}^o - 3d^7 \ a^4P_{3/2}$
3489.74	-1.6	TiII	$3d^2 \ 3F \ 4p \ z^4G_{7/2}^o - 3d^3 \ b^4F_{7/2}$
3491.07	-3.1	TiII	$3d^2 \ 3F \ 4p \ z^4G_{5/2}^o - 3d^3 \ b^4F_{3/2}$
3493.47	-1.8	FeII	$3d^6 \ 3H \ 4p \ z^2G_{9/2}^o - 3d^6 \ 1G_2 \ 4s \ c^2G_{9/2}$
3494.67	-1.8	FeII	$3d^6 \ 5D \ 4p \ z^4P_{5/2}^o - 3d^7 \ a^2P_{3/2}$
3500.34	-1.6	TiII	$3d^2 \ 3F \ 4p \ z^4G_{5/2}^o - 3d^3 \ b^4F_{5/2}$
3503.47	-1.2	FeII	$3d^6 \ 5D \ 4p \ z^6F_{1/2}^o - 3d^7 \ a^4P_{1/2}$
3504.90	-3.3	TiII	$3d^2 \ 1G \ 4p \ y^2G_{9/2}^o - 3d^2 \ 1G \ 4s \ b^2G_{9/2}$
3507.40	-1.4	FeII	$3d^6 \ 5D \ 4p \ z^4P_{3/2}^o - 3d^7 \ a^2P_{1/2}$
3509.84	-1.1	TiII	$3d^2 \ 1G \ 4p \ y^2G_{7/2}^o - 3d^2 \ 1G \ 4s \ b^2G_{9/2}$
3510.84	-3.2	TiII	$3d^2 \ 1G \ 4p \ y^2G_{7/2}^o - 3d^2 \ 1G \ 4s \ b^2G_{7/2}$
3513.99	-2.0	NiII	$3d^8 \ 3F \ 4p \ 4D_{7/2}^o - 3d^8 \ 3P \ 4s \ 4P_{5/2}$
3520.26	-2.1	TiII	$3d^2 \ 3P \ 4p \ x^2D_{3/2}^o - 3d^2 \ 3P \ 4s \ b^2P_{1/2}$
3535.41	-2.2	TiII	$3d^2 \ 3P \ 4p \ x^2D_{5/2}^o - 3d^2 \ 3P \ 4s \ b^2P_{3/2}$
3561.58	-1.3	TiII	$3d^2 \ 3F \ 4p \ z^4D_{5/2}^o - 3d^2 \ 3F \ 4s \ a^2F_{5/2}$
3564.53	-1.0	FeII	$3d^6 \ 3H \ 4p \ z^4I_{9/2}^o - 3d^6 \ 1G_2 \ 4s \ c^2G_{9/2}$
3565.97	-1.3	TiII	$3d^2 \ 3P \ 4p \ z^2S_{1/2}^o - 3d^3 \ a^4P_{3/2}$
3573.73	-2.0	TiII	$3d^2 \ 3F \ 4p \ z^4D_{3/2}^o - 3d^2 \ 3F \ 4s \ a^2F_{5/2}$
3576.76	-1.5	NiII	$3d^8 \ 3F \ 4p \ 4D_{5/2}^o - 3d^8 \ 3P \ 4s \ 4P_{3/2}$
3587.14	-1.9	TiII	$3d^2 \ 3F \ 4p \ z^4D_{7/2}^o - 3d^2 \ 3F \ 4s \ a^2F_{7/2}$
3596.05	-2.6	TiII	$3d^2 \ 3F \ 4p \ z^4D_{5/2}^o - 3d^2 \ 3F \ 4s \ a^2F_{7/2}$
3624.82	-2.3	TiII	$3d^2 \ 3P \ 4p \ z^2S_{1/2}^o - 3d^3 \ a^2P_{1/2}$
3635.34	-1.0	TiII	$3d^2 \ 3P \ 4p \ z^2S_{1/2}^o - 3d^2 \ 3P \ 4s \ b^4P_{3/2}$

Table 4 – Continued

λ (Å)	W_λ (Å)	Species	Transition (upper level – lower level)
3641.33	-2.6	TiIII	$3d^2 \ ^3P \ 4p \ z^2S_{1/2}^o - 3d^3 \ a^2P_{3/2}$
3659.76	-3.0	TiIII	$3d^2 \ ^1D \ 4p \ y^2F_{7/2}^o - 3d^3 \ b^2D_{5/2}$
3662.24	-2.8	TiIII	$3d^2 \ ^1D \ 4p \ y^2F_{5/2}^o - 3d^3 \ b^2D_{3/2}$
3679.68	-2.0	TiIII	$3d^2 \ ^1D \ 4p \ y^2F_{5/2}^o - 3d^3 \ b^2D_{5/2}$
3685.19	-4.6	TiIII	$3d^2 \ ^3F \ 4p \ z^2D_{3/2}^o - 3d^2 \ ^3F \ 4s \ a^2F_{5/2}$
3685.20	-4.9	TiIII	$3d^2 \ ^3F \ 4p \ z^2D_{5/2}^o - 3d^2 \ ^3F \ 4s \ a^2F_{7/2}$
3706.22	-2.4	TiIII	$3d^2 \ ^1D \ 4p \ y^2D_{3/2}^o - 3d^3 \ b^2D_{3/2}$
3721.64	-2.6	TiIII	$3d^2 \ ^3F \ 4p \ z^2F_{7/2}^o - 3d^2 \ ^3F \ 4s \ a^2F_{5/2}$
3741.63	-2.5	TiIII	$3d^2 \ ^1D \ 4p \ y^2D_{5/2}^o - 3d^3 \ b^2D_{5/2}$
3748.01	-1.2	TiIII	$3d^2 \ ^1G \ 4p \ x^2F_{5/2}^o - 3d^3 \ b^2F_{5/2}$
3757.69	-1.7	TiIII	$3d^2 \ ^1D \ 4p \ z^2P_{3/2}^o - 3d^3 \ b^2D_{3/2}$
3759.30	-4.7	TiIII	$3d^2 \ ^3F \ 4p \ z^2F_{7/2}^o - 3d^2 \ ^3F \ 4s \ a^2F_{7/2}$
3761.32	-4.5	TiIII	$3d^2 \ ^3F \ 4p \ z^2F_{5/2}^o - 3d^2 \ ^3F \ 4s \ a^2F_{5/2}$
3761.88	-1.4	TiIII	$3d^2 \ ^1G \ 4p \ x^2F_{7/2}^o - 3d^3 \ b^2F_{7/2}$
3764.10	-1.0	FeII	$3d^6 \ ^5D \ 4p \ z^4P_{3/2}^o - 3d^6 \ ^3P_2 \ 4s \ b^4P_{5/2}$
3783.35	-1.0	FeII	$3d^6 \ ^5D \ 4p \ z^4D_{5/2}^o - 3d^7 \ a^2P_{3/2}$
3814.58	-1.5	TiIII	$3d^2 \ ^3F \ 4p \ z^4F_{3/2}^o - 3d^2 \ ^3F \ 4s \ a^2F_{5/2}$
3836.09	-1.0	TiIII	$3d^2 \ ^3F \ 4p \ z^4F_{3/2}^o - 3d^2 \ ^3F \ 4s \ a^2F_{7/2}$
3900.55	-2.2	TiIII	$3d^2 \ ^3F \ 4p \ z^2G_{9/2}^o - 3d^3 \ a^2G_{9/2}$
3913.47	-2.0	TiIII	$3d^2 \ ^3F \ 4p \ z^2G_{7/2}^o - 3d^3 \ a^2G_{7/2}$
3933.66	-1.7	CaII	$3p^6 4p \ ^2P_{3/2}^o - 3p^6 4s \ ^2S_{1/2}$
3968.47	-1.2	CaII	$3p^6 4p \ ^2P_{1/2}^o - 3p^6 4s \ ^2S_{1/2}$
4101.73	1.2	HI	6 – 2
4163.65	-1.3	TiIII	$3d^2 \ ^3P \ 4p \ x^2D_{5/2}^o - 3d^3 \ b^2F_{7/2}$
4171.91	-1.1	TiIII	$3d^2 \ ^3P \ 4p \ x^2D_{3/2}^o - 3d^3 \ b^2F_{5/2}$
4340.46	3.5	HI	5 – 2
4576.34	1.0	FeII	$3d^6 \ ^5D \ 4p \ z^4D_{5/2}^o - 3d^6 \ ^3F_2 \ 4s \ b^4F_{5/2}$
4582.84	1.0	FeII	$3d^6 \ ^5D \ 4p \ z^4F_{7/2}^o - 3d^6 \ ^3F_2 \ 4s \ b^4F_{5/2}$
4620.52	1.0	FeII	$3d^6 \ ^5D \ 4p \ z^4D_{7/2}^o - 3d^6 \ ^3F_2 \ 4s \ b^4F_{7/2}$
4629.34	1.0	FeII	$3d^6 \ ^5D \ 4p \ z^4F_{9/2}^o - 3d^6 \ ^3F_2 \ 4s \ b^4F_{9/2}$
4666.76	1.1	FeII	$3d^6 \ ^5D \ 4p \ z^4F_{9/2}^o - 3d^6 \ ^3F_2 \ 4s \ b^4F_{7/2}$
4861.32	8.5	HI	4 – 2
4993.36	1.3	FeII	$3d^6 \ ^5D \ 4p \ z^6P_{7/2}^o - 3d^6 \ ^3F_2 \ 4s \ b^4F_{9/2}$
5146.13	1.1	FeII	$3d^6 \ ^5D \ 4p \ z^6F_{7/2}^o - 3d^6 \ ^3F_2 \ 4s \ b^4F_{7/2}$
5188.68	1.3	TiIII	$3d^2 \ ^3F \ 4p \ z^2D_{5/2}^o - 3d^3 \ b^2D_{5/2}$
5197.58	2.4	FeII	$3d^6 \ ^5D \ 4p \ z^4F_{3/2}^o - 3d^6 \ ^3G \ 4s \ a^4G_{5/2}$
5226.54	1.3	TiIII	$3d^2 \ ^3F \ 4p \ z^2D_{3/2}^o - 3d^3 \ b^2D_{3/2}$
5234.62	2.5	FeII	$3d^6 \ ^5D \ 4p \ z^4F_{5/2}^o - 3d^6 \ ^3G \ 4s \ a^4G_{7/2}$
5254.93	1.7	FeII	$3d^6 \ ^5D \ 4p \ z^4F_{5/2}^o - 3d^6 \ ^3G \ 4s \ a^4G_{5/2}$
5264.81	1.8	FeII	$3d^6 \ ^5D \ 4p \ z^4D_{3/2}^o - 3d^6 \ ^3G \ 4s \ a^4G_{5/2}$
5276.00	2.6	FeII	$3d^6 \ ^5D \ 4p \ z^4F_{7/2}^o - 3d^6 \ ^3G \ 4s \ a^4G_{9/2}$
5284.11	1.3	FeII	$3d^6 \ ^5D \ 4p \ z^6F_{7/2}^o - 3d^5 4s^2 \ a^6S_{5/2}$
5316.62	2.7	FeII	$3d^6 \ ^5D \ 4p \ z^4F_{9/2}^o - 3d^6 \ ^3G \ 4s \ a^4G_{11/2}$
5316.78	2.2	FeII	$3d^6 \ ^5D \ 4p \ z^4D_{5/2}^o - 3d^6 \ ^3G \ 4s \ a^4G_{7/2}$
5325.55	2.5	FeII	$3d^6 \ ^5D \ 4p \ z^4F_{7/2}^o - 3d^6 \ ^3G \ 4s \ a^4G_{7/2}$
5336.77	1.0	TiIII	$3d^2 \ ^3F \ 4p \ z^2F_{7/2}^o - 3d^3 \ b^2D_{5/2}$
5362.87	2.5	FeII	$3d^6 \ ^5D \ 4p \ z^4D_{7/2}^o - 3d^6 \ ^3G \ 4s \ a^4G_{9/2}$
5425.26	1.7	FeII	$3d^6 \ ^5D \ 4p \ z^4F_{9/2}^o - 3d^6 \ ^3G \ 4s \ a^4G_{9/2}$
5432.97	1.2	FeII	$3d^6 \ ^5D \ 4p \ z^4F_{7/2}^o - 3d^6 \ ^3H \ 4s \ b^2H_{9/2}$
5534.85	2.6	FeII	$3d^6 \ ^5D \ 4p \ z^4F_{9/2}^o - 3d^6 \ ^3H \ 4s \ b^2H_{11/2}$
5889.95	-1.0	NaI	$3p \ ^2P_{3/2}^o - 3s \ ^2S_{1/2}$
5991.38	1.9	FeII	$3d^6 \ ^5D \ 4p \ z^6F_{9/2}^o - 3d^6 \ ^3G \ 4s \ a^4G_{11/2}$
6084.11	1.3	FeII	$3d^6 \ ^5D \ 4p \ z^6F_{7/2}^o - 3d^6 \ ^3G \ 4s \ a^4G_{9/2}$
6147.74	2.3	FeII	$3d^6 \ ^5D \ 4p \ z^4P_{1/2}^o - 3d^6 \ ^3D \ 4s \ b^4D_{3/2}$

Table 4 – Continued

λ (Å)	W_λ (Å)	Species	Transition (upper level – lower level)
6149.26	2.3	FeII	$3d^6 \ 5D \ 4p \ z^4P_{1/2}^o - 3d^6 \ 3D \ 4s \ b^4D_{1/2}$
6238.39	2.6	FeII	$3d^6 \ 5D \ 4p \ z^4P_{3/2}^o - 3d^6 \ 3D \ 4s \ b^4D_{3/2}$
6247.56	3.1	FeII	$3d^6 \ 5D \ 4p \ z^4P_{3/2}^o - 3d^6 \ 3D \ 4s \ b^4D_{5/2}$
6347.11	-1.1	SiII	$3s^2 \ 1S \ 4p \ z^2P_{3/2}^o - 3s^2 \ 1S \ 4s \ 2S_{1/2}$
6416.92	2.5	FeII	$3d^6 \ 5D \ 4p \ z^4P_{5/2}^o - 3d^6 \ 3D \ 4s \ b^4D_{5/2}$
6432.68	1.8	FeII	$3d^6 \ 5D \ 4p \ z^6D_{5/2}^o - 3d^5 \ 4s^2 \ a^6S_{5/2}$
6456.38	3.8	FeII	$3d^6 \ 5D \ 4p \ z^4P_{5/2}^o - 3d^6 \ 3D \ 4s \ b^4D_{7/2}$
6516.08	2.3	FeII	$3d^6 \ 5D \ 4p \ z^6D_{7/2}^o - 3d^5 \ 4s^2 \ a^6S_{5/2}$
6562.79	26.1	HI	3 – 2
7222.39	1.6	FeII	$3d^6 \ 5D \ 4p \ z^4D_{1/2}^o - 3d^6 \ 3D \ 4s \ b^4D_{3/2}$
7224.49	1.8	FeII	$3d^6 \ 5D \ 4p \ z^4D_{1/2}^o - 3d^6 \ 3D \ 4s \ b^4D_{1/2}$
7308.07	2.5	FeII	$3d^6 \ 5D \ 4p \ z^4D_{3/2}^o - 3d^6 \ 3D \ 4s \ b^4D_{3/2}$
7310.22	1.5	FeII	$3d^6 \ 5D \ 4p \ z^4D_{3/2}^o - 3d^6 \ 3D \ 4s \ b^4D_{1/2}$
7320.65	1.9	FeII	$3d^6 \ 5D \ 4p \ z^4D_{3/2}^o - 3d^6 \ 3D \ 4s \ b^4D_{5/2}$
7449.33	1.7	FeII	$3d^6 \ 5D \ 4p \ z^4D_{5/2}^o - 3d^6 \ 3D \ 4s \ b^4D_{3/2}$
7462.41	3.4	FeII	$3d^6 \ 5D \ 4p \ z^4D_{5/2}^o - 3d^6 \ 3D \ 4s \ b^4D_{5/2}$
7479.69	1.0	FeII	$3d^6 \ 5D \ 4p \ z^4F_{7/2}^o - 3d^6 \ 3D \ 4s \ b^4D_{5/2}$
7515.83	1.3	FeII	$3d^6 \ 5D \ 4p \ z^4D_{5/2}^o - 3d^6 \ 3D \ 4s \ b^4D_{7/2}$
7655.49	1.1	FeII	$3d^6 \ 5D \ 4p \ z^4D_{7/2}^o - 3d^6 \ 3D \ 4s \ b^4D_{5/2}$
7711.72	4.2	FeII	$3d^6 \ 5D \ 4p \ z^4D_{7/2}^o - 3d^6 \ 3D \ 4s \ b^4D_{7/2}$
7771.94	-2.4	OI	$2s^2 2p^3 \ 4S^o \ 3p \ 5P_3 - 2s^2 2p^3 \ 4S^o \ 3s \ 5S_2^o$
7774.17	-2.2	OI	$2s^2 2p^3 \ 4S^o \ 3p \ 5P_2 - 2s^2 2p^3 \ 4S^o \ 3s \ 5S_2^o$
7775.39	-1.8	OI	$2s^2 2p^3 \ 4S^o \ 3p \ 5P_1 - 2s^2 2p^3 \ 4S^o \ 3s \ 5S_2^o$
7896.37	1.1	MgII	$4d \ 2D_{5/2} - 4p \ 2P_{3/2}^o$
8498.02	-3.0	CaII	$3p^6 4p \ 2P_{3/2}^o - 3p^6 3d \ 2D_{3/2}$
8542.09	-4.0	CaII	$3p^6 4p \ 2P_{3/2}^o - 3p^6 3d \ 2D_{5/2}$
8662.14	-3.8	CaII	$3p^6 4p \ 2P_{1/2}^o - 3p^6 3d \ 2D_{3/2}$
9545.97	1.5	HI	8 – 3
9631.89	1.7	MgII	$5f \ 2F_{7/2}^o - 4d \ 2D_{5/2}$
9632.43	1.4	MgII	$5f \ 2F_{5/2}^o - 4d \ 2D_{3/2}$
9997.58	3.3	FeII	$3d^5 4s^2 \ b^4G_{11/2} - 3d^6 \ 5D \ 4p \ z^4F_{9/2}^o$
10049.37	3.4	HI	7 – 3
10332.93	1.1	FeII	$3d^6 \ 3F_2 \ 4p \ y^4G_{9/2}^o - 3d^5 4s^2 \ b^4G_{9/2}$
10366.17	1.5	FeII	$3d^6 \ 3F_2 \ 4p \ y^4G_{11/2}^o - 3d^5 4s^2 \ b^4G_{11/2}$
10501.50	2.5	FeII	$3d^5 4s^2 \ b^4G_{9/2} - 3d^6 \ 5D \ 4p \ z^4F_{7/2}^o$

REFERENCES

Anupama, G. C., Sivarani, T., & Pandey, G. 2001, *A&A*, 367, 506

Aretxaga, I., Benetti, S., Terlevich, R. J., Fabian, A. C., Cappellaro, E., Turatto, M., & della Valle, M. 1999, *MNRAS*, 309, 343

Benetti, S., Cappellaro, E., Turatto, M., Taubenberger, S., Harutyunyan, A., & Valenti, S. 2006, *ApJL*, 653, L129

Bowen, D. V., Roth, K. C., Meyer, D. M., & Blades, J. C. 2000, *ApJ*, 536, 225

Brown, P. J., et al. 2007, *ApJ*, 659, 1488

Busche, J. R., Hillier, D. J., 2005, *AJ*, 129, 454

Chandra, P., Ray, A., Schlegel, E. M., Sutaria, F. K., & Pietsch, W. 2005, *ApJ*, 629, 933

Chevalier, R. 1982, *ApJ*, 258, 790

Chevalier, R. A., & Fransson, C. 1994, *ApJ*, 420, 268

Chevalier, R. A., & Fransson, C. 2001, ArXiv Astrophysics e-prints, arXiv:astro-ph/0110060

Chugai, N. N., & Danziger, I. J. 1994, *MNRAS*, 268, 173

Chugai, N. N. 2001, *MNRAS*, 326, 1448

Chugai, N. N., Blinnikov, S. I., Fassia, A., Lundqvist, P., Meikle, W. P. S., & Sorokina, E. I. 2002, *MNRAS*, 330, 473

Chugai, N. N., & Danziger, I. J. 2003, *Astronomy Letters*, 29, 649

Chugai, N. N., et al. 2004a, *MNRAS*, 352, 1213 (C04)

Chugai, N. N., Chevalier, R. A., & Lundqvist, P. 2004b, *MNRAS*, 355, 627

Chugai, N. N., & Yungelson, L. R. 2004, *Astronomy Letters*, 30, 65

Chugai, N. N., & Chevalier, R. A. 2007, *ApJ*, 657, 378

Davidson, K., & Humphreys, R. M. 1997, *ARA&A*, 35, 1

Deng, J., et al. 2004, *ApJL*, 605, L37

Dessart, L., & Hillier, D. J. 2005a, *A&A*, 437, 667

Dessart, L., & Hillier, D. J. 2005b, *A&A*, 439, 671

Dessart, L., & Hillier, D. J. 2006, *A&A*, 447, 691

Dessart, L., & Hillier, D. J. 2008, *MNRAS*, 383, 57

Dessart, L., et al. 2008, *ApJ*, 675, 644, ArXiv e-prints, 711, arXiv:0711.1815

Eldridge, J. J., Mattila, S. & Smartt, S. J. 2007, *MNRAS*, 376, L52

Fabian, A. C., & Terlevich, R. 1996, *MNRAS*, 280, L5

Fassia, A., et al. 2000, *MNRAS*, 318, 1093

Fassia, A., et al. 2001, *MNRAS*, 325, 907

Foley, R. J., Smith, N., Ganeshalingam, M., Li, W., Chornock, R., & Filippenko, A. V. 2007, *ApJL*, 657, L105

Fox, D. W., et al. 2000, *MNRAS*, 319, 1154

Fransson, C., Lundqvist, P., & Chevalier, R. A. 1996, *ApJ*, 461, 993

Fransson, C., et al. 2002, *ApJ*, 572, 350

Fransson, C., et al. 2005, *ApJ*, 622, 991

Gao, Y., Solomon, P. M. 2004, *ApJS*, 153, 62

Gerardy, C. L., Fesen, R. A., Höflich, P., & Wheeler, J. C. 2000, *AJ*, 119, 2968

Hamuy, M., et al. 2003, *Nature*, 424, 651

Han, Z., & Podsiadlowski, P. 2006, *MNRAS*, 368, 1095

Hillier, D. J. 1987, *ApJs*, 63, 965

Hillier, D. J., & Miller, D. L. 1998, *ApJ*, 496, 407

Hoffman, J. L., Leonard, D. C., Chornock, R., Filippenko, A. V., Barth, A. J., & Matheson, T. 2007, ArXiv e-prints, 709, arXiv:0709.3258

Howell, D. A., et al. 2005, *ApJ*, 634, 1190

Kitaura, F. S., Janka, H.-T., Hillebrandt, W. 2006, *A&A*, 450, 345

Kotak, R., Meikle, W. P. S., Adamson, A., & Leggett, S. K. 2004, *MNRAS*, 354, L13

Lentz, E. J., et al. 2001, *ApJ*, 547, 406

Leonard, D. C., Filippenko, A. V., Barth, A. J., & Matheson, T. 2000, *ApJ*, 536, 239

Levesque, E. M., Massey, P., Olsen, K. A. G., Plez, B., Josselin, E., Maeder, A., & Meynet, G. 2005, *ApJ*, 628, 973

Liu, Q.-Z., Hu, J.-Y., Hang, H.-R., Qiu, Y.-L., Zhu, Z.-X., & Qiao, Q.-Y. 2000, *A&AS*, 144, 219

Matheson, T., Filippenko, A. V., Chornock, R., Leonard, D. C., & Li, W. 2000, *AJ*, 119, 2303

Mucciarelli, P., Zampieri, L., Turatto, A. P. M., Cappellaro, E., & Benetti, S. 2006, *Memorie della Societa Astronomica Italiana Supplement*, 9, 391

Ofek, E. O., et al. 2007, *ApJL*, 659, L13

Pastorello, A., et al. 2002, *MNRAS*, 333, 27

Pastorello, A., et al. 2006, *MNRAS*, 370, 1752

Pastorello, A., et al. 2007, *Nature*, 447, 829

Pooley, D., et al. 2002, *ApJ*, 572, 932

Pozzo, M., Meikle, W. P. S., Fassia, A., Geballe, T., Lundqvist, P., Chugai, N. N., & Sollerman, J. 2005, 1604-2004: Supernovae as Cosmological Lighthouses, 342, 337

Pozzo, M., Meikle, W. P. S., Fassia, A., Geballe, T., Lundqvist, P., Chugai, N. N., & Sollerman, J. 2004, *MNRAS*, 352, 457

Rybicki, G. B., & Hummer, D. G. 1994, *A&A*, 290, 553

Salamanca, I., Terlevich, R. J., & Tenorio-Tagle, G. 2002, *MNRAS*, 330, 844

Schlegel, E. M., & Petre, R. 2006, *ApJ*, 646, 378

Schlegel, E. M. 1999, *ApJL*, 527, L85

Smith, N., Gehrz, R. D., Hinz, P. M., Hoffmann, W. F., Hora, J. L., Mamajek, E. E., and Meyer, M. R. 2003, *ApJ*, 125, 1458

Smith, N. 2005, *MNRAS*, 357, 1330

Smith, N., et al. 2007, *ApJ*, 666, 1116

Smith, N., & McCray, R. 2007, *ApJL*, 671, L17

Sobolev, V. V. 1960, Cambridge: Harvard University Press, 1960, “Moving envelopes of stars”.

Sollerman, J., Cumming, R. J., & Lundqvist, P. 1998, *ApJ*, 493, 933 (SCL)

Stathakis, R. A., & Sadler, E. M. 1991, *MNRAS*, 250, 786

Tsvetkov, D. Y. 1995, *Informational Bulletin on Variable Stars*, 4253, 1

Tsvetkov, D. Y., Volnova, A. A., Shulga, A. P., Korotkiy, S. A., Elmhamdi, A., Danziger, I. J., & Ereshko, M. V. 2006, *A&A*, 460, 769

Turatto, M., Cappellaro, E., Danziger, I. J., Benetti, S., Gouffes, C., & della Valle, M. 1993, *MNRAS*, 262, 128

van Dyk, S. D., Weiler, K. W., Sramek, R. A., & Panagia, N. 1993, *ApJL*, 419, L69

Wang, L., Baade, D., Höflich, P., Wheeler, J. C., Kawabata, K., & Nomoto, K. 2004, *ApJL*, 604, L53

Williams, C. L., Panagia, N., Van Dyk, S. D., Lacey, C. K., Weiler, K. W., & Sramek, R. A. 2002, *ApJ*, 581, 396

Wood-Vasey, W. M., Wang, L., & Aldering, G. 2004, *ApJ*, 616, 339

Wood-Vasey, W. M., & Sokoloski, J. L. 2006, *ApJL*, 645, L53

Woosley, S. E., & Janka, T. 2005, *Nature Physics*, 1, 147

Woosley, S. E., Blinnikov, S., & Heger, A. 2007, *Nature*, 450, 390

Zampieri, L., Mucciarelli, P., Pastorello, A., Turatto, M., Cappellaro, E., & Benetti, S. 2005, *MNRAS*, 364, 1419